Università degli Studi di Roma "La Sapienza"

Dipartimento di Ingegneria Meccanica e Aerospaziale
Corso di Dottorato di Ricerca in Ingegneria Spaziale e Astronautica
XXXV Ciclo

Ph.D. Thesis

Heat Transfer Modelling and Analysis of Oxygen/Methane Uncooled and Film-Cooled Liquid Rocket Engines

Submitted in Partial Fulfillment
of the Requirements
for the Degree of
Doctor of Philosophy

Candidate:
Pierluigi Concio

Advisor:
Prof. Francesco Nasuti

Thesis submitted in 2022

A mamma e papà

CONTENTS

LIST OF FIGURES

LIST OF TABLES

NOMENCLATURE

$\dot{m}$	mass flow rate
$\mathcal{M}$	molar mass
$\mathcal{R}$	universal gas constant
$\mathbf{I}$	unit tensor
$\mathbf{v}$	velocity
A	cross section area
B	blowing ratio
c_p	specific heat at constant pressure
e	static energy per unit mass
E_a	activation energy
F	thrust
f	Generic solution variable
G	mass flux
g_0	standard gravity
h	static enthalpy
I_{vac}	vacuum specific impulse
K	equilibrium constant
k	thermal conductivity
L	length, cell width
N_r	number of reactions
N_s	number of species
O/F	Mixture ratio
p	pressure
Pr	Prandtl number
Q	heat
q	heat flux
R	specific gas constant
r	radius, radial coordinate
Re	Reynolds number
s	line of sight
Sc	Schmidt number
St	Stanton number
T	temperature
t	time
u	axial velocity
x	abscissa
y	mass fraction

Subscripts

0	total
2	secondary flow
$conv$	convective
e	exit
f	fuel
g	hot gas, mainstream
i	i–th, of species i
j	j–th, of reaction j
liq	liquid

$_{mix}$	mixing
$_{ox}$	oxidizer
$_{p}$	partecipating species
$_{RE}$	Richardson–extrapolated
$_{st}$	stroichiometric
$_{T}$	turbulent
$_{vac}$	vacuum
$_{w}$	wall

Greek

α	third–body efficiency
χ	molar fraction
$\dot{\omega}_i$	species production term
ϵ	emittance
η_{c^*}	combustion efficiency
Γ	Liquid mass flow rate per unit circumference
μ	dynamic viscosity
ϕ	equivalence ratio
ρ	density
ε	numerical error
ξ	Equivalent distributed friction

Superscripts

P	Products
R	Reactants

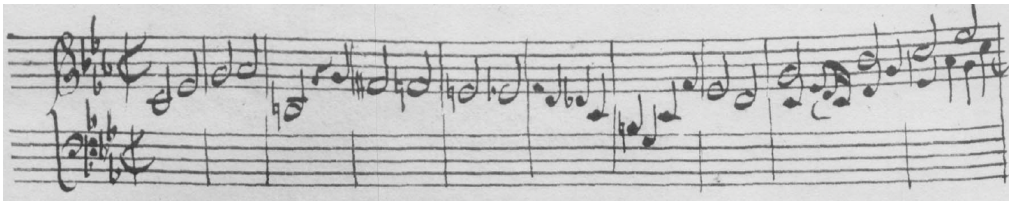

Das Musikalische Opfer (BWV 1079) - Thema Regium
J.S. Bach, 1747

ACKNOWLEDGEMENTS

First of all, with deepest esteem and admiration, I would like to thank my advisor Prof. Francesco Nasuti, who guided me through this Ph.D. with a lot of confidence, humanity, and support.

I would like to thank Prof. Daniele Bianchi too, for his wise advice and all the precious time he dedicated to me.

My most heartfelt gratitude goes to Simone and Mario. Thanks Simone for having been by my side during the hardest moments of this Ph.D. always giving me a reason to go on, and for having taught me that sometimes it is better to go straight to the point without wasting time.
Thanks Mario for having taught me to be fussy and to always look for an explanation. Our long walks and conversations made my day more than once.

Thanks to mamma e papà, to whom this thesis is dedicated, for always supporting me unconditionally with love and dedication. The achievement of such a milestone would not have been possible without you.

Thanks to Lorenzo for being by rock. No matter what happens, i know you will be there for me. You are the most important person in my life.

Thanks to my colleagues and dear friends Beatrice, Matteo, and Paolo, who always said hello to me in the morning with a big smile. Going to work has been a pleasure because of you.

Thanks to my friends Filippo, Lorenzo, Luca, Marco, Riccardo, and Simone for being a constant encouragement and for all the moments spent together.
I planned my future with each of you by my side.

Last but not least, thank you Arianna for the incredible idea to show the qr-code alongside with the manuscript of the Musical Offering by Johann Sebastian Bach. This might be the occasion for the reader to get to know/enjoy such a wonder of music history.

Rome, 2022 P. C.

ABSTRACT

The high hot gas temperatures and chamber pressures typical of modern liquid rocket engines (LREs) yield high local wall heat fluxes which have to be inevitably managed by the engine active cooling system. Nowadays, regenerative cooling alone might not be enough to counteract such high thermal loads in high-pressure high–performance engines, so cooling capabilities are typically enhanced with the addition of further strategies, such as film cooling or mixture ratio biased peripheral injectors. The prediction of wall heat flux in LREs is of paramount importance during the design phase both for sizing and safety purposes, especially at the nozzle throat where the maximum thermal load occurs. Numerical simulations can help in the prediction, provided that they can be effectively used during the design phase and that suitable modeling is employed.

In this framework, this thesis aims at evaluating the suitability of different modeling solutions to predict in affordable times the wall heat flux of LREs employing the oxygen-methane propellant combination, which is nowadays attracting the attention of many developers as a possible cheaper and denser replacement to hydrogen. In particular, the first part of the results presented in this thesis is devoted to the analysis of the throat heat flux, whereas the second part addresses the cylindrical region of the combustion chamber.

Computational fluid dynamics (CFD) simplified approaches are presented initially in case of absence of an active cooling system, and validated against experimental data as well as more accurate yet simplified numerical simulations carried out with a higher level of model completeness.

Then, the cooling strategy is introduced focusing on gaseous film cooling and mixture ratio bias techniques. Due to the extreme lack of experimental data in the literature regarding the oxygen–methane propellant combination, attention is focused on a second thrust chamber representative of a possible methane–fueled upper stage. The simplified approaches validated for the uncooled case are employed and further improved to perform parametric analyses aimed at investigating how the main design parameters, such as the secondary flow mass flow rate and mixture ratio, affect the throat heat flux and the engine performances.

Eventually, the second and final part of the results addresses the low–order modeling of gaseous and liquid film cooling in the cylindrical part of the combustion chamber. An extensive literature review allowed to select the most appropriate formulations to be implemented in the EcosimPro/ESPSS (European Space Propulsion System Simulation) framework, eventually providing a new component to be included in the multi–physics platform. The reliability of the predictions is assessed by analyzing transients and comparing the steady–

state results against the selected experimental test cases and CFD numerical simulations performed employing the approaches above.

1 INTRODUCTION

Liquid rocket engine (LRE) operations are characterized by wall heat fluxes, originated from combustion and chemical reactions, that can reach the order of magnitude of 100 MW/m^2. Because of this high amount of heat, a design trade-off between overall engine efficiency and safe structural life is required, and active cooling systems are needed to suitably extract heat from the hot-gas flow and maintain the wall material temperature within the admissible range. Therefore, heat transfer analysis is of paramount importance for the design, testing, and analysis of LREs.

In this framework, numerical simulations play a key role because of their versatility and ability to save resources with respect to more expensive and time–consuming procedures such as hot–firing tests. Since the development of boundary–layer–based empirical relations, such as the famous and mostly used Bartz equation [1], significant progresses have been made thanks to computational fluid dynamics (CFD) developments. However, a detailed simulation of a LRE thrust chamber should include modelling of: turbulent mixing and combustion possibly with two–phase flow or supercritical fluids; finite–rate reactions along the whole thrust chamber; boundary layers; low–subsonic to high–supersonic velocities; and radiative heat flux. Even if in principle one can consider to include all of this modelling in a single simulation, it will certainly require heavy computations with considerable computational times. Admitting that such a detailed computation can be made, it could be certainly more likely useful as a numerical test bench to validate reduced–order models rather than as a practical design tool able to perform several design iterations and parametric analyses. Moreover, in any case, numerical models need to be validated against experimental data over a wide range of operating conditions to prove their capability of describing the main phenomena occurring in the whole thrust chamber. However, thanks to the different numerical simulation models which have been developed so far, a selection of the most suited approach depending on the purpose of the study can be made.

This introductory chapter begins presenting the most recent developments concerning the nozzle throat heat transfer analysis and simulation in oxygen–methane LREs. It continues illustrating the state of the art of both liquid and gaseous film cooling modelling, focusing on low-order numerical formulations, and the main features of the mixture ratio bias technique. The main objectives of the work conducted during this Ph.D. research are then presented, and a brief outline of the thesis concludes the introductory overview.

1.1 NOZZLE THROAT HEAT TRANSFER IN OXYGEN–METHANE LRE

The study and prediction of the heat directed from combustion gases towards the wall must surely take into account the combustion process evolution along the thrust chamber. As it is well known, combustion evolves in different zones of the thrust chamber identified as: 1) the injection/atomization zone, 2) the rapid combustion zone, 3) the streamtube combustion zone, 4) the transonic flow zone, and 5) the supersonic flow zone [2] (Fig. 1).

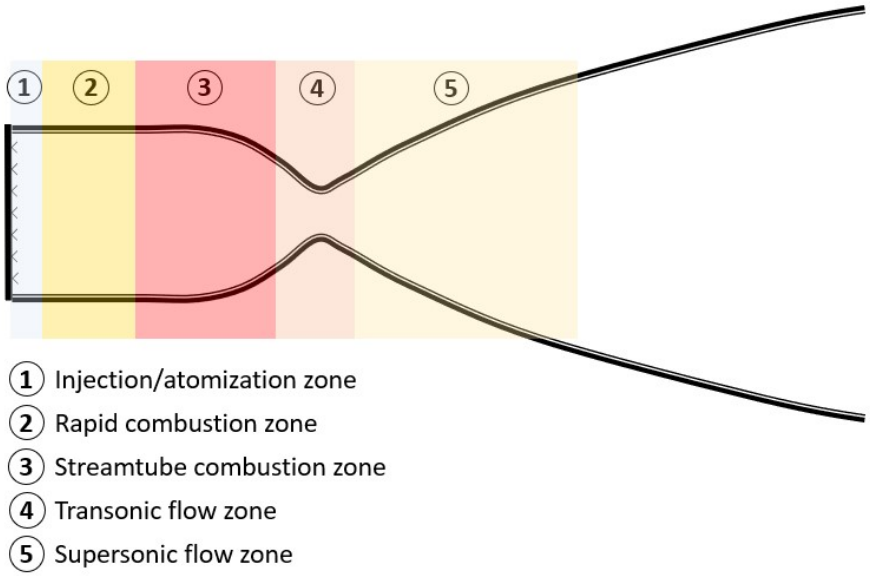

Figure 1: Zones for the analysis of a thrust chamber according to [2].

Different studies and modeling are requested to include the main phenomena driving the flow evolution and wall heat exchange in these different zones. The first two zones (see 1–2 in Fig. 1) are directly governed by the three–dimensional flow evolution near the injection plate, whereas in the streamtube zone (3) the flow evolves more and more towards a roughly one–dimensional core flow, depending on the size of the engine and on the length of the combustion chamber. Eventually, the transonic and supersonic flow regions show roughly two–dimensional flows mainly governed by the gas dynamic expansion.

Focusing on the validation of simulations aimed to predict thrust chamber heat flux, several experimental studies have reported the measured wall temperature and heat flux in the combustion chamber up to the convergent section of the nozzle (e.g. [3–6]). However, data on heat transfer in the nozzle throat region are barely available in the literature due to the difficulty to obtain a safe and reliable measurement. Data available in the open literature have been collected and compared by Pizzarelli [7]. The availability of experimental data for estimation of wall temperature and code validation is even lower when new

concepts based on less spread propellant combinations are considered. Among others, this is the case for the oxygen/methane propellant combination, which is catching much attention in recent years [8–12]. Methane is considered a valid low-cost replacement for other hydrocarbons like kerosene because of its higher specific impulse, cooling efficiency, and low level of coking and sooting, this last aspect being relevant especially for reusable launch vehicle applications. Methane can also compete with liquid hydrogen because its higher density allows for more compact tanks, turbomachinery, and stage size.

Among the data reported in Ref. [7] only a few address the oxygen/methane propellant combination [13, 14] which, however, are not suitable for CFD validation because of the lack of data. On the other hand, more recent analyses, using both heat sink and actively cooled subscale hardware with different geometries, injection patterns, and operating conditions, have been carried out with the purpose of providing data for validation of numerical approaches [5, 15, 16]. Although these experiments were mostly focused on the combustion chamber, Refs. [15, 16] also provide useful data for throat heat flux analyses. In fact, the actively cooled apparatus permitted measuring the heat flux in the throat region by exploiting the measurements of temperature variation between cooling system manifolds, as also reported in Ref. [17]. The collected data have been used by different research groups for the validation of computations made by commercial and in-house CFD software for the single-element [18–23] and the multi-element test cases [17, 21, 24–28]. Overall, those simulations with detailed CFD modeling (three-dimensional flow, detailed injection, high wall resolution) yield some differences both among each other and with the experimental data [25] despite the heavy computational burden, thus not allowing one to identify an approach that is more appropriate than the others.

1.2 FILM COOLING MODELING: STATE OF THE ART

The high temperature differences between the hot gases and the chamber walls together with chamber pressures of more than 180 bar result in extremely high heat flux levels and temperature gradients through the combustion chamber. Regenerative cooling system performaces alone are not enough in high–performance rocket engines to withstand such high thermal loads. Improvements could be either done by increasing the coolant velocity in the cooling channels or by a further reduction of the wall thickness between the coolant and hot gas. However, a higher coolant velocity would increase the pressure drop, resulting in additional loads for the propellant feed system. On the other hand, a reduced wall thickness would increase manufacturing risks, since current wall thicknesses (for instance in the Vulcain 2) are already far below 1 mm, also reducing safety and reliability of the combustion chamber. Therefore, in order to keep up with our challenging times in which higher and higher performances and thus chamber pressures and heat flux levels are required, re-

generative cooling capabilities must be augmented with an additional cooling system to guarantee safe operations and a long structural life of the engine. Film cooling, in particular, is an active cooling method used to protect combustion chamber and nozzle walls against high thermal loads. A controlled flow of coolant is introduced either in liquid or gaseous phase as a thin film through circular slots or discrete holes placed in the combustion chamber, for example at the outer row of the injection plate or at different positions downstream, or at a specific nozzle plane toward the throat. A meticulous design is required to limit the performance losses yielded by the injection of such a cold fluid. For this purpose, the typical coolant mass flow rate employed in film cooling applications is in the range between 1 and 6% of the total mass flow rate.

In this section the main results concerning liquid and gaseous film cooling modelling available in open literature are presented. Particular attention is paid to numerical and modelling aspects in liquid rocket engines combustion chambers and nozzles.

1.2.1 Liquid film cooling

Liquid film cooling (LFC) is being studied since the early '50s, trying to understand the effect of different injection configurations and coolants on the film cooling performances in the first place, and then to assess its applicability to rocket applications [29–37]. The latter was guaranteed by early feasibility studies [29–31, 36, 38, 39], in which significant wall heat flux reduction was observed with acceptable performance losses in terms of specific impulse employing both storable and cryogenic propellants. Those kinds of propellants, such as hydrazine–type propellants, hydrogen, and methane, were considered more suited for film cooling of rocket engines than other coolants used in the past years [31], due to high heat of vaporization and high heat capacity in gaseous phase, respectively.

Only few experimental studies on LFC under rocket engine–like conditions are available. Nevertheless, different propellants such as space storable [40], hydrocarbons [38, 41, 42] and hydrogen [36] have been employed, even at high pressures up to 138 bar, to test the heat flux reduction due to LFC. Three peculiar and particularly challenging aspects can be defined for LFC, i.e the liquid film stability, its phase change (evaporation), and the so–called film cooled length (FCL). In particular, the FCL is defined as the length after which the film ceases to exist in liquid phase, thus changing completely the cooling performances. The determination of the evaporation rate for both inert and reactive coolants was the object of the early analytical and empirical studies on LFC [43, 44]. A lot of hypotheses, such as a stable liquid film, were retained to obtain results in closed form. Eventually, models were also calibrated on the basis of very specific experimental data, yielding very limited applicability in some cases [35, 45, 46]. Unrealistic treatments of film stability also led to high discrepancies in later numerical studies [47]. Different attempts have been

made to develop numerical correlations accounting also for the entrainment of liquid droplets in the gaseous phase. Gater et al. [48] correlated the mass and energy transfer due to vaporization and unvaporized liquid entrainment with the Stanton number and the coolant flow rate, strictly relying on experimental data on liquid–gas interfacial structure and interaction. Unfortunately, experimental data have never been available to prove their technique. Stechman et al. [31] calculated the turbulent heat transfer coefficient between the liquid film and the wall analytically by means of a modified Bartz equation, obtaining 20% error. Corrections to the equation were introduced to include film instability, the two-phase nature of the flow and the variation of transport properties between the main core gas and the coolant. Nevertheless, the model was found to provide good results only in case of small engines. A correlation yielding good, yet limited, results has been recently developed by Sawant et al. [49], who correlated the liquid entrained fraction with the Weber and coolant Reynolds numbers. However, the correlation was developed relying only on air–water test data, hence there is still a need for improvement considering fluids with different properties. Experiments were conducted within a limited pressure range, up to 6 bar, and for several coolant flow rates. Even nowadays, the liquid entrainment and film stability phenomena are not understood enough to draw definitive conclusions [50, 51], and no experimental information is available for assessment under rocket engine-like conditions. Nevertheless, Shine et al. [52] were able to observe the liquid surface shearing due to disturbance waves by means of transient numerical simulations, and to identify that as the main mechanism of liquid entrainment.

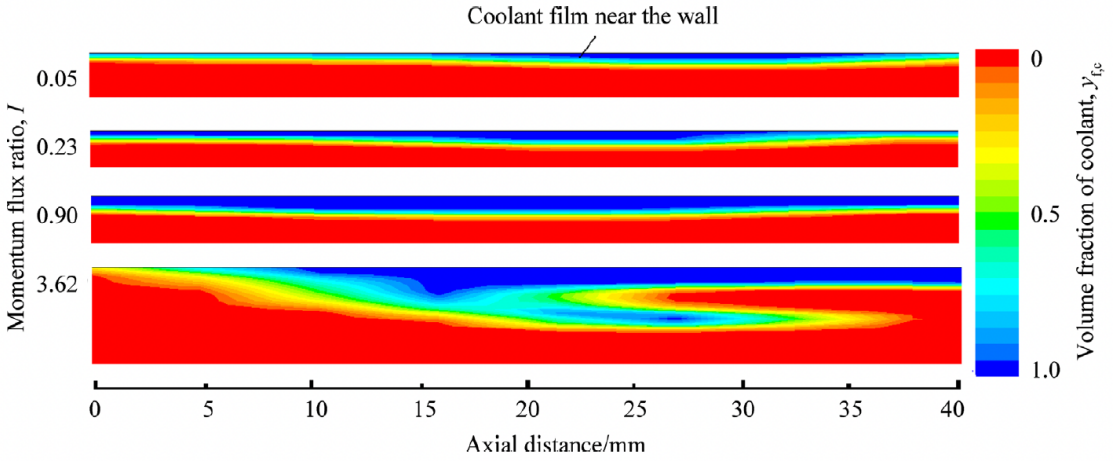

Figure 2: Liquid–gas interface shapes at different momentum flux ratios [52].

As shown in Fig. 2 liquid pockets start being entrained in the gaseous mainstream at high momentum flux ratio, i.e. when the liquid–gas interface becomes unstable. Liquid entrainment was also included in semi–analytical models developed for the determination of the FCL. Ewen and Evensen [53] proposed a compact expression, in which the FCL is calculated as a function of the coolant flow rate and a liquid entrainment parameter. The latter is

based largely on empirical correlations, and depends on both phases and interface properties, such as density, velocity, temperature, and surface tension. This model, together with that by Stechman et al. [31], has been applied to an oxygen–kerosene combustion chamber by Trotti [54], showing a discrete general matching but with an overall overestimation. Grisson [55] developed a 1–D model for the determination of the evaporation rate and the FCL, also including the effect of radiation in a rocket thrust chamber. Liquid entrainment and flow acceleration effects were neglected, making this model valid only at low coolant flow rates. The model employs a LFC treatment until the film dry–out point, after which the coolant is considered as a gas. After the nozzle entrance, a correction term accounts for the increased mixing due to the geometry. Further downstream results can not be compared with any benchmark due to the lack of modelling concerning the neglected flow acceleration effects. This model has been recently adapted by Jang et al. [56] to calculate the FCL in a H_2O_2/RP–1 bipropellant thruster. The model was kept essentially unchanged, but, in addition, thermal decomposition of H_2O_2 was considered by means of an empirical constant, and it was observed how this process caused a reduction of the FCL. Further modelling has been provided by Shine et al. [57], who developed a semi–analytical model including both radiation and liquid entrainment for the calculation of the FCL in chambers operating at subcritical pressures. Numerical correlations by Sawant et al. [49] and Leckner [58], respectively for liquid entrainment and gas total emittance calculation, were employed. Among all, results have been compared also against the same experimental data used by Grisson [29], showing good agreement.

Very few CFD numerical studies based on RANS computations are available [59–62]. Nevertheless, they permitted to study the behavior of LFC when integrated in regeneratively cooled engines. To the author's knowledge, no research activity is available on liquid film cooling under supercritical conditions in rocket thrust chambers.

1.2.2 Gaseous film cooling

Similarly to LFC, the study of gaseous film cooling (GFC) started in the '50s with investigations dedicated to understand the effects of different coolant injection procedures on the main stream boundary layer [63–68], until the first feasibility studies performed in rocket combustion chambers and nozzles [69, 70]. Hydrogen, methane, and also nitrogen and propane were used as coolants, realizing that the former two are more suitable for rocket applications. Moreover, multi–slot coolant injection was found to be more suited for high–energy propellants in rocket applications as well. In this framework, turbulence and compressibility effects on film cooling performances have been largely discussed in the literature. A significant decrease in the film cooling performances was found to occur with an increase of the free stream turbulence level first by Carlson and Talmor [71] in the late '60s and then by Gau et al. [72] in the '90s,

whereas no significant consequences occur by changing the turbulence intensity of the coolant jet [73]. On the other hand, compressibility effects were considered negligible as a first approximation in combustion chambers for a wide range of velocities and temperatures until the early '70s [74, 75]. Opposite results have been found experimentally by Pedersen et al. [76] and Hansmann et al. [77] within the following 20 years, according to which density and velocity ratios have a considerable influence on the film cooling effectiveness. Eventually, Dellimore et al. [78] confirmed this statement showing that flow compressibility changes the growth rate of the shear layer between the main and secondary flows. They also attributed the contradictory results obtained in the past to the use of a low Mach number.

Few yet significant experimental studies under different rocket engine-like conditions have been recently developed [42, 79–82], also providing a great amount of data for validation of numerical tools. Hydrogen, methane and kerosene were employed as coolants under low, medium, and high-pressure conditions for different chamber and injection slot geometries. The assessment of the role played by blowing ratio, i.e., the ratio between coolant and mainstream mass fluxes, coolant mass flow rate, slot dimensions, and out–of–plane motions on film cooling performances was the main goal of these campaigns. Experimental information is available also in the framework of supersonic GFC. One of the first goals was that of Goldstein [83] in the '60s to study the effect of the blowing ratio on the adiabatic wall temperature using a single slot for coolant injection. Important developments were made in the '90s, when Juhany et al. [84] showed that cooling effectiveness improves with increasing injectant Mach number and heat capacity. A large amount of data was produced in the following years by Aupoix et al. [85], considering different geometries, pressure ratios and film temperatures. They observed the improvement on film cooling efficiency in supersonic conditions due to reduced mixing, thus confirming Juhany et al. results. Further studies were performed recently on the effect of the coolant jet on flow separation in TOC (thrust optimized contour) nozzles [86] and the decrease of film cooling effectiveness in presence of an impinging shock waves [87].

Concerning the modelling, the determination of GFC performances has been mostly carried out empirically. Several numerical correlations have been proposed [88–92], typically in terms of adiabatic film cooling effectiveness, which represents the capability of the coolant jet to thermally insulate a surface. A great number of studies and results is available in the literature concerning GFC, but, unfortunately, only few recent numerical analyses address rocket thrust chambers. Early studies were dedicated to the study the applicability of GFC and to correlate the adiabatic film cooling effectiveness with the injection procedure. As described in detail by Goldstein [68], investigations expressed empirically the cooling effectiveness as a function of the blowing ratio, fluid properties, distance from the injector and the Reynolds number, using very similar mathematical expressions. These models [89–92] assume constant

properties ideal gases, a constant average temperature in the boundary layer, and a full mixing of the coolant with the mainstream. Good agreement was found against experimental data though, due to a sort of counter–balancing effect introduced by the last two assumptions. A significant improvement was made by Goldstein and Haji-Sheikh [93], who tried to correct the assumptions relying on available experimental data made in the past. New dependencies were proposed, such as the coolant molar mass, Prandtl number, and the angle of injection. Comparisons with experimental data proved that such modelling was able to provide better results than the previous techniques. Other empirical models were developed, always providing worse results than Goldstein and Haji-Sheikh. Hatch and Papell [94], for instance, developed an experimentally assessed correlation relying again on the assumption of fully mixed flow, even in case of angled injection. Several years later, the model was considered valid also in case of multiple injection of coolant by Sellers [95], but some aspects remained fairly questionable. Spalding [96] proposed instead a piecewise–defined correlation to describe the film cooling effectiveness drop downstream of the film breaking point, but the model was limited only to injection parallel to the wall.
On the other hand, recently, Arnold et al. [97] claimed that none of the previous models considered the extreme conditions inside a rocket thrust chamber and the acceleration due to a high-pressure gradient in presence of a fully turbulent, high–temperature flow with variable properties. A modified empirical correlation was hence developed on the basis of that by Goldstein and Haji-Sheikh [93]. Flow acceleration effects were included by adapting the approach initially proposed by Hartnett et al. [89] to the chamber environment. Assessments have been done with experimental data by the authors themselves, showing good agreement under typical conditions of liquid rocket engines. Further developments have been proposed starting from that by Simon [98]. Assuming incompressible flow, the latter expresses the film cooling effectiveness as a function of coolant mass flow rate, core flow turbulence level, and coolant and main stream temperatures. Experimental data [99] were considered for the empirical model closure. The wall–jet and the fully developed regions were distinguished by interposing a fully mixed zone in between. Important conclusions were drawn by Dellimore et al. [78] by improving Simon's model including the effects of adverse and favorable pressure gradients and flow compressibility as briefly described above. In particular, the velocity ratio was found to control the film cooling performance in presence of a pressure gradient. Simon's equations and geometry were retained by Di Matteo et al. [100], who developed a new model by adding the effect of variable heat capacity with temperature, the presence of two different fluids, and high temperature ratios. Results have been validated against oxygen–hydrogen experimental data [81], showing good agreement.

As for LFC, few numerical CFD studies are available in literature. RANS–based approaches were preferred to study the film cooling performances both in combustion chambers [101–104] and nozzles [105–108]. No information is

available concerning LES or DNS approaches applied to GFC under rocket engine-like conditions.

1.3 MIXTURE RATIO BIAS

The role of film injection in the frame of chamber cooling is to lower the temperature of the gases which come in contact with the chamber wall. A similar strategy which allows to pursue the same objective is the modification of the peripheral injector mixture ratio, regardless of the other employed cooling techniques. Such a procedure, called *mixture ratio bias* or *shift*, is of the same nature of film cooling, involving the injection of a secondary flow in the combustion chamber, mixing and reacting with the hot gas. In this regard, the mixture ratio bias of the outer region of the injector plate is usually achieved by making this region more fuel–rich than the core flow, producing lower–temperature combustion products, and, therefore, reducing substantially the wall heat flux. To the author's knowledge, no dedicated CFD or other kinds of studies are available in the literature concerning mixture ratio bias in oxygen/methane LRE thrust chambers.

1.4 OBJECTIVES AND OUTLINE

The main goal of this research is to perform heat transfer analyses in oxygen/methane thrust chambers employing different design solutions, namely the absence of an active cooling system, film cooling, and mixture ratio biased peripheral injectors, in sight of a future high–performance LRE application. The suitability of several CFD and low–order simplified numerical approaches is evaluated on the basis of heat flux predictions and comparison with the few experimental data available in the literature. Two simplified CFD numerical approaches with increasing level of model complexity are employed to understand the impact that a detailed injection and combustion modelling produces on the throat heat flux, i.e. the role of modelling the details of zones 1 and 2 on the prediction of the heat flux in zone 4 according to Fig. 1. In this regard, the interest to study the throat heat flux estimation for oxygen/methane engines comes from the known greater role played by the near–wall recombination reactions, as compared to the oxygen/hydrogen propellant pair.

Once the best trade–off between accuracy and computational effort has been found, the CFD approach is enriched by adding a near–wall secondary flow injection, with both film cooling and mixture ratio bias techniques, while preserving its modelling simplicity and versatility. Pros and cons yielded by the two wall cooling approaches on throat heat flux and engine performance are analyzed by considering a well–designed engine configuration with operating conditions in terms of total mass flow rate and global mixture ratio typical of a

LRE application. The main design parameters are identified on the basis of the literature, and parametric analyses are performed to observe the role of each parameter on the throat wall heat flux reduction and performance loss within a comprehensive range of investigation.

The last part of the thesis aims at presenting low–order models for liquid and gaseous film cooling in oxygen/methane LRE combustion chambers. In this regard, a brand–new liquid and gaseous film–cooled thrust chamber component is designed to be included in the EcosimPro/ESPSS simulation platform, hence enriching and improving its heat loads prediction capabilities. Such a new component might represent a useful tool during the engine development phase, for two main reasons. The first is the quick evaluation of a complex phenomenon, even if performed in an approximate way, allowing for parametric analyses with a low computational effort. The second is the inclusion of wall film cooling in a system–wide representation in which interdependence with other phenomena might occur. Low–order models are assessed by analyzing transients and comparing the steady–state results with the selected experimental test cases and purposely carried out CFD simulations.

Part I of this thesis is devoted to the presentation of the numerical models. In particular, the numerical model used to carry out CFD numerical simulations is presented in Chap. 2, whereas an in–depth description of the reduced models implemented in the EcosimPro/ESPSS platform as a new LRE film–cooled thrust chamber component is provided in Chap. 3.
Numerical results are presented in Part II. Results of the heat transfer CFD analyses performed on uncooled, film cooled, and mixture ratio biased thrust chambers are illustrated in Chapters. 4 and 5. Eventually, the validation of the reduced liquid and gaseous film cooling models by means of the EcosimPro/ESPSS platform is provided in Chap. 6. Conclusions are summarized in Chap. 7.

Part I

MODELLING

2 CFD MODEL

The numerical model used to perform CFD heat transfer analyses employing the different approaches presented later in Part II is described in this chapter.

The numerical study of the wall heat transfer in the cylindrical part and at nozzle throat of LRE thrust chambers requires suitable modelling of convective and radiative phenomena. In this framework, the convective contribution to the total heat flux is modeled through a suitable CFD approach (Section 2.1), making use of an in–house three–dimensional finite–volume Reynolds–Averaged Navier–Stokes (RANS) solver. The solver is second–order accurate in space and time, and capable to handle multicomponent mixtures of turbulent, reactive, compressible, and thermally perfect gases. On the other hand, the radiative contribution is modeled separately by solving the radiative transfer equation (RTE) on the basis of the local conditions of the flowfield as computed by the CFD model. Thermal radiation model features are described in Section 2.2.

2.1 FLOWFIELD AND CONVECTION MODELLING

The convective contribution to the wall heat flux is computed by solving the compressible Reynolds–averaged Navier–Stokes (RANS) equations for reacting mixtures [109]:

$$\begin{aligned}
&\frac{\partial(\rho y_i)}{\partial t} + \nabla\cdot(\rho \mathbf{v} y_i) = -\nabla\cdot\mathbf{j}_i + \dot{\omega}_i \qquad (i = 1, ..., N_s)\\
&\frac{\partial(\rho \mathbf{v})}{\partial t} + \nabla\cdot(\rho \mathbf{v}\mathbf{v}) = \nabla\cdot\mathbf{S}\\
&\frac{\partial(\rho e_0)}{\partial t} + \nabla\cdot(\rho e_0 \mathbf{v}) = \nabla\cdot(\mathbf{v}\cdot\mathbf{S}) - \nabla\cdot\mathbf{q}
\end{aligned} \tag{1}$$

where the mixture total energy per unit mass e_0 is defined as

$$e_0 = \sum_{i=1}^{N_s} y_i e_i + \frac{\mathbf{v}\cdot\mathbf{v}}{2} \tag{2}$$

The quantities under divergence sign on the right hand side of Eq. (1) are:

$$\begin{aligned} \mathbf{j}_i &= -\left(\frac{\mu}{Sc}+\frac{\mu_T}{Sc_T}\right)\nabla y_i \\ \mathbf{S} &= -p\mathbf{I}-(\mu+\mu_T)\left\{\frac{2}{3}(\nabla\cdot\mathbf{v})\mathbf{I}+\left[\nabla\mathbf{v}+(\nabla\mathbf{v})^T\right]\right\} \\ \mathbf{q} &= -\left(k+\frac{\mu_T}{Pr_T}\sum_{i=1}^{N_s} y_i c_{p,i}\right)\nabla T+\sum_{i=1}^{N_s}\left(h_i+\Delta h^\circ_{f,i}\right)\mathbf{j}_i \end{aligned} \tag{3}$$

which represent the mass diffusion flux vector of the i-th species, the stress tensor, and the heat flux vector, respectively. Notice that the mass fluxes $\mathbf{j}_i$ are corrected to ensure that they sum to zero by distributing the residual according to the species mass fraction [110]. According to Ref. [110], this correction allows to obtain results close to formulations based on gradients of molar mass fractions (Hirschfelder approximation [111]). Thermodynamic closure is obtained assuming a thermally perfect gas mixture, governed by the equation of state

$$p=\rho RT \quad \text{with} \quad R=\sum_{i=1}^{N_s} y_i R_i \tag{4}$$

where R_i is the species gas constant. The caloric equation of state is obtained expressing constant pressure specific heats as a function of temperature according to the seventh-order polynomial written for each species:

$$\begin{aligned} c_{p,i}(T) =& a_{1,i}T^{-2}+a_{2,i}T^{-1}+a_{3,i}+a_{4,i}T+ \\ &+a_{5,i}T^2+a_{6,i}T^3+a_{7,i}T^4 \qquad\qquad (i=1,\ldots,N_s) \end{aligned} \tag{5}$$

with coefficients $a_{1,i}, a_{2_i}, \ldots, a_{7,i}$ reported in Ref.[112]. The standard heat of formation for the i-th species $\Delta h^\circ_{f,i}$ is also taken from Ref. [112]. The molecular transport properties μ and k are derived from those of the individual species according to Wilke's rule [109], and those of individual species are taken from the fourth–order polynomials of temperature reported in Ref. [113]. Species diffusion is considered to be the same for all the N_s species through a constant Schmidt number, assumed as $Sc = 0.7$. Turbulent viscosity μ_T is evaluated by the integration of an additional convection/diffusion equation, according to the Spalart-Allmaras one–equation model [114], whose standard constants are used for model closure. Turbulent diffusivity and conductivity are evaluated on the basis of μ_T through constant turbulent Schmidt and Prandtl numbers, $Sc_T = 0.7$ and $Pr_T = 0.9$, respectively.

The chemical source terms $\dot{\omega}_i$ in Eq. (1) are obtained by the contribution of each of the N_r reactions as

$$\dot{\omega}_i = \mathcal{M}_i\sum_{j=1}^{N_r}(\nu^P_{i,j}-\nu^R_{i,j})\left[k_{f,j}\prod_{s=1}^{N_s}\left(\frac{\rho_s}{\mathcal{M}_s}\right)^{\nu^R_{s,j}}-k_{b,j}\prod_{s=1}^{N_s}\left(\frac{\rho_s}{\mathcal{M}_s}\right)^{\nu^P_{s,j}}\right]\alpha_j \tag{6}$$

where the generic reaction among species B_i is expressed with stoichiometric coefficients of reactants $\nu_{i_j}^R$ and products $\nu_{i_j}^P$ as:

$$\sum_{i=1}^{N_s} \nu_{i,j}^R B_i \rightleftarrows \sum_{i=1}^{N_s} \nu_{i,j}^P B_i \qquad (j = 1, ..., N_r) \tag{7}$$

and forward $k_{f,j}$ and backward $k_{b,j}$ reaction rates are expressed as

$$k_{f,j} = A_j \, T^{n_j} \exp\left(-\frac{E_{a,j}}{\mathcal{R}T}\right) \qquad k_{b,j} = k_{f,j}/K_j \tag{8}$$

where A_j is the pre-exponential factor, n_j the temperature exponent, $E_{a,j}$ the molar activation energy, $\mathcal{R}$ the universal gas constant, and K_j the equilibrium constant of the j-th reaction evaluated from thermodynamic data taken from Ref. [112]. The coefficient α_j in Eq. (6) is generally equal to one, except for the case of reactions involving a generic third body M; in such a case, it is defined as

$$\alpha_j = \sum_{i=1}^{N_s} \hat{\alpha}_{i,j} \left(\frac{\rho_i}{\mathcal{M}_i}\right) \tag{9}$$

where $\hat{\alpha}_{i,j}$ is the third–body efficiency of the i–th species when involved in the j-th reaction.

Two reaction mechanisms are used in this thesis to evaluate differences among numerical results. Most of the CFD numerical simulations employ an extension of the Jones-Lindstedt [115] global reaction mechanism for an oxygen/methane mixture (Table 1). This mechanism includes three additional species and three extra reactions with respect to the original one with the goal of taking into account recombination reactions of dissociated species. Hereafter such 9–species 7–reactions mechanism will be referred to as "JL–R" (Jones Lindsted with recombinations). It has been introduced and validated in the range 10-100 bar for recombination reactions in Ref. [116] and allows to get the correct equilibrium composition at the end of the combustion process.

Table 1: JL–R global reaction mechanism for oxygen–methane simulations [116] (A_j units are expressed in kmoles, meters, and seconds)

j	Reaction	A_j	n_j	$E_{a,j}/\mathcal{R}$ (K)
1	$\frac{1}{2}CH_4 + \frac{5}{4}O_2 \longrightarrow CO + 2H_2 + \frac{3}{4}O_2 - \frac{1}{2}CH_4$	$4.40 \cdot 10^{11}$	0.00	15096.6
2	$CH_4 + H_2O \longrightarrow CO + 3H_2$	$3.00 \cdot 10^{08}$	0.00	15096.6
3	$CO + H_2O \rightleftarrows CO_2 + H_2$	$2.75 \cdot 10^{09}$	0.00	10064.4
4	$\frac{1}{4}H_2 + \frac{3}{2}O_2 \rightleftarrows 2H_2O + \frac{1}{2}O_2 - \frac{7}{4}H_2$	$6.80 \cdot 10^{15}$	-1.00	20128.8
5	$O_2 \rightleftarrows 2O$	$1.50 \cdot 10^{09}$	0.00	56863.8
6	$H_2O \rightleftarrows H + OH$	$2.30 \cdot 10^{22}$	-3.00	60386.3
7	$OH + H_2 \rightleftarrows H + H_2O$	$2.10 \cdot 10^{05}$	1.51	1726.0

As a term of comparison for the JL–R chemical kinetics, a second reaction mechanism is adopted [117] (see Table 2).

Table 2: TSR-CDF-13 skeletal reaction mechanism for oxygen–methane simulations [117] (A_j units are expressed in kmoles, meters, and seconds)

j	Reaction	A_j	n_j	$E_{a,j}/\mathcal{R}$ (K)
1	$2\,O + M \rightleftarrows O_2 + M$	$1.20 \cdot 10^{14}$	-1.00	0.0
2	$H + O + M \rightleftarrows OH + M$	$5.00 \cdot 10^{14}$	-1.00	0.0
3	$H_2 + O \rightleftarrows H + OH$	$5.00 \cdot 10^{01}$	2.67	3165.2
4	$HO_2 + O \rightleftarrows O_2 + OH$	$2.00 \cdot 10^{10}$	0.00	0.0
5	$CH_3 + O \rightleftarrows CH_2O + H$	$8.43 \cdot 10^{10}$	0.00	0.0
6	$CH_4 + O \rightleftarrows CH_3 + OH$	$1.02 \cdot 10^{06}$	1.50	4327.7
7	$CO + O + M \rightleftarrows CO_2 + M$	$6.02 \cdot 10^{11}$	0.00	1509.7
8	$HCO + O \rightleftarrows CO + OH$	$3.00 \cdot 10^{10}$	0.00	0.0
9	$HCO + O \rightleftarrows CO_2 + H$	$3.00 \cdot 10^{10}$	0.00	0.0
10	$CH_2O + O \rightleftarrows HCO + OH$	$3.90 \cdot 10^{10}$	0.00	1781.4
11	$CO + O_2 \rightleftarrows CO_2 + O$	$2.50 \cdot 10^{09}$	0.00	24053.9
12	$CH_2O + O_2 \rightleftarrows HCO + HO_2$	$1.00 \cdot 10^{11}$	0.00	20128.8
13	$H + O_2 + M \rightleftarrows HO_2 + M$	$2.80 \cdot 10^{15}$	-0.86	0.0
14	$H + 2\,O_2 \rightleftarrows HO_2 + O_2$	$3.00 \cdot 10^{14}$	-1.72	0.0
15	$H + H_2O + O_2 \rightleftarrows H_2O + HO_2$	$9.38 \cdot 10^{12}$	-0.76	0.0
16	$H + O_2 \rightleftarrows O + OH$	$8.30 \cdot 10^{10}$	0.00	7252.9
17	$2\,H + M \rightleftarrows H_2 + M$	$1.00 \cdot 10^{15}$	-1.00	0.0
18	$2\,H + H_2 \rightleftarrows 2\,H_2$	$9.00 \cdot 10^{10}$	-0.60	0.0
19	$2\,H + H_2O \rightleftarrows H_2 + H_2O$	$6.00 \cdot 10^{13}$	-1.25	0.0
20	$CO_2 + 2\,H \rightleftarrows CO_2 + H_2$	$5.50 \cdot 10^{14}$	-2.00	0.0
21	$H + OH + M \rightleftarrows H_2O + M$	$2.20 \cdot 10^{19}$	-2.00	0.0
22	$H + HO_2 \rightleftarrows H_2O + O$	$3.97 \cdot 10^{09}$	0.00	337.7
23	$H + HO_2 \rightleftarrows H_2 + O_2$	$2.80 \cdot 10^{10}$	0.00	537.4
24	$H + HO_2 \rightleftarrows 2\,OH$	$1.34 \cdot 10^{11}$	0.00	319.5
25[a]	$CH_3 + H\,(+M) \rightleftarrows CH_4\,(+M)$	$1.27 \cdot 10^{13}$	-0.63	192.7
		$2.48 \cdot 10^{30}$	-4.76	1227.9
26	$CH_4 + H \rightleftarrows CH_3 + H_2$	$6.60 \cdot 10^{05}$	1.62	5454.9
27[a]	$H + HCO\,(+M) \rightleftarrows CH_2O\,(+M)$	$1.09 \cdot 10^{09}$	0.48	-130.8
		$1.35 \cdot 10^{21}$	-2.57	717.1
28	$H + HCO \rightleftarrows CO + H_2$	$7.34 \cdot 10^{10}$	0.00	0.0
29	$CH_2O + H \rightleftarrows H_2 + HCO$	$2.30 \cdot 10^{08}$	1.05	1648.0
30[a]	$CO + H_2\,(+M) \rightleftarrows CH_2O\,(+M)$	$4.30 \cdot 10^{04}$	1.50	40056.2
		$5.07 \cdot 10^{24}$	-3.42	42446.5
31	$H_2 + OH \rightleftarrows H + H_2O$	$2.16 \cdot 10^{05}$	1.51	1726.0
32	$2\,OH \rightleftarrows H_2O + O$	$3.57 \cdot 10^{01}$	2.40	-1061.8
33	$HO_2 + OH \rightleftarrows H_2O + O_2$	$2.90 \cdot 10^{10}$	0.00	-251.6
34	$CH_4 + OH \rightleftarrows CH_3 + H_2O$	$1.00 \cdot 10^{05}$	1.60	1570.0
35	$CO + OH \rightleftarrows CO_2 + H$	$4.75 \cdot 10^{04}$	1.23	35.2
36	$HCO + OH \rightleftarrows CO + H_2O$	$5.00 \cdot 10^{10}$	0.00	0.0
37	$CH_2O + OH \rightleftarrows H_2O + HCO$	$3.43 \cdot 10^{06}$	1.18	-224.9
38	$CH_3 + HO_2 \rightleftarrows CH_4 + O_2$	$1.00 \cdot 10^{09}$	0.00	0.0
39	$CO + HO_2 \rightleftarrows CO_2 + OH$	$1.50 \cdot 10^{11}$	0.00	11876.0
40	$CH_3 + O_2 \rightleftarrows CH_2O + OH$	$3.60 \cdot 10^{07}$	0.00	4498.8
41	$CH_3 + HCO \rightleftarrows CH_4 + CO$	$2.65 \cdot 10^{10}$	0.00	0.0
42	$CH_2O + CH_3 \rightleftarrows CH_4 + HCO$	$3.32 \cdot 10^{00}$	2.81	2948.9
43	$H_2O + HCO \rightleftarrows CO + H + H_2O$	$2.24 \cdot 10^{15}$	-1.00	8554.7
44	$HCO + M \rightleftarrows CO + H + M$	$1.87 \cdot 10^{17}$	-1.00	8554.7
45	$HCO + O_2 \rightleftarrows CO + HO_2$	$7.60 \cdot 10^{09}$	0.00	201.3
46	$CH_3 + OH \rightleftarrows CH_2O + H_2$	$8.00 \cdot 10^{09}$	0.00	0.0

[a] Fall–off reaction. k_{f0} and k_∞ Arrhenius coefficients are reported in the first and second row, respectively.

Having as a starting point the detailed chemical kinetics for oxygen–methane mixtures at high pressures developed by Zhukov [118], this second reaction mechanism is a result of a reduction strategy employing an algorithm based on the CSP (computational singular perturbation) theory. It should be noted that the reduction strategy presented in Ref. [117] gave birth to a family of skeletal reaction mechanism, with different number of species and reactions and, thus, with different accuracies. The decision to choose exactly that shown in Table. 2, which is neither the most accurate nor the least, comes from the reasonable compromise between the accuracy it showed during validation and computational cost increase with respect to the global mechanism. Therefore, the selected skeletal reaction mechanism, hereafter referred to as "TSR-CDF-13" (tangential stretching rate - counterflow diffusion flame-13) retains the same species of the JL–R global mechanism, with the addition of further four, namely HO_2, CH_3, HCO, and CH_2O, for a total of 13 species and 46 reactions. The reaction set includes 10 three–body reactions (efficiencies are reported in Table 3) and 3 fall-off reactions. The latter rely on two sets of Arrhenius coefficients, and thus on two premilinary reaction rates k_{f0} and k_∞, for the determination of the actual reaction rate k_f. For further details the interested reader may consult Refs. [119–121].

Table 3: Third-body efficiencies associated to the TSR-CDF-13 skeletal reaction mechanism [117]. Provided only for reactions involving a third body M.

j	Reaction	$\hat{\alpha}_{CH_4}$	$\hat{\alpha}_{CO}$	$\hat{\alpha}_{CO_2}$	$\hat{\alpha}_{H_2}$	$\hat{\alpha}_{H_2O}$	$\hat{\alpha}_{O_2}$
1	$2O + M \rightleftharpoons O_2 + M$	2.00	1.75	3.60	2.40	15.40	1.00
2	$H + O + M \rightleftharpoons OH + M$	2.00	1.50	2.00	2.00	6.00	1.00
7	$CO + O + M \rightleftharpoons CO_2 + M$	2.00	1.50	3.50	2.00	6.00	6.00
13	$H + O_2 + M \rightleftharpoons HO_2 + M$	1.00	0.75	1.50	1.00	0.00	0.00
17	$2H + M \rightleftharpoons H_2 + M$	2.00	1.00	0.00	0.00	0.00	1.00
21	$H + OH + M \rightleftharpoons H_2O + M$	2.00	1.00	1.00	0.73	3.65	1.00
25	$CH_3 + H + M \rightleftharpoons CH_4 + M$	2.00	1.50	2.00	2.00	6.00	1.00
27	$H + HCO + M \rightleftharpoons CH_2O + M$	2.00	1.50	2.00	2.00	6.00	1.00
30	$CO + H_2 + M \rightleftharpoons CH_2O + M$	2.00	1.50	2.00	2.00	6.00	1.00
44	$HCO + M \rightleftharpoons CO + H + M$	2.00	1.50	2.00	2.00	0.00	1.00

The TSR-CDF-13 reaction mechanism has been specifically developed to deal with the CFD analysis of rocket engines thrust chambers. Moreover, it has been validated at four different operating pressures ranging from 20 to 450 bar, showing good agreement with data provided by Zhukov's detailed mechanism [118].

The RANS equations are numerically integrated up to the wall by an in-house CFD solver that has been validated in different operating conditions [116, 122–128]. The solver adopts a finite volume Godunov-type formulation. To allow a second-order accuracy in space, a linear cell reconstruction of flow variables is carried out by using the value in the considered cell and those in the contiguous ones. A Roe approximate Riemann solver [129] for multi-block structured meshes is used. This allows to evaluate variables at cell inter-

faces and associated fluxes to compute the evolution in time. Time integration adopts the Strang operator-splitting technique [130]: convective and diffusive terms are integrated by a second-order Runge-Kutta scheme, whereas for the chemical source terms a stiff ordinary differential equation implicit integrator is used [131].

2.2 THERMAL RADIATION MODELLING

The thermal radiation modelling strategy relies on the main assumptions of gray/diffuse wall and of gray/non–scattering medium, which are justified in the following. The global treatment of spectral features, leading to the assumption of gray wall, is deemed to be quite accurate given its fair independence from wavelength over the spectrum. The constraint on computer time restricts the choice to the gray assumption also for the gas, enabling to compute a single radiative intensity. The absence of solid particles suspended in the gas phase, finally, is consistent with the assumption of a non–scattering behavior of the medium, and the effect of soot radiation is not accounted for in the present study. It is also assumed that radiation does not affect the flow field significantly [132], because of the relative small weight of the wall heat transfer, and in particular of the radiative contribution, as compared to the whole thermal power generated within the thrust chamber. This assumption allows to evaluate the radiative heat flux only at the boundaries, and to neglect its contribution into the energy conservation equation.

The incident radiative heat flux $q_{g,rad}$ reaching a specific wall location is defined by the integral of the wall radiative intensity $\mathcal{I}_w$ over the hemispherical solid angle facing the incoming radiation:

$$q_{g,rad} = \int_{4\pi} \mathcal{I}_w \sin\theta \, d\Omega = \int_0^{2\pi} \int_0^{\frac{\pi}{2}} \mathcal{I}_w \sin\theta \cos\theta \, d\theta \, d\psi \tag{10}$$

where Ω is the solid angle, and θ and ψ are the line–of–sight elevation and azimuth angle, respectively. The radiative intensity at the wall from a generic line–of–sight can be computed by integrating the radiative transfer equation (RTE) along the whole radiation path length. The RTE expresses the balance of radiative intensity along a generic direction, including contributions due to absorption/emission and, potentially, in/out–scattering. Under the assumption of gray/non–scattering medium, the RTE reduces to the form

$$\frac{d\mathcal{I}}{ds} = j^e - \kappa \mathcal{I} \tag{11}$$

where j^e is the power per unit volume emitted by the gas, κ is the absorption coefficient, and s is the abscissa along a line–of–sight. The term j^e can be expressed as proportional to the black–body radiative intensity through a proportionality constant for emission equal to the absorption coefficient, i.e.

$j^e = \kappa\sigma T^4/\pi$, where σ is the Stefan–Boltzmann constant. The RTE formal solution can then be obtained as

$$\mathcal{I}_w = \mathcal{I}_{w,0}\ \exp\left(-\int_{s_{w,0}}^{s_w} \kappa\, ds\right) + \int_{s_{w,0}}^{s_w} j^e\ \exp\left(-\int_{s}^{s_w} \kappa\, ds'\right)\ ds \tag{12}$$

where the line–of–sight originates from another wall point (indicated with the subscript 0).

Equations (10) and (12) require the knowledge of radiative intensity at the line–of–sight origin $\mathcal{I}_{w,0}$ and of the absorption coefficient of the gas mixture κ to be solved. The former, under the assumption of gray/diffuse wall, can be simply evaluated taking into account both the emitted and reflected radiative intensity:

$$\pi\, \mathcal{I}_{w,0} = \epsilon_{w,0}\sigma T_{w,0}^4 + (1-\epsilon_{w,0}) q_{g,rad,0} \tag{13}$$

The latter is derived by means of a global model, typically used for high–temperature combustion mixtures under vibrational equilibrium conditions:

$$\kappa = p \sum_{i=1}^{N} \chi_i \kappa_{p,i} \tag{14}$$

indicating that the absorption of radiative energy is proportional to the pressure and to the absorption coefficients of the participating species weighted with their molar fraction χ_i. Note that $\kappa_{p,i} = 0$ except for H_2O, CO_2, and CO, which are the most relevant in the process of thermal radiation exchange [133, 134]. Radiation from hydroxyls, widely exploited for combustion diagnostics, is not considered relevant under the energetic standpoint for rocket chamber conditions, despite the non–negligible OH concentrations [135, 136]. The absorption coefficients averaged over the whole spectrum, i.e. the Planck mean absorption coefficients, are obtained from the model of [135]. This model, not explicitly accounting for high–pressure effects, does admittedly leave some uncertainty, which is however deemed of a weight comparable to those implied by other aspects of the model.

In the present work, the RTE is integrated with the discrete transfer method (DTM) using an in–house software for generic axisymmetric gray/diffuse boundaries and inhomogeneous gray/non–scattering media. The software was suitably developed, validated, and applied for convective and radiative heat flux comparisons in [122, 124]. For DTM simulations, a discretization consisting in 256 rays for each calculation point and a step of 1 mm along each ray have been used after performing convergence analyses for both parameters. Moreover, a wall emissivity equal to 0.91 has been assumed. The outlet section is modeled as an open surface, neglecting its contribution of emission and reflection.

Once the incident radiative heat flux is obtained with Eq. (10), the net radiative wall heat flux can be computed with

$$q_{w,rad} = \epsilon_w (q_{g,rad} - \sigma T_w^4) \tag{15}$$

where the first term on the right hand side is the absorbed heat flux, according to Kirkhoff's law, and the last is the emitted heat flux according to the corresponding total black–body emissive power σT_w^4. Equation (15) shows that $q_{w,rad}$ depends on the gas properties (see Eq. (10)), on the wall temperature, and on the wall properties (ϵ_w and $\mathcal{J}_{w,0}$, see Eq. (13)).
The field and wall local parameters needed by the code are recovered from the CFD solution, which is given to the radiation software as input.

3 FILM COOLING LOW–ORDER MODELING

The prediction of gaseous and, especially, liquid film cooling is a demanding procedure in terms of modelling and computational cost, hence discouraging when an entire rocket system has to be simulated and analyzed in detail. Propulsion system simulators tend to privilege the essential features of a rocket engine, for instance combustion and expansion processes, which are necessary to provide a first order prediction of engine performances. As far as cooling systems are concerned, regenerative cooling is usually considered as the main technique employed to provide thermal protection to chamber walls. However, the numerical simulation of the regenerative cooling system alone may not be sufficiently realistic and accurate in heat transfer analysis of modern LREs, as already mentioned in Sec. 1.2. As a consequence, the feature for a LRE system simulator to handle film cooling predictions is becoming more and more interesting and necessary. For those reasons, suitable modelling has been searched and then selected among the few choices available in the literature, aiming at extending the capabilities provided by LRE design tools for system analysis. Choosing criteria were the compatibility with the EcosimPro/ESPSS software paradigm and capabilities, but also the possibility of having formulations not so computationally heavy to generate bottlenecks in the system simulations. In this regard, the EcosimPro/ESPSS framework is a state–of–the–art object–oriented visual simulation tool, which allows the propulsion system to be assembled by connecting the individual components available in the software (pipes, valves, turbomachinery, cooling jackets, thrust chamber, etc.). Furthermore, it allows to design and develop brand–new components to be included in the model.

In this chapter, the detailed description and the implementation strategy of the models selected as best candidates to be included as brand–new components into the EcosimPro/ESPSS platform modelling both liquid and gaseous film–cooled LRE thrust chambers are presented. Because of the nature of the framework itself, different categories of models which can deliver results with different orders of accuracy with respect to the investigated phenomena have been selected, thus involving different computational efforts. Therefore, different levels of approximation might be considered, if needed.

3.1 LIQUID FILM COOLING MODELS

Different models have been considered with their pros and cons for liquid film cooling [55, 57]. They are mostly based on empirical formulations and several simplifying hypotheses are usually retained to have a compromise between accuracy and computational effort due to the highly complex phenomena which are occurring.

3.1.1 Grisson full formulation

Grisson's model [55] is a one–dimensional differential model of liquid film cooling in liquid rocket engine combustion chambers. The main purpose of the model is to calculate the coolant evaporation rate due to heating and, accordingly, to estimate the size of the film–cooled region, referred to as FCL (*film cooled length*). Radiative heating to the liquid film is considered in the model. Grisson's complete model also assumes that a portion of the evaporated coolant continues to provide a (lesser) thermal protection due to its entrainment into the boundary layer. Limitations exist for this model, e.g., since liquid droplets entrainment into the hot gas stream is neglected, a greater error should be expected when dealing with significant mass flow rates. Moreover, the effect of boundary–layer gases acceleration is neglected as well, therefore lower accuracy is expected in the nozzle as well, where a correction factor applies only for the convergent part.

Right after injection, the coolant is assumed to heat up until saturation conditions due to heat exchange with the hot gases. The convective heat transfer coefficient is calculated according to the flat plate correlation by Chilton and Colburn [137], thus involving the hot gas properties:

$$C_{f,0} = 0.0592\ Re_x^{-0.2} \tag{16}$$

$$St_0 = \frac{1}{2} C_{f,0}\ Pr^{-0.6} \tag{17}$$

$$h_0 = K_t\ G_{mean}\ c_{p,g}\ St_0 \tag{18}$$

$$G_{mean} = \rho_g u_g \left(\frac{u_g - u_{liq}}{u_g} \right) = \rho_g (u_g - u_{liq}) \tag{19}$$

where $C_{f,0}$ is the skin friction factor, Re_x is the abscissa–based hot gas Reynolds number, St_0 is the Stanton number, Pr is the Prandtl number of the hot gases, and h_0 is the dry–wall convective heat transfer coefficient between the hot gas and the liquid film, i.e. not accounting for transpiration effects. $K_t = 1 + 4e_t$ is a correction factor for turbulence (function of the RMS turbulence fraction e_t) and G_{mean} is the hot gas mass flow per unit area, evaluated at the mean temperature between the gas and the liquid film and accounting also for the coolant velocity. Typical values of e_t measured in liquid rocket engines are in

the range 0.05 – 0.2. Once h_0 is obtained, the convective heat exchange between the hot gas and the liquid film is evaluated as $q_{conv,film} = h_0(T_g - T_{liq})$. The convective heat exchange between the film and the walls $q^{wall}_{conv,film}$ is evaluated using the same procedure while considering the liquid coolant properties:

$$q^{wall}_{conv,film} = h^{wall}_{film}\,\Delta T = 0.0296\left(\frac{x}{k_{liq}}\right) Re^{0.8}_{x,liq}\, Pr^{0.33}_{liq}\,(T_{liq} - T_{wall}) \tag{20}$$

where x is the local abscissa and k_{liq} is the liquid coolant thermal conductivity. Then, the radiative heat flux towards the liquid film is calculated as:

$$q_{rad,film} = \sigma\, A_w\, \epsilon_g\,(T_g^4 - T_{liq}^4) \tag{21}$$

where σ is the Stefan–Boltzmann constant and A_w is the absorptivity of the chamber wall, which can be set as a free parameter.
The hot gas total emittance ϵ_g is evaluated by the model. According to Grisson's model only water and carbon dioxide are supposed to give a contribution to the hot gas total emittance, thus:

$$\epsilon_{H_2O} = 0.825\left(1 + \left(\frac{\rho_{opt,H_2O}}{c_{H_2O}}\right)^{-n_{H_2O}}\right)^{-\frac{1}{n_{H_2O}}} \tag{22}$$

$$\epsilon_{CO_2} = 0.231\left(1 + \left(\frac{\rho_{opt,CO_2}}{c_{CO_2}}\right)^{-n_{CO_2}}\right)^{-\frac{1}{n_{CO_2}}} \tag{23}$$

where $\rho_{opt,H_2O} = p\, y_{H_2O}\, L_{eff}$ and $\rho_{opt,CO_2} = p\, y_{CO_2}\, L_{eff}$ are the optical densities, $L_{eff} = 0.95\, D_c\, A_w^{-0.85}$ is a reference length, and c and n are coefficients which are tabulated as a function of temperature and the chemical species.

A high-pressure correction (pressure higher than 1 bar) is applied by multiplying both the emissivities by a factor K_p:

- H_2O

$$K_{pH_2O} = 1 + c_1\left(1 - exp\left(\frac{1 - p(1 + \chi_{H_2O})}{c_2}\right)\right) \tag{24}$$

$$c_1 = 0.26 + 0.74\, exp(-2.5\,\rho_{H_2O}) \tag{25}$$

$$c_2 = 0.75 + 0.31\, exp(-10\,\rho_{H_2O}) \tag{26}$$

- CO_2

$$\log_{10}(K_{pCO_2}) = 0.036\,\rho_{CO_2}^{-4.33}(1 + (2\log_{10}(p))^{-100\rho_{CO_2}})^{-\frac{1}{100\rho_{CO_2}}} \tag{27}$$

where ρ_{H_2O} and ρ_{CO_2} are the water and carbon dioxide partial densities respectively, and χ_{H_2O} is the mole fraction of water in the mixture. An additional

correction $\Delta\epsilon$ is necessary to account for overlaps in the two spectra for temperatures higher than 1200 K (see Ref. [55] for further details):

$$\Delta\epsilon = \begin{cases} 0.0551\, K_x(1-exp(-4\rho_{opt}))(1-exp(-12.5\rho_{opt})) & \text{if } T \geqslant 1200\,K \\ 0 & \text{otherwise} \end{cases} \tag{28}$$

$$K_x = 1 - \left|\frac{2\chi_{H_2O}}{\chi_{H_2O}+\chi_{CO_2}}\right|^n \tag{29}$$

$$n = 5.5(1+(1.09\rho_{opt})^{-3.88})^{-\frac{1}{3.88}} \tag{30}$$

where $\rho_{opt} = \rho_{optH_2O} + \rho_{optCO_2}$ and χ_{CO_2} is the mole fraction of carbon dioxide in the mixture. The total gas emissivity is then:

$$\epsilon_g = \epsilon_{H_2O}\, K_{pH_2O} + \epsilon_{CO_2}\, K_{pCO_2} - \Delta\epsilon \tag{31}$$

Once the radiative heat flux to the film is known, the radiation at the wall is calculated as:

$$q_{rad,wall} = q_{rad,film}\, e^{-\alpha\, t} \tag{32}$$

$$t = \frac{2\,\mu_{liq}\,\Gamma}{\rho_{liq}\,\tau_{w,0}} \tag{33}$$

where α is an averaged liquid absorptivity (free parameter), t is the liquid film thickness, μ_{liq} and ρ_{liq} are the dynamic viscosity and the density of the liquid film respectively, Γ is the coolant mass flow rate per unit chamber circumference, and $\tau_{w,0}$ is the dry–wall shear stress (calculated from $C_{f,0}$). The exponential term in Eq. (32) represents the fraction of radiation transmitted through the liquid film. The total heat flux, obtained summing up the convective and radiative contributions, is absorbed by the liquid film, causing a temperature rise:

$$\frac{\Delta T}{\Delta x} = \frac{q_{tot,film}}{\Gamma\, c_{p,liq}} \tag{34}$$

After the liquid reaches the saturation temperature, the evaporation rate per unit area is:

$$\dot{m}_{vap} = \frac{Q_{conv,film} + Q_{rad,film} + Q^{wall}_{conv,film}}{\lambda} \tag{35}$$

where λ is the coolant latent heat of vaporization. This vapor flows away from the liquid film, similar to liquid transpiration through a porous wall, thus decreasing the dry–wall shear stress $\tau_{w,0}$ and convective heat transfer coefficient h_0. To take this phenomenon into account, a new convective heat transfer coefficient h (and a new wall shear stress τ_w, actually not used in the model) is calculated from the dry–wall one by means of a transpiration correction:

$$\frac{h}{h_0} = \frac{\ln(1+H)}{H} \tag{36}$$

$$H = \frac{K_m\, c_{p,g}}{\lambda}\left[(T_g - T_{sat}) + \frac{q_{rad,film}}{h}\right] = \frac{K_m\, c_{p,g}\, \dot{m}_{vap}}{h} \tag{37}$$

where K_m is a function of hot gas and coolant molar masses $\mathcal{M}$:

$$K_m = \begin{cases} (\mathcal{M}_g/\mathcal{M}_{film})^{0.6} & \text{if } \mathcal{M}_g \geqslant \mathcal{M}_{film} \\ (\mathcal{M}_g/\mathcal{M}_{film})^{0.35} & \text{otherwise} \end{cases} \tag{38}$$

Given the non–linear nature of the dependencies, an iterative procedure is required to calculate $\dot{m}_{vap}$, h, and H. Once the evaporation rate is known, it decreases the liquid mass flow rate per unit circumference at a rate:

$$\frac{\Delta\Gamma}{\Delta x} = -\dot{m}_{vap} \tag{39}$$

The FCL is hence determined as the abscissa at which $\Gamma = 0$.

Starting from the position marked as FCL it is assumed that the whole coolant mass remains in the boundary layer (see Fig. 3a), which grows and heats up due to the free stream entrainment. Note that all the mass flow rates involved in this gaseous film cooling formulation, indicated as $\dot{M}$, are intended per unit length of chamber circumference, hence units are $kg/(s \cdot m)$.

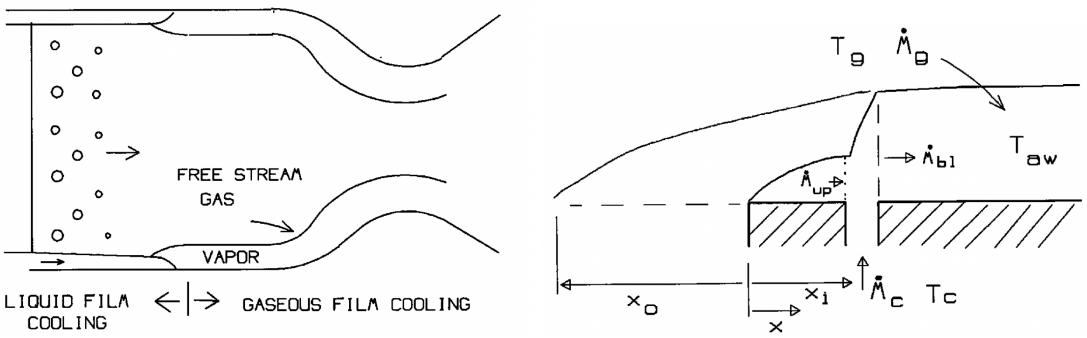

(a) (b)

Figure 3: Grisson model boundary layer treatment schematics [55].

The mass flow rate increase in the boundary layer at the i–th grid node due to free stream entrainment is:

$$\Delta\dot{M}_e = 0.1963\, K_t\, G \left(\frac{\mu_g}{\dot{M}_{bl,i}}\right)^{-0.25} \Delta x \tag{40}$$

where the mass flow per unit area G is now calculated as the chamber value $\rho_g u_g$ scaled by the local area ratio A_c/A. $\dot{M}_{bl,i}$ is the gaseous mass flow rate in the boundary layer at the i–th grid node. When calculated for the first time, the latter is defined as a function of the actual film mass flow rate (equal to the initial value of Γ) and of an effective leading–edge abscissa X_0 used to obtain a proper boundary layer growth rate [91] (see Fig. 3b):

$$\dot{M}_{bl,1} = 0.325\,\Gamma(FCL + X_0) = 0.325\,\Gamma(3.08 + FCL^{0.8}) \tag{41}$$

A further term is used to consider the chamber contraction in the convergent part of the nozzle:

$$\Delta\dot{M}_c = -\dot{M}_{bl,i}\,\frac{\Delta D_{c,i}}{D_{c,i}} \tag{42}$$

where D_i is the local chamber diameter, and $\Delta D_{c,i} = D_{c,i-1} - D_{c,i}$. Therefore, the mass flow rate in the boundary layer at the next step $i+1$ is calculated as:

$$\dot{M}_{bl,i+1} = \dot{M}_{bl,i} + \Delta\dot{M}_e + \Delta\dot{M}_c \tag{43}$$

Note that the boundary–layer mass flow rate increase is limited by the total chamber mass flow rate.
On the other hand, the temperature increase in the boundary layer is computed as:

$$\Delta T_e = \Delta\dot{M}_e(T_r - T_{bl,i})\left[\dot{M}_{bl,i} + \Gamma\left(\frac{1}{K_m}\,\frac{c_{p,c}}{c_{p,g}} - 1\right)\right]^{-1} \tag{44}$$

and radiation from hot gases:

$$\Delta T_{rad} = \left(\frac{q_{rad}}{c_{p,g}\,\dot{M}_{bl,i}}\right) \tag{45}$$

where T_r is the recovery temperature, and $c_{p,c}$ is the gaseous coolant specific heat at constant pressure calculated at the boundary layer temperature $T_{bl,i}$. Eventually, the boundary layer temperature at the next grid node is calculated as:

$$T_{bl,i+1} = T_{bl,i} + \Delta T_e + \Delta T_{rad} \tag{46}$$

Once the boundary layer temperature is obtained, the convective heat transfer coefficient between the boundary layer and the wall is calculated according to the Chilton–Colburn correlation:

$$h_{bl,i} = 0.0296\,K_t\,G\,c_{p,c}\left(\frac{G(x_i - FCL + X0/K)}{\mu_c}\right)^{-0.2}\left(\frac{\mu_c\,c_{p,c}}{k_c}\right)^{-0.6} \tag{47}$$

where x_i is the local abscissa, and μ_c and k_c are respectively the gaseous coolant dynamic viscosity and thermal conductivity calculated at the boundary layer temperature $T_{bl,i}$. It should be noted that this convective heat transfer coefficient is calculated using the pure coolant properties. This represents a modelling approximation since the coolant is mixed with the hot gas in the boundary layer, resulting in a mixture with different chemical composition, and thus with intermediate properties between the mainstream and the coolant itself. A more realistic approach would foresee the mixing between the two flows at each chamber node prior to the calculation of the convective heat transfer coefficient. However, such a procedure would involve several further calculation steps, hence increasing significantly the computational burden which is already moderate due to the complex phenomenology entailed by liquid film cooling. For those reasons, the assumption is considered acceptable.

3.1.2 Grisson simplified formulation

Grisson [55] also provided a simplified 0–dimensional analytical formulation of his model to avoid the iterative calculation of the evaporation rate and the transpiration–corrected convective heat transfer coefficient. They can be obtained explicitly by neglecting the term $q_{rad,film}$ in Eq. (37). In fact, without radiation the transpiration correction reduces to a simple form:

$$\frac{h}{h_0} = \frac{\ln(1+H)}{H} \tag{48}$$

$$H = \frac{K_m \, c_{p,g}}{\lambda^*}(T_g - T_{sat}) \tag{49}$$

where the latent heat of vaporization λ^* includes also the contribution yielded by coolant heating from the injection temperature T_{liq} to the saturation point T_{sat}:

$$\lambda^* = \lambda + c_{p,liq}(T_{sat} - T_{liq}) \tag{50}$$

The FCL is then calculated without the necessity of integrating along the chamber abscissa:

$$FCL = \frac{61.62\,\mu_g}{G_{mean}} \left[\frac{\lambda^* \, \Gamma}{c_{p,g}(T_g - T_{sat})\,\mu_g (h/h_0)} \right]^{1.25} Pr^{0.75} \tag{51}$$

Eventually, the convective heat transfer coefficients h and h_0 are calculated using Eq. (48), Eq. (49), and the Stanton number St_0:

$$St_0 = 1.25 \left[0.0296 \left(\frac{G_{mean}\, FCL}{\mu_g} \right)^{0.2} Pr^{-0.6} \right] \tag{52}$$

Due to the simplified nature of this model, the wall region covered by the liquid film has been supposed as adiabatic, so the term $q^{wall}_{conv,film}$ is neglected. The gaseous formulation does not change from the full Grisson model, since the hot–gas radiation can be retained during the boundary layer calculations without drastically increase model computational heaviness.

3.1.3 Shine et al.

Shine et al. model [57], hereafter *Shine* for the sake of brevity, is a 0–dimensional analytical model of liquid film cooling in LREs combustion chambers operating at subcritical conditions, which incorporates hot gas radiation and the entrainment of the liquid phase into the gas. The approach involves the modelling of the liquid phase as a control volume with constant properties (see Fig. 4), and the evaporation is calculated by means of mass and energy balances. Mass transfer via entrainment is obtained employing the numerical correlation by Sawant et al. [49]. The logic behind the calculation of the evaporation rate and

the convective heat transfer coefficient is similar to that of Grisson, with slight modifications.

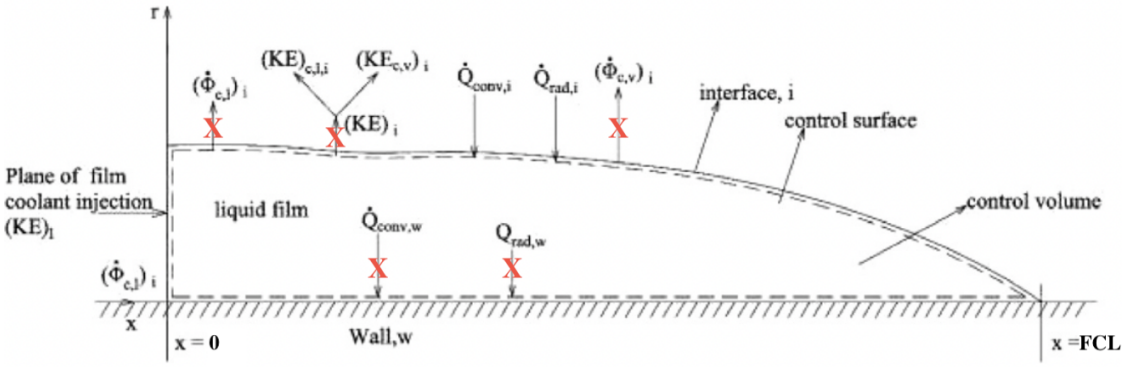

Figure 4: Schematic of the control volume and heat contributions used by Shine et al. [57].

As shown in Fig. 4, the control volume exchanges energy with the wall and with the hot gases. The model includes convection and radiation at the interface of liquid film with combustion gas, the contribution of enthalpy and kinetic energy carried by coolant vapor, and the entrainment of the liquid phase in the mainstream. In most cases, the kinetic energy contributions and radiation at the wall can results negligible in comparison to the other contributions. Moreover, the increasing liquid phase enthalpy is neglected as well, in the control volume, thus assuming the liquid phase heating process from the injection temperature to the saturation value as instantaneous. In such a way, an overall vaporization enthalpy can be defined as already done in Eq. (50) for the simplified Grisson model. The convective heat transfer to the wall is neglected, thus considering the chamber wall as adiabatic. All the neglected terms are crossed-out in Fig. 4. In the end, the total heat flux exchanged by the control volume is just $q_{tot,film} = q_{conv,film} + q_{rad,film}$. The evaporation process is modelled similarly to Grisson model (see Sec. 3.1.1), i.e., calculating a dry–wall convective heat transfer coefficient h_0 and then introducing the transpiration correction to obtain h. In the Shine model, the dry–wall quantities are obtained starting from the implicit calculation of the Darcy friction factor f_D:

$$\frac{1}{\sqrt{f_D}} = 1.93 \log_{10}(Re_g \sqrt{f_D}) - 0.537 \tag{53}$$

$$St_0 = \frac{f_F/2}{1.20 + 11.8\sqrt{f_F/2}\,(Pr - 1)\,Pr^{-0.33}} \tag{54}$$

$$h_0 = G_{mean}\, c_{p,g}\, St_0\, K_t \tag{55}$$

where $f_F = f_D/4$ is the Fanning friction factor, G_{mean} is defined as in Eq. (19), and Re_g is the hot–gas chamber diameter–based Reynolds number. The radiative heat flux towards the liquid film is calculated as $q_{rad,film} = \sigma \epsilon_g (T_g^4 - T_{sat}^4)$.

The total hot gas emittance is evaluated through the Leckner correlation [58], whose details are provided in the following. According to Leckner, and similarly to the method used by Grisson, only the partial emittances of water and carbon dioxide participate to the total mixture emittance, which is a function of temperature, pressure, and chamber geometry:

$$\epsilon(T, pL_e) = exp\left\{ a_0 + \sum_{j=1}^{M} a_j \, [\log_{10}(pL_e)]^j \right\} \tag{56}$$

$$a_j = c_{0j} + \sum_{i=1}^{N} c_{ij} \left(\frac{T}{1000} \right)^i \tag{57}$$

where p is the partial pressure of water or carbon dioxide, L_e can be reasonably assumed equal to the chamber length, and coefficients M, N, and c are tabulated in Ref. [58] for temperatures higher than 400 K and depending on the chemical. Similarly to the Grisson model, a high–pressure correction is needed for the correct emissivity assessment. The correction factor can be casted as $C = 1 + \Xi(\Lambda - 1)$, where factors Λ and Ξ are different if water or carbon dioxide are concerned. Being $\hat{T} = T/1000$, the latter are defined as follows:

$$\Lambda_{H_2O} = \frac{\left[1.888 - 2.053 \log_{10}\left(\hat{T}\right)\right] P_{E,H_2O} + 1.10\,\hat{T}^{-1.4}}{P_{E,H_2O} + \left[1.888 - 2.053 \log_{10}\left(\hat{T}\right)\right] + 1.10\,\hat{T}^{-1.4} - 1} \tag{58}$$

$$\Lambda_{CO_2} = \frac{\left[1 + 0.1\,\hat{T}^{-1.45}\right] P_{E,CO_2} + 0.23}{P_{E,CO_2} + \left[1 + 0.1\,\hat{T}^{-1.45}\right] - 0.77} \tag{59}$$

$$\Xi_{H_2O} = exp\left\{ -\frac{1}{2} \left[\log_{10}\left(13.2\,\hat{T}^2\right) - \log_{10}\left(p_{H_2O}\, L_e\right) \right] \right\} \tag{60}$$

$$\Xi_{CO_2} = exp\left\{ -1.47 \, \left[\bar{\mu} - \log_{10}\left(p_{CO_2}\, L_e\right) \right] \right\} \tag{61}$$

$$\bar{\mu} = \begin{cases} \left(\log_{10}\left(0.225\,\hat{T}^2\right) & \text{if } T \geqslant 700K \\ \left(\log_{10}\left(0.054\,\hat{T}^{-2}\right) & \text{otherwise} \end{cases} \tag{62}$$

$$P_{E,H_2O} = p_0 \left[1 + 4.9 \left(\frac{p_{H_2O}}{p_0} \right) \sqrt{\frac{273}{T}} \right] \tag{63}$$

$$P_{E,CO_2} = p_0 \left[1 + 0.28 \left(\frac{p_{CO_2}}{p_0} \right) \right] \tag{64}$$

where T is the hot–gas temperature, p_{H_2O} and p_{CO_2} are water and carbon dioxide partial pressures respectively, and p_0 is the total pressure. The total emittance is then obtained as:

$$\epsilon_g = C_{H_2O}\, \epsilon_{H_2O} + C_{CO_2}\, \epsilon_{CO_2} - \Delta\epsilon \tag{65}$$

where the band overlap correction $\Delta\epsilon$ depends only on partial pressures and L_e:

$$\Delta\epsilon = \left(\frac{\zeta}{10.7 + 101\,\zeta} - 0.0089\,\zeta^{10.4} \right) [\log_{10}(p\,L_e)]^{2.76} \tag{66}$$

$$\zeta = \frac{p_{H_2O}}{p_{H_2O} + p_{CO_2}} \tag{67}$$

$$p = p_{H_2O} + p_{CO_2} \tag{68}$$

Note that the Leckner correlation assumes pressures in bar and L_e in cm.

The transpiration correction is calculated implicitly by means of the same procedure shown for the Grisson model. The Stanton number is used here, even if it should be noted that $St/St_0 = h/h_0$. Then the transpiration–corrected convective heat transfer coefficient is calculated from the transpiration–corrected Stanton number using $h = G_{mean}\,c_{p,g}\,St\,K_t$. The iterative procedure also returns the evaporation rate, which is calculated as:

$$\dot{m}_{vap} = \frac{Q_{conv,film} + Q_{rad,film}}{\lambda^*} \tag{69}$$

Note that the amount of vaporizing liquid might be lower than the amount of liquid injected since some portion of it might be entrained in the free stream. The correlation by Sawant et al. [49] is used to calculate this coolant loss, expressed as a fraction E of the injected mass flow rate Γ:

$$E = E_m \tanh\left(a\,We^{1.25}\right) \tag{70}$$

$$E_m = 1 - 250\,\frac{\ln\left(Re_{liq}\right) + 1265}{Re_{liq}} \tag{71}$$

$$a = 2.31 \cdot 10^{-4}\,Re_{liq}^{-0.35} \tag{72}$$

$$We = \frac{\rho_g\,u_g\,D}{\sigma\,(\Delta\rho/\rho_g)^{0.25}} \tag{73}$$

where Re_{liq} is the slot height–based coolant Reynolds number, We is the modified Weber number, σ is the liquid surface tension, E_m is a limiting entrained fraction determined empirically depending only on the Reynolds number, and $\Delta\rho$ is the density difference between the liquid and the gas phases. Knowing the entrained fraction E, the liquid mass flow rate available for film cooling is given by:

$$\Gamma_{av} = \Gamma\,(1 - E) \tag{74}$$

and the film cooled length is $FCL = \Gamma_{av}/\dot{m}_{vap}$.

Boundary layer model for film cooling in gaseous phase is retained from Grisson model (see Sec. 3.1.1).

3.2 GASEOUS FILM COOLING MODELS

The gaseous modelling relies on a quasi–2D reduced formulation [100], which has been revised in the framework of this Ph.D. research, increasing its robustness and extending the field of application to a larger spectrum of operating conditions. A numerical correlation was also derived by CFD results processing. The latter is characterized by a higher robustness than that of a reduced model, but its low versatility and narrow field of application let the reduced model be a better choice for parametric analyses. The support provided by CFD simulations and the high versatility of such a formulation when implemented in a numerical environment capable of handling system transients makes this gaseous film cooling reduced modelling implementation an original, useful, and important addition to systems simulators as EcosimPro to provide reliable predictions of liquid rocket engines heat loads.

3.2.1 Modified Simon – Di Matteo et al.

Gaseous film cooling model by Simon–Di Matteo et al. [100], then modified in the framework of this thesis, is a quasi–2D differential formulation to study the developed flowfield of a film–cooled rocket combustion chamber. The model is capable to provide a prediction of the evolution in space and time of the wall heat flux, retaining the geometry of the developed flowfield proposed by Simon [98] (see Fig. 5).

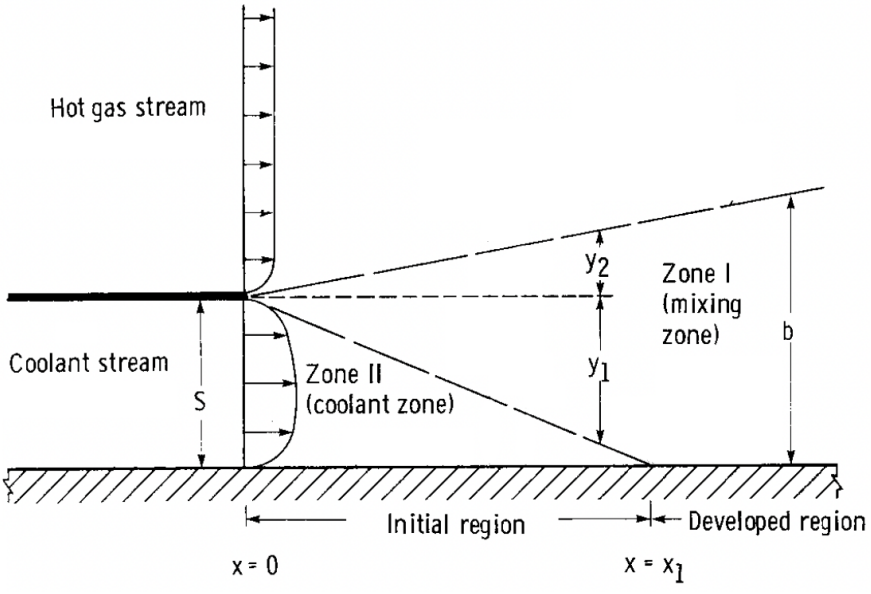

Figure 5: Geometry of the developed flowfield assumed by Simon [98].

The latter includes three different regions: the core (hot gases, subscript g), film (subscript *film*), and mixing region (subscript *mix*). The entrained mass flow rates and the quantities exchanged between the hot gas, the mixing, and

the film regions are computed by means of geometrical correlations. All the three zones are assumed to have the same pressure for any given cross–section of the combustion chamber, determined as no film cooling were present. The model assumes also that the mixing zone does not affect the film and hot gas flows, but it is a result of their interaction. As a result, the hot gas and film flows do not interact with each other anyhow, and the fluid properties in the mixing zone are determined according to a one–way dependency through the entrained hot gas and film mass and energy inflows.

The first step of the model is the calculation of the length of the film region x_1, also called *potential core length*. The latter defines the region characterized by coolant properties (the *initial region* in Fig. 5), so the convective heat flux is determined by the film conditions, whilst in the developed region the wall conditions are determined by the mixing conditions. The value of x_1 can be enforced, obtained by means of an iterative procedure as proposed in the original model [100], or calculated employing the CFD–based correlation developed during this Ph.D. research. The reason which led to extend the possibilities offered by the original model lays in its own limitations. In particular, the model by Simon–Di Matteo et al. had a narrow range of applicability, being valid only in the so–called *wall–jet* regime. The latter occurs in case $u_{film} > u_g$, which actually represents only a restricted group of possibilities in LRE gaseous film cooling design. For the sake of clarity, only the iterative procedure is presented in this section, while the numerical correlation is described in detail in Sec. 3.2.2.

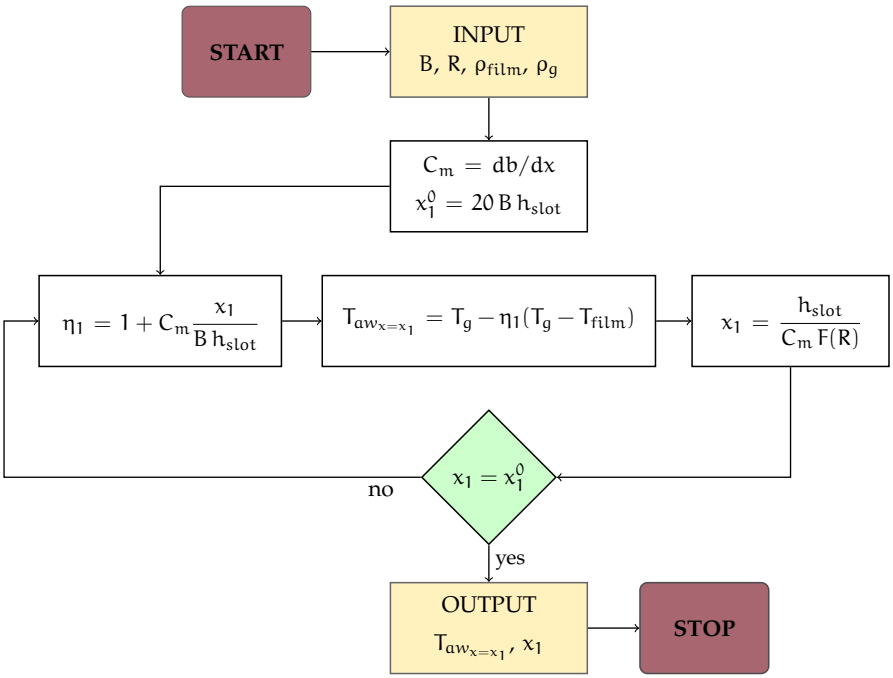

Figure 6: Iterative procedure for the calculation of the potential core length x_1.

The detailed flowchart of the iterative procedure for the calculation of x_1 proposed in the original model by Simon–Di Matteo et al. is shown in Fig. 6, where $B = (\rho u)_g / (\rho u)_{film}$ is the blowing ratio, R is the velocity ratio, defined in the following, h_{slot} is the film injection slot height, C_m is the mixing coefficient, which is equivalent to the mixing zone growth rate according to [98], T_{aw} is the adiabatic wall temperature, and $F(R)$ is the following function of the velocity ratio (see also Fig. 5):

$$F(R) = \frac{y_1}{y_2} = \frac{1}{\frac{\rho_{film}}{\bar{\rho}_{mix}\,(0.416 + 0.134\,R)} - 1} \tag{75}$$

The term $\bar{\rho}_{mix}$ is the average density of the mixing zone, which is calculated by means of the perfect gas equation of state using the temperature $T_{aw_{x=x_1}}$ (output of flowchart in Fig. 6) and the averaged gas constant between the hot gas and film regions. Moreover, the velocity ratio is defined as:

$$R = k_R \frac{u_g}{u_{film}} \tag{76}$$

where $k_R = Nb/2\pi r_c$ is a correction parameter accounting for discrete slot injection in the 1–D environment, being N the number of discrete slots, b the slot width, and r_c the combustion chamber radius. Concerning the mixing zone growth rate, it is given by:

$$\frac{db}{dx} = C_m = \pm c \frac{R-1}{R+1} \tag{77}$$

where c is a function of the density ratio ρ_g/ρ_{film} with positive sign if $R > 1$ or negative otherwise. Note that Eq. (77) can not be used if the velocity ratio equals 1, since it would provide an unrealistic null mixing zone growth.
Once the potential core length is known, it is possible to calculate the flowfield geometry, which depends on time but is constant at a fixed time instant. In particular, having Fig. 5 as a reference, the geometrical quantities at the i–th node are calculated as:

$$y_{1,i} = \frac{h_{slot}}{x_1} x_i \quad ; \quad y_{2,i} = \frac{db}{dx} x_i \tag{78}$$

$$A_{g,i} = \pi (r_{c0} - y_{2,i})^2 \tag{79}$$

$$A_{film,i} = \pi \left[r_c^2 - (r_{c0} + y_{1,i})^2 \right] \tag{80}$$

$$\begin{aligned} A_{mix,i} &= \pi \left[(r_{c0} + y_{1,i})^2 - (r_{c0} - y_{2,i})^2 \right] = \\ &= \pi r_c^2 - A_{g,i} - A_{film,i} \end{aligned} \tag{81}$$

where $r_{c0} = r_c - h_{slot}$ and A is the cross–section area of the specified flow region. The next step of the model is the integration of the differential equations. The least number of partial differential equations is included in the model, for simplicity, and different treatments are employed in the three regions of the flowfield as schematised below. All the quantities refer to those calculated in the specified flow region.

- Core

$$A\frac{\partial \rho}{\partial t} + \frac{\partial \rho u A}{\partial x} = 0 \tag{82}$$

$$A\frac{\partial \rho u}{\partial t} + \frac{\partial [(\rho u^2 + p)A]}{\partial x} = -\frac{1}{2}\frac{d\xi}{dx}\rho u\,|u|\,A + p\left(\frac{dA}{dx}\right) \tag{83}$$

$$A\frac{\partial \rho E}{\partial t} + \frac{\partial \rho u H A}{\partial x} = 0 \tag{84}$$

  All the three governing equations are retained for the core region. Note that the heat loss source term is not present in the energy equation since the core zone never gets in contact with the wall.

- Film

$$V\frac{\partial \rho e_0}{\partial t} + \frac{\partial \dot{m} h_0}{\partial x} = Q_{wall} \tag{85}$$

  In the film region only the energy equation is retained, where the integrated variable has to be intended as the product of film density and film total energy, being the former not provided by the mass conservation equation or other procedures. Similarly, due to the lack of the momentum conservation equation, the mass flow rate is supposed to be constant in space but variable in time, and equal to the value at the coolant injector, as if information propagate with infinite speed for a fixed time instant. Then, knowing mass flow rate and thus mass flux $G = (\dot{m}/A)_{film}$ also from the geometry, the film thermodynamic state is calculated iteratively according to the following steps:

  1. First–guess film density ρ_k;
  2. Calculation of the static and total energy e_k and $e_{0,k}$ from ρ_k, pressure, and G_{film};
  3. Evaluation of $(\rho e_0)_k$;
  4. Minimization of $\Delta(\rho e_0) = (\rho e_0)_k - (\rho \bar{e}_0)$, where $(\rho \bar{e}_0)$ is provided by Eq. (85);
  5. Evaluation of film density (ρ_{film}), velocity (u_{film}), and static enthalpy (h_{film}).

All the other film properties are calculated exploiting chamber pressure, which is the same for all regions, and film static enthalpy.

- Mixing zone

  No partial differential equations are retained in the mixing region.
  The thermodynamic state is obtained as a function of the geometry calculated initially and the core and film zone solutions. Details are provided in the following.

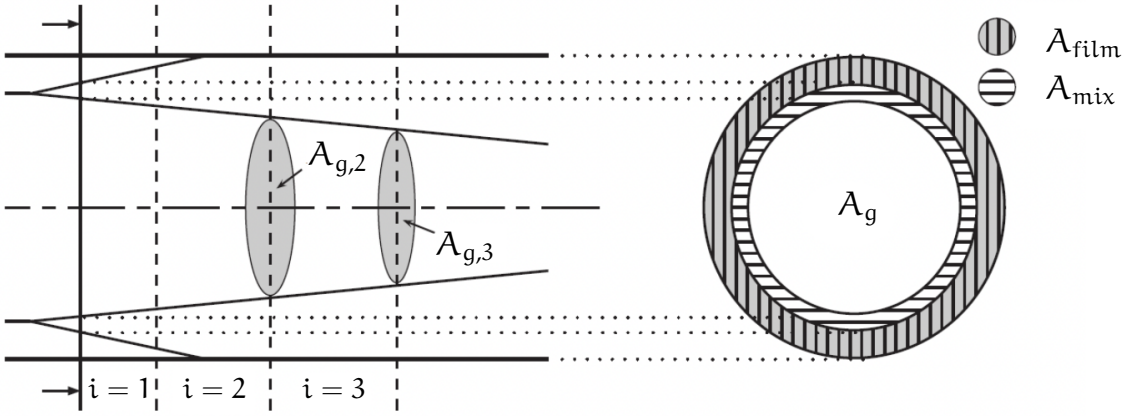

Figure 7: Flowfield geometry development as assumed by the gaseous film cooling model [100].

Mixing region properties are determined by those of the hot gas and the film in a one–way dependency, meaning that they can influence the mixing but not the other way around. Algebraic equations based on geometrical considerations and on the properties of the hot gas and the film are used to evaluate the incoming mass flow rates to the mixing region $\dot{m}_{C2M}$ (core to mixing) and $\dot{m}_{F2M}$ (film to mixing):

$$\dot{m}_{C2M} = (\rho u)_g \, A_{C2M} \tag{86}$$

$$\dot{m}_{F2M} = (\rho u)_{film} \, A_{F2M} \tag{87}$$

where the mass fluxes are known and the area terms represent the interface area between two adjacent regions, which are determined by the assumed geometry of the flow field calculated above and schematically shown in Fig. 7:

$$A_{C2M,i} = A_{g,i-1} - A_{g,i} \tag{88}$$

$$A_{F2M,i} = A_{film,i-1} - A_{film,i} \tag{89}$$

As a result, the mixing zone temperature at the i–th node is calculated by averaging all the incoming flow temperatures, using their mass flow rate as weights:

$$T_{mix,i} = \begin{cases} \dfrac{T_{g,i}\dot{m}_{C2M,i} + T_{film,i}\dot{m}_{F2M,i}}{\dot{m}_{C2M,i} + \dot{m}_{F2M,i}} & \text{if } i = 1 \\ \dfrac{T_{g,i}\dot{m}_{C2M,i} + T_{film,i}\dot{m}_{F2M,i} + T_{mix,i-1}\dot{m}_{mix,i-1}}{\dot{m}_{C2M,i} + \dot{m}_{F2M,i} + \dot{m}_{mix,i-1}} & \text{otherwise} \end{cases} \tag{90}$$

where mass flow rate in the mixing region is calculated as:

$$\dot{m}_{mix,i} = \left(\dot{m}_{g,i} + \dot{m}_{film,i}\right) \frac{A_{mix,i}}{A_{g,i} + A_{film,i} + A_{mix,i}} \tag{91}$$

Since pressure is known from the core region, mixing density can be obtained by the equation of state, and the other fluid properties are retrieved as a function of pressure and temperature. As far as chemical composition is concerned, a chemical equilibrium model is adopted for the core and the mixing flow regions. The film does not need any chemical model since only one species is considered by the model. Mixing chemical composition is calculated on the basis of the incoming mass flow rates from the core and film regions.
Eventually, mixing velocity is calculated from mass flow rate:

$$u_{mix} = K_a\, K_u \frac{\dot{m}_{mix}}{\rho_{mix}\, A_{mix}} \tag{92}$$

where $K_a = A_c/A$ and $K_u = (u_g - u_{film})/u_g$ are two correction parameters accounting for chamber area variation and jets velocity difference.

The convective heat transfer coefficient is evaluated differently for the mixing and film regions. In the mixing region ($x \geqslant x_1$) the latter is evaluated by means of a modified Stanton–type Bartz equation [138]:

$$St_{0,mix} = 0.026 \left(\frac{\mu_{mix}}{\dot{m}_{mix}}\right)^{0.2} \left(\frac{A\,\pi/4}{r_{curv}\, D_{th}}\right)^{0.1} \left(\frac{T_{aw}}{T_{mix}}\right)^{0.6} \left(\frac{x}{x_{th}}\right)^{-0.2} Pr_{mix}^{-0.6} \tag{93}$$

where r_{curv} is the radius of curvature, D_{th} and x_{th} are throat diameter and abscissa respectively, and T_{aw} is the adiabatic wall temperature. On the other hand, in the film region ($x < x_1$) the simpler modified Pavli equation is used [138]:

$$St_{0,film} = 0.026\, Re_{film}^{-0.2}\, Pr_{film}^{-0.6} \left(\frac{T_{aw}}{T_{ref}}\right)^{0.6} \left(\frac{x}{x_{th}}\right)^{-0.2} \tag{94}$$

where Re_{film} is the film slot height–based Reynolds number, Pr_{film} is the film Prandtl number, and T_{ref} is a reference temperature. Two correction factors are added to the Stanton number:

- $K_{acc} = \sqrt{1 - |r_{c,i} - r_{c,i-1}|}$, to account for flow acceleration in the convergent part of the nozzle;

- $St_{corr,i} = 0.25\,atan\left[7\left(\frac{x_i}{x_{comb}} - 0.63\right)\right] + 0.7$, to account for vaporization phenomenon near to the injector plate. The quantity x_{comb} represents the spatial extension of the region in which such phenomenon is considered, and can be enforced as a free parameter

In such a way, the effective Stanton number can be obtained as:

$$St = K_{acc}\, St_{corr}\, St_0 \tag{95}$$

and the convective heat load can be expressed as:

$$Q_{conv,i} = A_i\,(T_{aw,i} - T_{wall,i}) \begin{cases} St_{film,i}\,\rho_{film,i}\,u_{film,i}\,c_{p,film,i} & \text{if } x < x_1 \\ St_{mix,i}\,\rho_{mix,i}\,u_{mix,i}\,c_{p,mix,i} & \text{if } x \geqslant x_1 \end{cases} \tag{96}$$

3.2.2 Numerical correlation for the film cooling effectiveness

The CFD–based numerical correlation described in detail in this section may be used as a more robust alternative to calculate the potential core length with respect to the Simon–Di Matteo et al. loop procedure shown in Fig. 6.

The CFD model described in Chap. 2 has been used to carry out numerical simulations. The model has been suitably validated against experimental data [64] (see [139] for details) to assess its capability to reproduce the main elements of the phenomenology under invstigation. In this framework, it is worth noticing that the validation procedure has been carried out against experimental tests conducted with nearly ambient–temperature air on a flat plate, hence under conditions very far from those typical of liquid rocket engines. This choice is justified and supported by the remarkable simplicity of such a setup. In fact, it should be kept in mind that the combustion chamber of a rocket engine can be approximated by a flat plate over which very different operating conditions occur. In this regard, the present numerical correlation aims at providing the following improvements with respect to those developed in the past for gaseous film cooling [88–93]:

- Wider applicability range to a larger spectrum of operating conditions;
- Application under operating conditions tyipical of liquid rocket engines, characterised by high pressure and high temperature differences between the hot gas and the coolant;
- Improved accuracy in the prediction of gaseous film cooling capabilities.

The correlated quantity in this model is the adiabatic film cooling effectiveness, defined as follows:

$$\eta(x) = \frac{T_{aw}(x) - T_g}{T_{film} - T_g} \tag{97}$$

This effectiveness represents the capability of the film to thermally insulate a surface, and it is 1 when the local adiabatic wall temperature T_{aw} equals the film injection temperature T_{film}, whereas it approaches 0 as the adiabatic wall temperature approaches the hot gas temperature T_g. Typically, the film cooling effectiveness over a flat plate follows a characteristic trend in the logarithmic plane as a function of the non–dimensional abscissa x/h_{slot}, shown in Fig. 8.

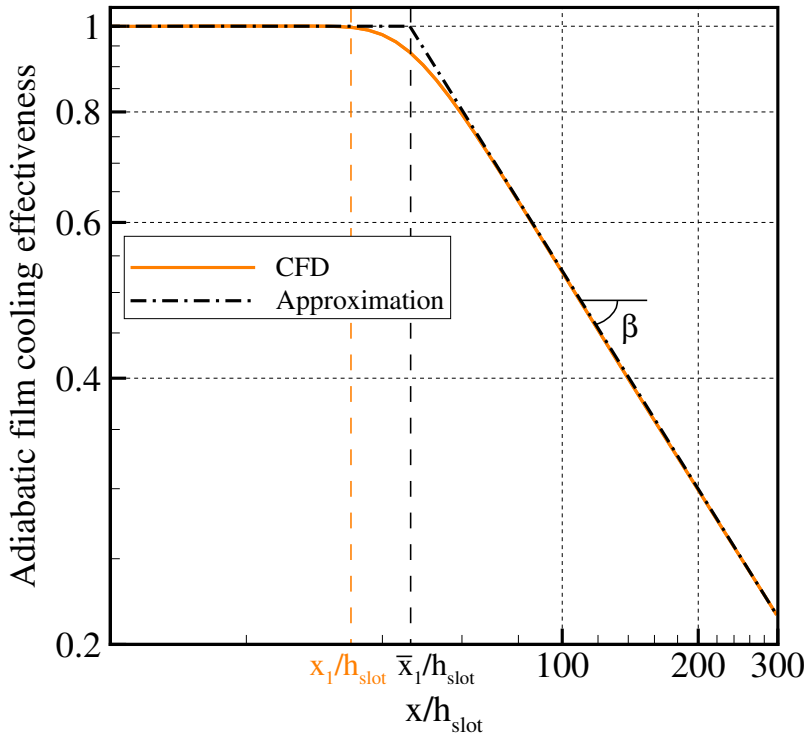

Figure 8: Typical trend forseen for the adiabatic film cooling effectiveness over a flat plate.

The effectiveness is unitary until a particular abscissa x_1/h_{slot}, which is actually the non–dimensional potential core length, and then undergoes a linear (power–law trend) decrease with a certain slope β. The final goal of this numerical correlation is the quick evaluation of the two parameters x_1 and β, which completely identify the effectiveness spatial evolution, as a function of the main parameters which characterize a gaseous film–cooled combustion chamber. The main parameters, listed below with their investigated ranges, have been chosen as the result of a CFD–based sensitivity analysis, employing as a starting point the validation flat plate setup.

- Injection slot height, $h_{slot} \in [0.75,\ 5.00]$ mm;
- Blowing ratio, $B \in [0.2,\ 2.5]$;
- Slot height–based film Reynolds number, $Re_{film} \in [2300,\ 17700]$;

- Injection of different gases. Film–mainstream gas combinations include air, methane, and hydrogen gases.

Note that parameters are varied one at a time while keeping the others at their reference values, hence retaining the superposition principle assumption. All of those contributions to the film cooling effectiveness are included in the correlation by means of different functions Φ_i, which are obtained by the interpolation of the carried–out CFD numerical results.

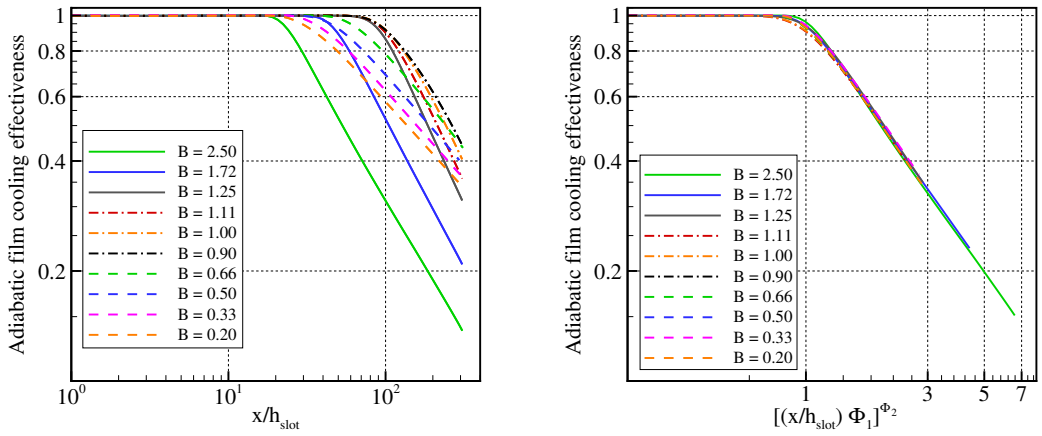

Figure 9: Film cooling effectiveness at different blowing ratios as a function of non–dimensional abscissa (left) and suitable reduction parameter (right).

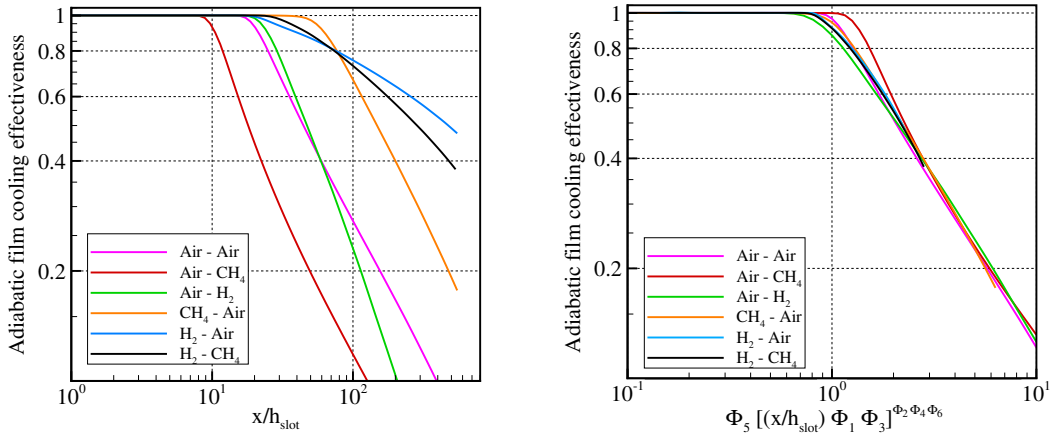

Figure 10: Film cooling effectiveness obtained with different film–mainstream gases combinations as a function of non–dimensional abscissa (left) and suitable reduction parameter (right).

Each function has the peculiarity to depend on a suitably designed parameter which collapses all the numerical results, carried out over a certain spectrum of operating conditions, as much as possible on a single curve. All the functions Φ_i are illustrated in the following, together with the numerical correlation. As examples, numerical simulations with variable blowing ratio and variable film–mainstream gases combinations are shown in Figs. 9 and Fig. 10, respectively. In particular, sub–figures (a) show results as a function of the non–dimensional abscissa x/h_{slot}, whereas sub–figures (b) show results as a function of a suitable combination of functions Φ_i. For more details about the procedure the reader is referenced to [139]. As a result, the numerical correlation has been carried out in the form:

$$\eta(x) = \begin{cases} 1 & \text{if } x \leqslant \bar{x}_1 \\ \Phi_5^{-1} \left[\left(\dfrac{x}{h_{slot}} \right) \Phi_1 \, \Phi_3 \right]^{-\Phi_2 \, \Phi_4 \, \Phi_6} & \text{otherwise} \end{cases} \tag{98}$$

where $\bar{x}_1$ is the estimation of the potential core length, as shown also in Fig. 8. The latter is expressed as

$$\frac{\bar{x}_1}{h_{slot}} = \Phi_5^{\Phi_2 \, \Phi_4 \, \Phi_6} \, [\Phi_1 \, \Phi_3]^{-1} \tag{99}$$

All the mentioned functions Φ_i are listed in the following, pointing out also the effect on the adiabatic film cooling effectiveness they account for.

- Effect of blowing ratio (B) on the potential core length estimation ($\bar{x_1}$):

$$\frac{1}{\Phi_1 \left(\frac{1}{B}\right)} = \frac{31.68 \, \left(\frac{1}{B}\right)^3 - 42.07 \, \left(\frac{1}{B}\right)^2 + 48.55 \, \left(\frac{1}{B}\right) - 7.936}{\left(\frac{1}{B}\right)^3 - 1.331 \, \left(\frac{1}{B}\right)^2 + 0.2638 \, \left(\frac{1}{B}\right) + 0.3563} \tag{100}$$

- Effect of blowing ratio on the effectiveness drop slope (β):

$$\Phi_2 \left(\frac{1}{B}\right) = \frac{27.16 \, \left(\frac{1}{B}\right)^2 - 49.73 \, \left(\frac{1}{B}\right) + 27.80}{\left(\frac{1}{B}\right)^3 + 48.83 \, \left(\frac{1}{B}\right)^2 - 86.58 \, \left(\frac{1}{B}\right) + 43.22} \tag{101}$$

- Effect of slot–based Reynolds number (Re_{film}) on the potential core length estimation:

$$\Phi_3 \left(Re_{film}\right) = \frac{0.989}{1784 \, Re_{film}^{-1.21} + 0.9509} \tag{102}$$

- Effect of slot–based Reynolds number (Re_{film}) on the effectiveness drop slope:

$$\Phi_4 \left(Re_{film}\right) = \frac{0.990}{666.3 \, Re_{film}^{-1.088} + 0.9484} \tag{103}$$

- Effect of coolant–mainstream fluid properties on the potential core length estimation:

$$\Phi_5\left(\zeta_5\right) = 0.954\,\frac{\zeta_5^3 - 10.73\,\zeta_5^2 + 23.76\,\zeta_5 - 21.4}{0.8124\,\zeta_5^3 - 11.39\,\zeta_5^2 + 23.04\,\zeta_5 - 19.65} \tag{104}$$

where:

$$\zeta_5 = \left(\frac{\rho_{film}}{\rho_g}\right)^{0.75}\left(\frac{c_{p,film}}{c_{p,g}}\right)^{0.03} \tag{105}$$

- Effect of coolant–mainstream fluid properties on the effectiveness drop slope:

$$\Phi_6\left(\zeta_6\right) = \frac{0.884}{2.28\,\zeta_6^{-0.1445} - 1.412} \tag{106}$$

where:

$$\zeta_6 = \left(\frac{\rho_{film}}{\rho_g}\right)^{0.50}\left(\frac{c_{p,film}}{c_{p,g}}\right) \tag{107}$$

The numerical correlation above has been validated against two liquid rocket engine applications, involving oxygen–methane and oxygen–hydrogen propellant combinations to assess its prediction capabilities under different conditions from those defining the validation test case.

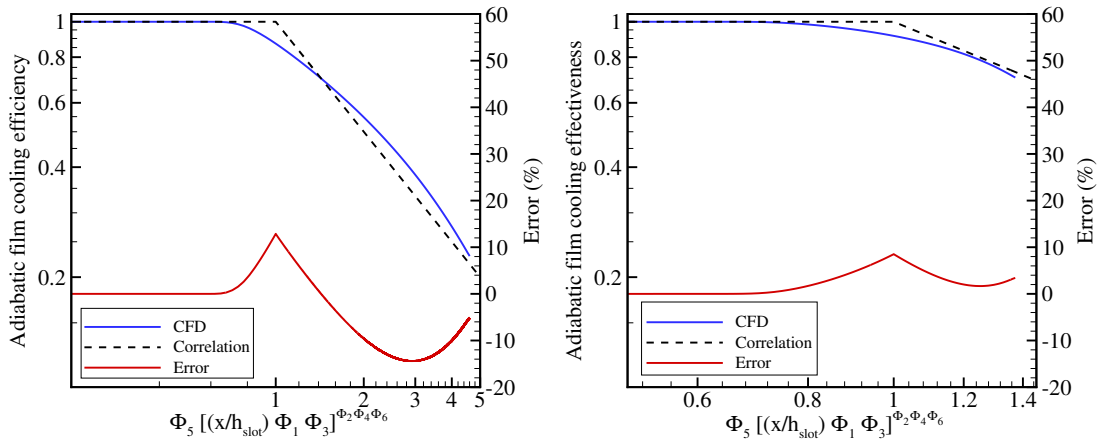

(a) oxygen–methane (b) oxygen–hydrogen

Figure 11: Comparison between results provided by the newly–developed numerical correlation and CFD simulation for oxygen–methane (left) and oxygen–hydrogen (right) combustion chambers.

The subscale combustion chambers B [101] for oxygen–methane and E [140] for oxygen–hydrogen developed at DLR Lampoldshausen have been considered. Two CFD simulations have been conducted reproducing the experiments,

and providing adiabatic film cooling effectiveness axial profiles. Numerical results are shown in Fig. 11, where they are also compared with the newly–developed numerical correlation. The percentage discrepancy between the two is represented as a solid red line. The numerical correlation presented in this section is capable to reproduce the adiabatic film cooling effectiveness within 15% error in both cases. Higher accuracy is shown in case of the oxygen–hydrogen combustion chamber, where errors do not exceed 10% along the combustion chamber. Nevertheless, higher error is provided on the potential core length evaluation.

3.3 IMPLEMENTATION

The film cooling models presented in this chapter has been implemented in the EcosimPro/ESPSS platform during this Ph.D. research. In particular the 6.2.0 version of the software and the 3.3.0 version of the ESPSS libraries have been used. In this section, the new film–cooled thrust chamber is presented, providing an overview and a detailed description of the implementation strategy. For all the clarifications concerning the EcosimPro programming language features and terminology, the interested reader is referenced to the EcosimPro/ESPSS user manual. The new film–cooled thrust chamber has been conceived as the natural extension of the previously–existing ESPSS uncooled liquid combustor component, whose main characteristics have been retained in the implementation of the reduced models. The film-cooled thrust chamber component has been implemented as a new component, and the motivation lays in the fact that it needed invasive modifications, with respect to the uncooled liquid combustor, due to the multidisciplinary nature of the problem. A further distinction is made between gaseous and liquid formulations due to the different implementation techniques required by the reduced models, eventually providing two separated components.

3.3.1 New components overview

The new film–cooled thrust chamber omponents are shown in Fig. 12. Components differ only for the combustor design, thus retaining the same topology (see Fig. 13). A new fluid connection for film injection, with a minimalist internal line, has been added to the component on the basis of the original fuel and oxidizer ones. The line includes an external fluid port (*f_cool*), i.e., coolant inlet, a coolant dome (*Cav_cool*) and a coolant injector (*Inj_cool*) which is connected to the new film–cooled combustor component, in turn. The line is modeled by means of components already available in the ESPSS library, such as cavities, junctions, thermal nodes with imposed temperature, and an analog temperature signal. As done for the two propellant lines (namely *red* and *oxy*), information about pressure, temperature and quality factor is shared between

the dome and the chamber, but the coolant cavity *Cav_cool* is modeled to be thermally independent from the rest of the engine for robustness reasons (see bottom Fig. 13).

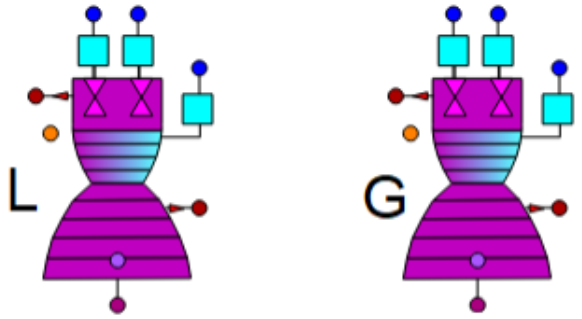

(a) (b)

Figure 12: New film–cooled thrust chamber components: *CombustChamberNozzle_LFC* (a) and *CombustChamberNozzle_GFC* (b).

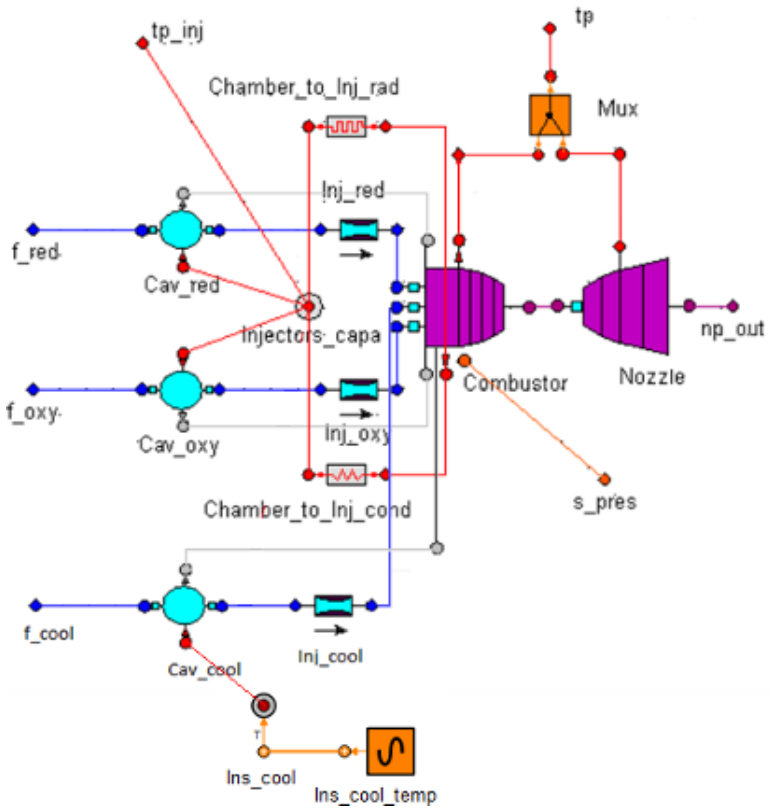

Figure 13: New film–cooled thrust chamber components: topology.

The new film–cooled combustor component is a significantly modified version of the regular liquid combustor (*abs_combustor*) component, already available in the ESPSS library. Such modifications allow to properly model film cooling in a multi–disciplinary sense. In fact, the presence of the coolant affects both the heat load to the walls and the hot gas flow behaviour inside the

chamber, influenced by coolant vaporization and reaction. The original nozzle component included in the ESPSS 3.3.0 version has been retained without modifications.

3.3.2 Implementation strategy

All the models mentioned in this chapter have been implemented into the EcosimPro/ESPSS framework within the new components *CombustChamberNozzle_LFC* and *CombustChamberNozzle_GFC*. Such components employ a modified version of the uncooled liquid combustor, which has undergone large modifications to include the film cooling models. Moreover, the new components allow to switch among the different formulations, in order to select the most suitable one depending on the specific application and the sought level of approximation.

Concerning liquid film cooling, film injection can take place arbitrarily at any chamber node, referred to as i_{fs}, with the chamber acting as the regular uncooled combustor upstream of that location. The logic behind such a procedure is described more in detail in the following, taking the Grisson liquid film cooling model as a reference. Note that terms marked as red in the equations below represent additions to the conservation equations belonging to the regular liquid ESPSS combustor. Moreover, equations are reported as already discretised according to the EcosimPro 1–D environment.

- Upstream of i_{fs}: wall conditions are calculated as in the regular combustor. Conservation equations remain unchanged:

$$V_i \frac{\partial \rho_i}{\partial t} + \Delta \dot{m}_i = \dot{m}_{vf,i} + \dot{m}_{vo,i} \tag{108}$$

$$\frac{L_i + L_{i+1}}{2} \frac{\partial \dot{m}_i}{\partial t} + \Delta \left[A \left(p + q_n + \rho u^2 + \frac{1}{4} \xi \rho u |u| \right) \right]_i = \tag{109}$$

$$= \frac{p_i + p_{i+1}}{2} \Delta A_i$$

$$V_i \frac{\partial (\rho e_0)_i}{\partial t} + \Delta (\dot{m} h_0)_i = Q_{vf,i} + Q_{vo,i} - Q_{g,i} \tag{110}$$

where $\dot{m}_{vf}$, $\dot{m}_{vo}$, Q_{vf}, and Q_{vo} are mass flow rates and heats associated to the vaporised fuel and oxidiser, q_n is the artificial viscosity, ξ is the equivalent distributed friction, function of geometry, absolute roughness, and Reynolds number, and Q_g is the heat load associated to the hot gas and sent to the thermal port;

- Downstream of i_{fs} and upstream of the complete evaporation location, marked as i_{fe} (computed at runtime): wall conditions are calculated through the selected liquid film cooling model.

$$V_i \frac{\partial \rho_i}{\partial t} + \Delta \dot{m}_i = \dot{m}_{vf,i} + \dot{m}_{vo,i} + \dot{m}_{vc,i} + \dot{m}_{c,gas} \tag{111}$$

$$\frac{L_i + L_{i+1}}{2} \frac{\partial \dot{m}_i}{\partial t} + \Delta \left[A \left(p + q_n + \rho u^2 + \frac{1}{4} \xi \rho u |u| \right) \right]_i = \tag{112}$$

$$= \frac{p_i + p_{i+1}}{2} \Delta A_i + \left(\dot{m}_{vc,i} + \dot{m}_{c,gas} \right) u_i$$

$$V_i \frac{\partial \left(\rho e_0 \right)_i}{\partial t} + \Delta \left(\dot{m} h_0 \right)_i = Q_{vf,i} + Q_{vo,i} + Q_{vc,i} + \tag{113}$$

$$+ \left(\dot{m} h_0 \right)_{c,gas} - Q_{loss}$$

where $\dot{m}_{vc}$ and Q_{vc} are the vaporized coolant mass flow rate and heat, and $\dot{m}_{c,gas}$ is the gaseous phase fraction of the injected coolant mass flow rate;

- Downstream of i_{fe}: wall conditions are calculated through the gaseous film cooling formulation embedded in the liquid model.

$$V_i \frac{\partial \rho_i}{\partial t} + \Delta \dot{m}_i = \dot{m}_{vf,i} + \dot{m}_{vo,i} + \dot{m}_{vc,i} \tag{114}$$

$$\frac{L_i + L_{i+1}}{2} \frac{\partial \dot{m}_i}{\partial t} + \Delta \left[A \left(p + q_n + \rho u^2 + \frac{1}{4} \xi \rho u |u| \right) \right]_i = \tag{115}$$

$$= \frac{p_i + p_{i+1}}{2} \Delta A_i + \dot{m}_{vc,i} u_i$$

$$V_i \frac{\partial \left(\rho e_0 \right)_i}{\partial t} + \Delta \left(\dot{m} h_0 \right)_i = Q_{vf,i} + Q_{vo,i} + Q_{vc,i} - Q_{loss} \tag{116}$$

The quantity Q_{loss} represents the heat exchanged between the hot gases and the liquid film, and is calculated differently depending on the coolant phase:

$$Q_{loss} = \begin{cases} A_i \left(q_{rad,wall,i} + q_{rad,film,i} + q_{conv,filmIN,i} \right) & \text{if } i_{fs} \leqslant i \leqslant i_{fe} \\ A_i \left(q_{conv,wall,i} + q_{rad,wall,i} \right) & \text{otherwise} \end{cases} \tag{117}$$

As far as the location between the coolant injection node and the complete evaporation node is concerned, heat losses include the radiative heat flux both to the film and to the wall and the convective heat released by the hot gas and absorbed by the liquid film ($q_{conv,filmIN}$). On the other hand, when the coolant is totally evaporated convection and radiation to the wall are considered.
Depending on the film cooling model, both convective and radiative heat load formulations, as well as the definition of the hot–gas emittance, are suitably modelled.

No restrictions apply concerning the coolant species choice, as it can be chosen as one of the propellants or a third different fluid. In this regard, propellant species mass conservation laws are influenced by the nature of the coolant. As an example, if the coolant chemical coincides with the fuel one, the following equations apply:

$$\begin{cases} V_i \dfrac{\partial (y_f \rho)_i}{\partial t} + \Delta \dot{m}_{f,i} = \dot{m}_{vf,i} + \dot{m}_{vc,i} + \dot{m}_{c,gas,i} & \text{if } i = i_{fs} \\ V_i \dfrac{\partial (y_f \rho)_i}{\partial t} + \Delta \dot{m}_{f,i} = \dot{m}_{vf,i} + \dot{m}_{vc,i} & \text{otherwise} \end{cases} \tag{118}$$

where y_f is the fuel mass fraction. On the other hand, if a third fluid is chosen as the coolant, a further variable y_{co} is considered with its dedicated conservation equation, similarly to Eq. (118). Coolant mixtures are also allowed by the newly–developed chamber component. In this framework the implementation has been slightly changed by introducing a n–species modelling:

$$\begin{cases} V_i \dfrac{\partial (\rho\, y_j)_i}{\partial t} + \Delta \left(\dot{m}\, y_j\right) = & \text{if } i = i_{fs} \\ = \dot{m}_{vf,i}\, y_{f,j} + \dot{m}_{vo,i}\, y_{o,j} + \dot{m}_{b,i} \left(y_{i,j} - y_{eq,i,j}\right) + \left(\dot{m}_{vc,i} + \dot{m}_{c,gas,i}\right) y_{c,j} & \\ V_i \dfrac{\partial (\rho\, y_j)_i}{\partial t} + \Delta \left(\dot{m}\, y_j\right) = & \text{otherwise} \\ = \dot{m}_{vf,i}\, y_{f,j} + \dot{m}_{vo,i}\, y_{o,j} + \dot{m}_{b,i} \left(y_{i,j} - y_{eq,i,j}\right) + \dot{m}_{vc,i}\, y_{c,j} & \end{cases} \tag{119}$$

where $j = 1, \ldots, N_s$, N_s is the number of species included in the EcosimPro chemical database, y_j is the mass fraction of the j–th species in the mixture, $\dot{m}_b$ is the combustion products mass flow rate (suitably calculated if the model is active), y_{eq} is the combustion products equilibrium composition, and y_o and y_c are the oxidiser and coolant mass compositions, respectively.

After the passage in its dome (*Cav_cool*) and injector (*Inj_cool*), the film is injected at the desired position inside the combustion chamber through the dedicated fluid port. In the same way as fuel and oxidizer, some quantities are passed to the chamber by the cavity and the port, like coolant mass flow rate, dome pressure, temperature, and quality factor. To avoid coolant heating prior to injection, the dome temperature is taken as the coolant injection temperature, which is automatically enforced through the *Ins_cool* and *Ins_cool_temp* components (see topology in Fig. 13). In particular, an axisymmetric circumferential

slot is assumed for the coolant injection geometry, whose height is calculated as follows:

$$h_{slot} = \frac{1}{2}\left(D_{c,i_{fs}} - \sqrt{D^2_{c,i_{fs}} - 4\,A_{cool}/\pi}\right) \tag{120}$$

where $D_{c,i_{fs}}$ is the chamber diameter at node i_{fs} and the area A_{cool} is supposed to be known. The injection area is then assigned to the coolant fluid port and also to the junction *Ins_cool*. Coolant mass flow rate is split into liquid and gaseous fractions through the dome quality factor, as done for the propellants. In case of liquid film cooling model, if the dome temperature is such to produce a quality factor between 0 and 1, only the liquid fraction of the mass flow rate is considered as available for film cooling, and the rest is immediately mixed with the hot gases at the first chamber node (see $\dot{m}_{c,gas}$ in Eqs. 111, 112, and 113). The liquid mass flow rate is not supposed to contribute to the liquid mass and energy conservation equations since it is considered as of secondary importance. The hot gases and the coolant are considered as two separate entities, until evaporation occurs. Note that the evaporation dynamics occurring between the liquid film and the hot flow depends on the specific liquid film cooling model. Such dynamics has been included in all the flow conservation laws as a distributed mass flow rate source term $\dot{m}_{vc}$ along the chamber, and thus correctly generates different phenomena, as follows:

- Chamber pressure increases due to the injected additional mass flow rate;
- The enthalpy content of the inflowing flow influences chamber temperature;
- Coolant chemicals react with the hot gases, influencing the hot mixture composition (O/F shift) and thus its temperature;
- Heat loss term in the energy equation also includes the heat transferred from the hot gas to the film.

It has to be remarked that the coolant evaporation process and the thermochemical state of the hot gas stream in its vicinity are interdependent. For such a reason, an iterative procedure is necessary to compute the correct coupling between heat load to the film and the hot stream state in its vicinity. Specifically, the sub–stepping consists in:

- Firstly, as in the original component, an initial chemical composition (unburned propellants only) is defined. Propellants are then mixed together, eventually providing a mixture at the desired O/F;
- Then, the evaporated coolant is added to this mixture. The amount of vaporized coolant is determined by the film cooling models during the iterative procedure;
- After that, the mixture containing the mixed hot gas and coolant is burned, providing the final thermodynamic state, fluid properties and mixture composition.

- Finally, the burned mixture is used to compute the new evaporation rate through the film cooling models.

Due to such interdependence, the system would end up in a quite heavy differential–algebraic equations system. To avoid such a thing an additional ODE has been introduced to break this nonlinearity. Therefore, the evaporation dynamics $\dot{m}_{vc,i}$ has been modeled to follow the law:

$$\frac{\partial \dot{m}_{vc,i}}{\partial t} = c_\alpha \left(-\dot{m}_{vc,i} + \dot{m}_{vc,ist,i}\right) \tag{121}$$

where $\dot{m}_{vc,ist}$ is the instantaneous coolant vaporized mass flow rate value provided from the film cooling models and c_α is a suitably tuned calibration parameter.

Concerning gaseous film cooling the logic remains the same until the integration of the governing equations (see Sec. 3.2.1), except for the evaporation process, which is not present of course. Hot gases, film, and mixing regions are treated independently in the combustor, and then assembled together depending on the computed flowfield geometry (see Fig. 5) to eventually provide the wall heat load distribution.

Part II

RESULTS

4 UNCOOLED THRUST CHAMBER

This chapter aims at analyzing the impact of the detailed flow and chemical reactions evolution occurring in the cylindrical part of the thrust chamber on the heat flux at nozzle throat, in the framework of uncooled liquid rocket engines. For this purpose, two sets of simulations have been identified sharing the same code, kinetic mechanism, and wall resolution. The two CFD modeling strategies are discussed and compared with each other to identify what is the main physics influencing the evaluation of throat heat flux. The first strategy assumes as inlet conditions those that should identify the streamtube zone (see Fig. 1): it therefore neglects the details of combustion and mixing processes, allowing to get a quick evaluation of the heat flux at the throat and, more generally, in the divergent part of the nozzle. This can be considered a valid assumption in well–designed full–scale engines, which are characterized by high combustion efficiency. Obviously, this approach does not allow to obtain a reliable evaluation of the wall heat flux at the foremost part of the combustion chamber. To provide a more realistic numerical representation of the real flow physics, the second approach considers a more detailed, yet simplified, modeling of the injection and combustion of oxygen and methane. This has the aim of at least partially taking into account, with a reasonable computational time, the phenomena neglected within the first strategy. Results obtained with both approaches are compared with each other, with numerical simulations from the literature and with experimental data [17], suitably described at the beginning of this chapter. The analysis is finally extended to a wide range of chamber pressures, yielding a Bartz-like numerical correlation for a quick evaluation of the wall heat flux for oxygen/methane liquid rocket engines.

4.1 TEST CASE

The selected test case for the present study is the seven-element thrust chamber described in Ref. [15] burning gaseous oxygen and gaseous methane. The thrust chamber is composed of five water–cooled segments. According to Ref. [15], together with the nozzle segment, the total length of the thrust chamber is 383 mm. The combustion chamber inner diameter is 30 mm and the throat diameter is 19 mm, resulting in a relatively small contraction ratio of 2.5. The reference operating mean chamber pressure is 18.3 bar, the mixture ratio is 2.65, and the total mass flow rate is 0.291 kg/s. Reported measurements of wall pressure refer to 13 pressure transducers placed all along the combustion cham-

ber. Information about wall temperature and heat flux were made available in Ref. [15] both in the combustion chamber and in the nozzle by thermocouples and calorimetric measures in different cooling segments surrounding the thrust chamber. The cooling segment for the nozzle provides a single measurement of the average heat flux, which is the most relevant experimental information for the present research. Injection of propellants is achieved through a faceplate with seven distinct injectors, six peripheral and one in the center (see Fig. 14a).

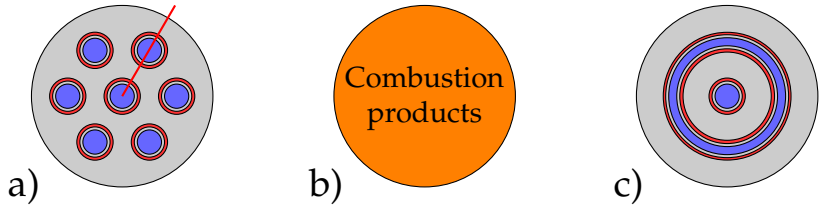

Figure 14: Injection plate schematics: real injection plate (a), CPI simulations (b), API simulations (c). Proportions are realistic. Orange, red, and blue areas stand, respectively, for combustion products, gaseous methane, and gaseous oxygen injection, whereas grey areas represent walls.

4.2 NEAR–INJECTOR APPROACH

The arrangement of the injectors leads to a complex 3–D flow characterized by strong interactions among the individual flames. Large temperature variations are expected to occur in the azimuthal direction due to the interaction of the contiguous jets, thus affecting the convective heat flux coefficient. Although these 3–D phenomena are present in the combustion chamber, this research is mainly focused on the heat load at the throat, where the above–mentioned processes might be considered negligible. To assess the validity of this conjecture, two different approaches with increasing model completeness are employed in this study. The simplest one will be referred to as *combustion product injection* (CPI; see Fig. 14b). This approach is characterized by a uniform injection of combustion products through the whole injection plate area; hence the details of the mixing and combustion processes are completely bypassed. The imposed chemical composition is the equilibrium composition obtained with specified mixture ratio and chamber pressure as computed with the chemical equilibrium with applications (CEA) software [113]. To evaluate the role of combustion on the throat heat flux, instead of reproducing numerically the real flow physics that would require a full 3–D numerical simulation with much higher computational effort, an equivalent injector system is considered where mixing and combustion are partially reproduced within affordable computational times. With this approach, referred to as *axisymmetric propellant injection* (API;

see Fig. 14c), the central injector is kept unchanged, whereas the six peripheral injectors are replaced with an equivalent annular injector to retain axial symmetry. The peripheral pattern is modified by tailoring the concentric rings to match the experimental injection areas.

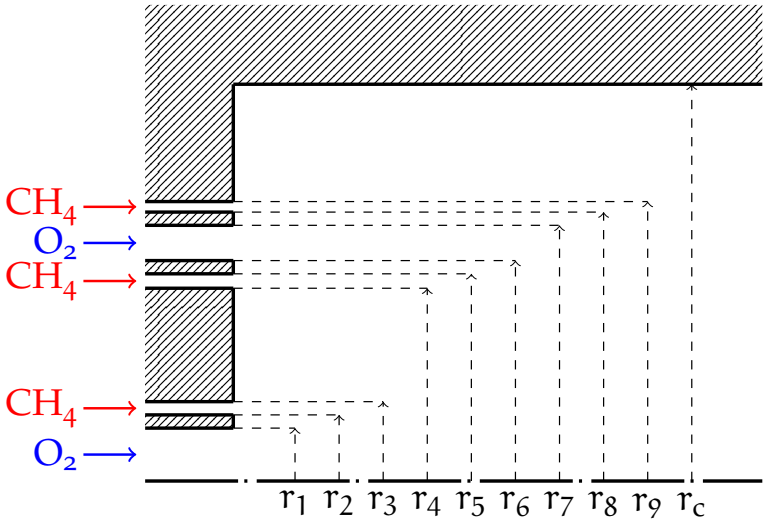

Figure 15: Injection zone schematics and radii representation for API simulations.

The mean radius of the outer oxidizer annulus is equal to the radius of the circumference passing through the outer experimental injector centers. The experimental mass flow rate is preserved, so the two outer fuel annuli receive three–sevenths of the fuel mass flow rate each, whereas the oxidizer annulus in between receives six–sevenths of the oxidizer mass flow rate. The remaining mass flow rate enters the chamber through the central injector. Since the injection areas are the same as the experimental ones, the outer fuel annulus results thinner than the inner one. The equivalent injector geometry is shown in Fig. 15, and dimensions are listed in Table. 4, where experimental radii are reported along the red line depicted in Fig. 14a.

Table 4: Injector radii of experimental faceplate and equivalent injector pattern used in the API approach. Lengths are in millimeters.

	r_1	r_2	r_3	r_4	r_5	r_6	r_7	r_8	r_9	r_c
EXP	2.00	2.50	3.00	6.00	6.50	7.00	11.00	11.50	12.00	15.00
API	2.00	2.50	3.00	7.29	7.83	8.33	9.66	10.16	10.56	15.00

Since mass flow rates and areas are preserved, injector radii are obviously different from the 3–D configuration, yielding different shear layers and propellant mixing. While this assumption may be of importance in the near–injector zone, it is expected to play only a secondary role on the investigation of throat heat transfer performed in this study, as it will be clearer in the following.

4.3 COMPUTATIONAL GRIDS AND BOUNDARY CONDITIONS

The computational domain is a single–block 2–D axisymmetric structured grid for both CPI and API approaches.

4.3.1 CPI approach

The hypothesis of homogeneous injection of combustion products allows the CPI grid to be topologically simple, as shown in Fig. 16.

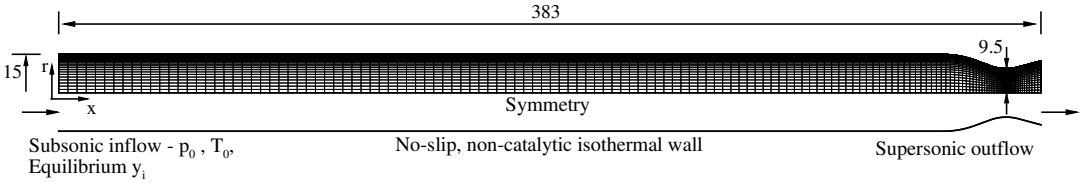

Figure 16: Computational grid with boundary conditions used for CPI simulations. Dimensions are in mm.

An overall amount of 9600 computational volumes is adopted. A cell clustering toward the upper wall is used in order to properly resolve the viscous sublayer, resulting in a non–dimensional wall distance $y^+ \approx 1$. In the axial direction, cells are clustered toward the throat to manage the higher axial gradients and the sonic conditions. Symmetry is enforced at the centerline. The upper wall is characterized by a no–slip, non–catalytic, and isothermal boundary condition. A variable temperature profile is enforced on the upper wall as shown in Fig. 17 on the basis of experimental thermocouple readings, which are only available between 6 and 320 mm [17]. Wall temperature values are obtained by piecewise–cubic–polynomials interpolation of experimental data. The latter have been used as boundary conditions in several numerical simulations performed in the literature for the same test case [25]. Moreover, it should be noted that thermocouples are placed at a depth of 0.7 and 1 mm within the copper structure of the combustion chamber, hence measuring a temperature lower than that actually present on the surface and leading eventually to a source of error in the calculation of the wall heat flux. Nevertheless, considering worst–case conditions with a wall thickness of 1 mm, a copper thermal conductivity of 390 W/(m·K), and the maximum experimental heat flux that occurs in the cylindrical part of the combustion chamber (6.72 MW/m^2), the wall temperature increase due to conduction across the chamber wall is equal to 17 K. This temperature difference results in a wall heat flux reduction of less than 0.5 %, which has been considered reasonably negligible. Since wall temperature was not measured in the nozzle, the most downstream temperature reading from the cylindrical part of the chamber is enforced to the whole

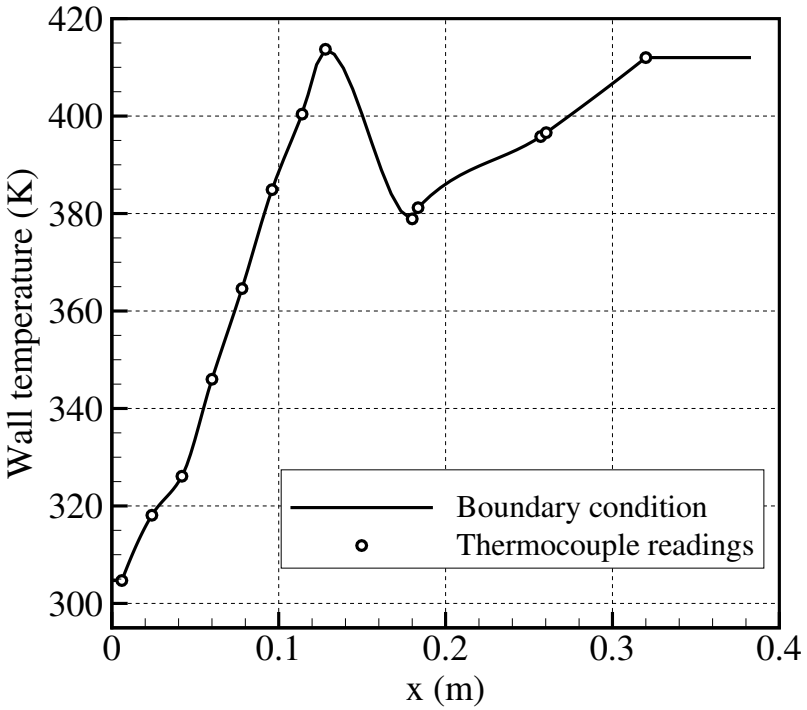

Figure 17: Experimental wall temperature readings [17] and boundary conditions enforced on the chamber upper wall.

nozzle wall. The same applies to the left boundary of the measurement range. Imposing the experimental wall temperature as a numerical boundary condition allows to perform a reasonable comparison between the computed wall heat flux and the integral values of heat flux measured in each segment. A subsonic inflow condition is enforced to the left boundary assigning total pressure, total temperature, and chemical composition in terms of the species included in the chemical mechanism described in Sec. 2.1. The CEA program [113] is used to compute T_0 and the equilibrium mass fractions y_i at the assigned chamber pressure and mixture ratio assuming gaseous reactants at their injection temperature (see Table. 5). The reference case is at $\dot{m}$ =0.291 kg/s and O/F =2.65 [17]. Accordingly, the enforced total pressure value to match this mass flow rate results to be p_c =18.3 bar. Interestingly, this total pressure value coincides with the one reported as the mean combustion pressure in Ref [17]. The outflow is supersonic.

4.3.2 API approach

The grid used for the API approach is topologically different from the one employed in CPI simulations only in the injection region (see Fig. 15). The interaction between the jets emanating from the injectors, in fact, generates three distinct mixing layers, which are resolved by a suitable radial and axial cell

Table 5: Oxygen/methane equilibrium temperature and chemical composition computed by CEA at O/F = 2.65 for different pressures.

	p = 18.3 bar	p = 30 bar	p = 50 bar	p = 100 bar
T_0 (K)	3266.6	3314.8	3362.4	3422.4
y_{O_2}	0.0048	0.0039	0.0031	0.0022
y_{CH_4}	0	0	0	0
y_{H_2O}	0.4024	0.4063	0.4103	0.4154
y_{CO}	0.3733	0.3730	0.3727	0.3723
y_{CO_2}	0.1650	0.1655	0.1660	0.1667
y_{H_2}	0.0202	0.0202	0.0201	0.0200
y_H	0.0018	0.0016	0.0014	0.0011
y_O	0.0028	0.0022	0.0018	0.0012
y_{OH}	0.0296	0.0272	0.0246	0.0211

clustering near the injector, fading slowly away downstream. Cell clustering toward the upper wall, as done for the CPI approach, keeps y^+ of order one throughout the whole thrust chamber. To make computations affordable, a total number of 16800 cells are employed (100 in the axial and 168 in the radial direction). The grid is designed to properly and reasonably capture the developing flames, and smooth transitions between mesh regions are guaranteed by a suitable axial cell clustering, which allows to consider larger cells where the propellants are mixed and hence to reduce computational time. Boundary conditions imposed in the API approach are the same as the CPI ones, except for the inlet. Adiabatic walls and propellant subsonic inflow conditions are applied to the left boundary. Mass flow rate, static temperature, and mixture mass composition are prescribed at the inlet boundaries. Injection temperatures are taken as those in oxygen and methane manifolds upstream of injectors, equal, respectively, to 259.4 and 237.6 K.

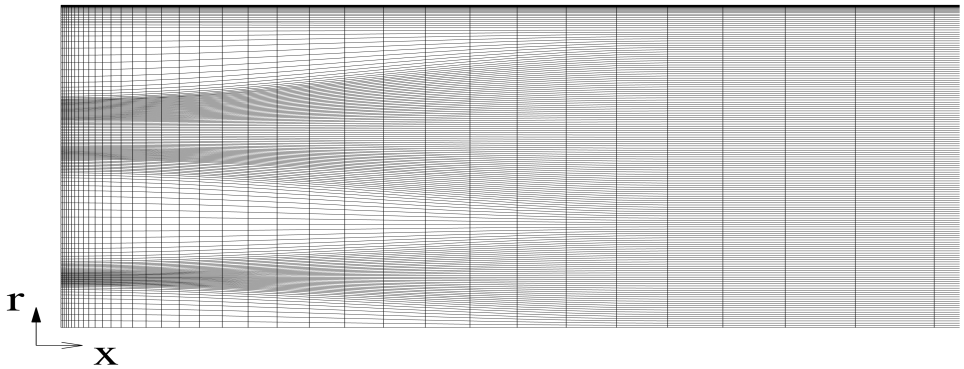

Figure 18: Enlargement of the injection region of the computational domain used for API simulations. The boundary conditions imposed on the left hand side are depicted by Figures 14c and 15.

4.4 GRID CONVERGENCE ANALYSIS

In order to verify grid independence and evaluate the numerical error, three levels of grid refinement are considered for the CPI approach. The finest level is made of 320 cells in the axial direction and 120 cells in the radial direction. Medium and coarse grids are obtained by halving and double-halving respectively the number of cells in both axial and radial directions with respect to the 320×120 grid, therefore the characteristic spatial discretization Δx is doubled by coarsening the grid. As a result, the medium grid level is composed by 160×60 cells and the coarse level by 80×30 cells. All three grid levels ensure a cell height at nozzle throat wall lower than 1 µm. Appropriate resolution of the boundary layer physics is guaranteed by the maximum dimensionless wall distance, y^+, obtained at nozzle throat wall, which ranges between 1.1 and 0.2 for the above-mentioned grid levels. As shown in Fig. 19a, the convective wall heat flux at throat obtained with the coarse and medium grid levels differs from the value obtained with the fine grid of 0.36 MW/m^2 (2.1%) and 0.08 MW/m^2 (0.46%), respectively.

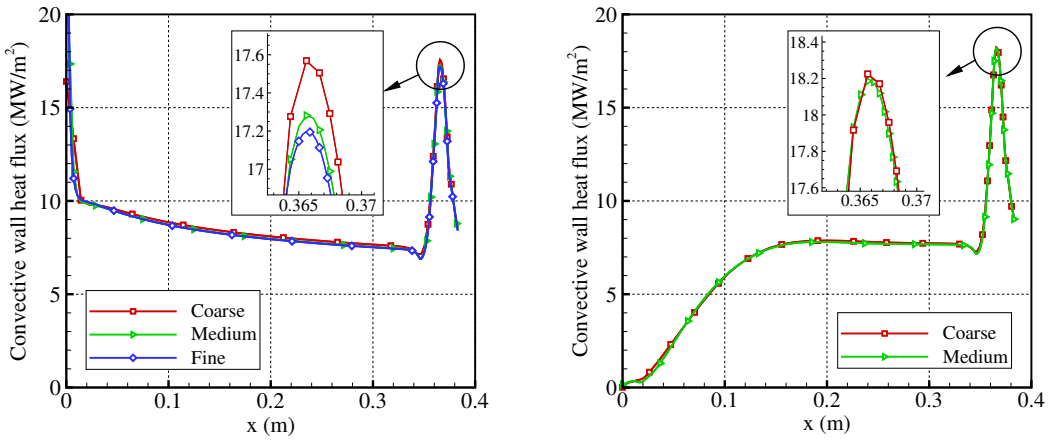

(a) CPI approach

(b) API approach

Figure 19: Grid convergence analysis on convective wall heat flux for the reference CPI and API cases.

On the basis of the numerical results shown in Fig. 19a and Table 6 it is possible to compute the order of convergence n and the Richardson-extrapolated solution [141, 142] as

$$n = \frac{1}{\ln(m)} \ln\left(\frac{f_2 - f_1}{f_3 - f_2}\right) \tag{122}$$

and

$$f_{RE} = \frac{f_2^2 - f_1 f_3}{2f_2 - f_3 - f_1} \tag{123}$$

where subscripts from 1 to 3 indicate increasing resolution from coarse to fine grid, and $\Delta x_1 = m\Delta x_2 = m^2 \Delta x_3$. By choosing f as the value of the convective

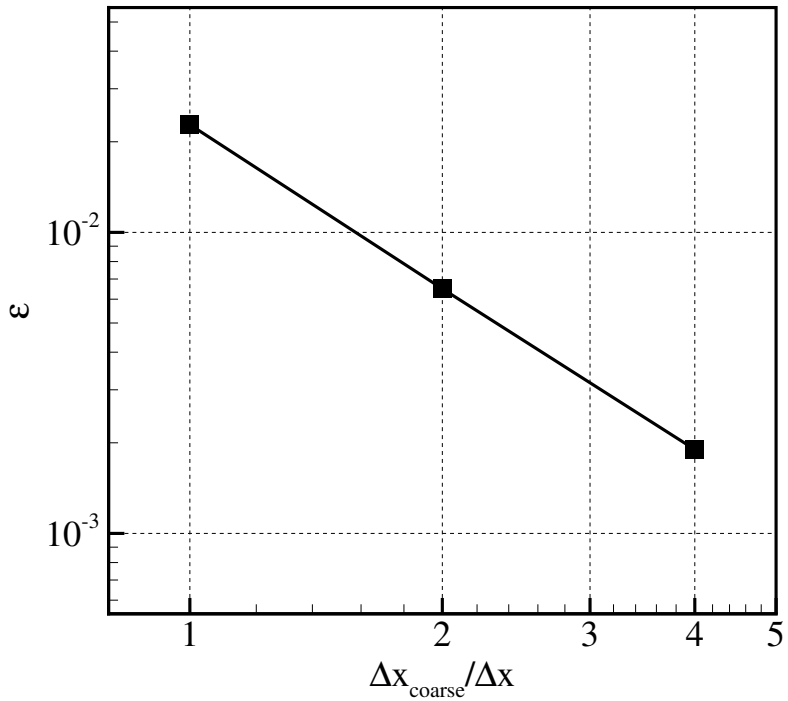

Figure 20: Numerical error for CPI convective wall heat flux results.

wall heat flux at throat, the computed order of convergence for CPI simulations is 1.8 and the error with respect to the Richardson-extrapolated solution

$$\varepsilon = |f - f_{RE}|/f_{RE} \tag{124}$$

decreases with increasing grid resolution (see Fig. 20). CPI simulations reach low errors at fine and medium grid levels, equal to 0.65 % and 0.2 % respectively. On the basis of the grid sensitivity analysis shown above, the 160×60 mesh (grid 2 in Table 6) is considered acceptable to carry out CPI simulations.

Table 6: Computational grids and convective wall heat flux values at throat used in the grid convergence analysis for CPI and API simulations.

	CPI			API		
Quantity	Grid 1	Grid 2	Grid 3	Grid 1	Grid 2	Grid 3
Number of cells	2400	9600	38400	16800	67200	–
Throat heat flux, MW/m^2	17.56	17.28	17.20	18.22	18.18	–

Once grid convergence of the solver is verified on the CPI approach, only two grid levels are considered for the API approach due to its higher computational cost. The obtained values of convective wall heat flux at throat are compared in Fig. 19b and Table 6. The coarser grid, shown partially in Fig. 18, is made by 100 cells in the axial direction and 168 cells in the radial direction. The finer grid is obtained by doubling the number of cells in each direction,

eventually providing a 200×336 grid. Both grid levels guarantee a cell height at the nozzle throat wall lower than 1 µm and a maximum dimensionless wall distance at the same position lower than 1.6. As one can notice from Fig. 19b and Table 6, the variation of convective wall heat flux at throat between the two grid levels is very small if compared to the finer solution (< 1 %). Therefore, the 100×168 grid is adopted to perform API simulations.

4.5 CPI AND API WALL HEAT FLUX COMPARISON

Despite the large differences in the assumptions made for the CPI and API approaches, their wall heat flux profiles in the nozzle are found to be in acceptable agreement (Fig. 21).

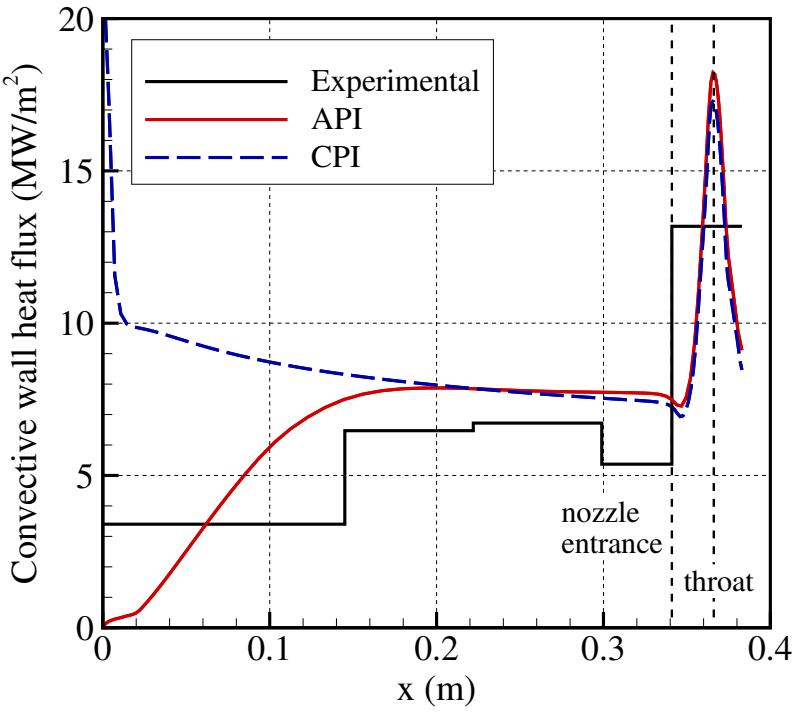

Figure 21: Convective wall heat flux results for API and CPI simulations. Experimental data are also reported [17].

In the CPI solution, where the mixture is directly injected at the adiabatic flame temperature, the heat flux decreases due to the thickening of the boundary layer until the end of the combustion chamber, and then it sharply increases reaching a peak of 17.28 MW/m^2. The inclusion of finite-rate chemistry in the numerical modeling is important in such evaluation of the peak heat flux [116, 143, 144], which has shown deviations up to 16% assuming frozen or shifting equilibrium chemistry [116]. Moreover, the effects of molecular diffusion are

not expected to be relevant for the present test case. Indeed, CPI simulations with laminar and turbulent Schmidt numbers varied in the range 0.5 – 1.0 show deviations on peak heat flux of 0.005% and 1.5%, respectively.

On the other hand, the API solution shows a steep heat flux increase within the first half of the chamber due to propellants injection and combustion. A change of slope is present at $x \approx 200$ mm indicating the end of the combustion process. A peak heat flux of 18.22 MW/m^2, which is 5.4% higher than the value computed with the CPI approach, is reached at throat. Reasons for this difference will be discussed more in detail in Section 4.8.

4.6 EXPERIMENTAL REBUILDING

To quantitatively compare the computed wall heat flux with the experimental data, it is necessary to average the local numerical values on the area of each chamber segment (see Sec 4.1).

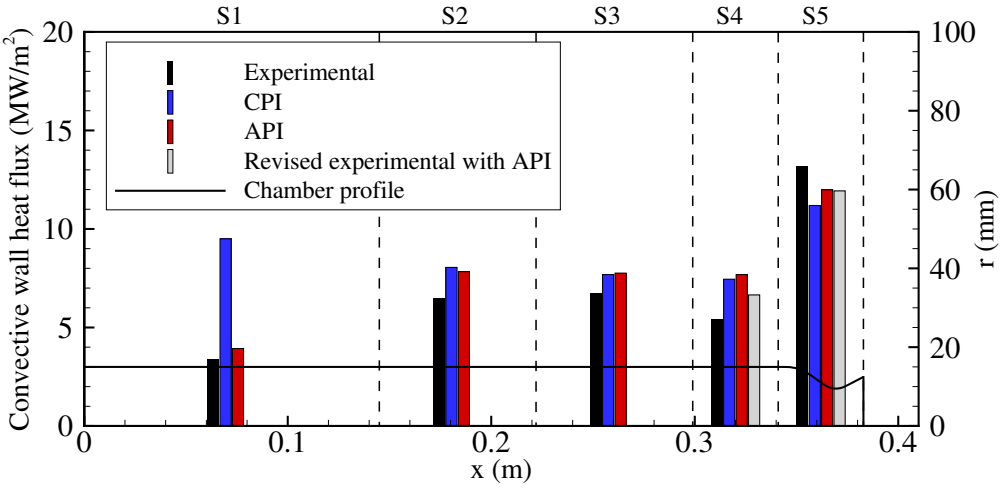

Figure 22: Numerical and experimental [17] area–averaged convective wall heat fluxes at each segment. Both original and revised experimental data are shown. Chamber segments (S1 – S5) are also indicated on the top.

The experimental wall heat flux increases in the first two segments (Fig. 22) and it is qualitatively reproduced using the API approach, while it is significantly overestimated by the CPI solution. Given the approximations in the modeling of the injection and rapid combustion region, an accurate quantitative comparison is not expected in the first two segments for neither of the considered approaches, however it is worth noting that the API solution tends to reasonably approximate the experimental results. From the second to the third segment, the experimental wall heat flux does not change significantly, indicating the end of the main combustion and mixing processes, which is consistent to what already observed with the API approach. In fact, the CPI

solution shows the best agreement with the experimental wall heat flux at the third segment. The reported experimental wall heat flux in the fourth segment is much lower than that in the third segment. Moreover, the experimental wall heat flux rises significantly from the fourth to the fifth segment. Nevertheless, it is to be considered that the thrust chamber is cooled by two water cycles, one for the first four segments (S1 – S4) and one for the nozzle segment (S5). In fact, it has been pointed out in previous studies [17, 24] that, since the inlet coolant temperature of the second water cycle is lower than the outlet coolant temperature of the first one, an axial heat transfer is present between the S4 and S5 segments. It is hence evident that the coolant flowing in the second water cycle surrounding the S5 segment is heated not only from the hot-gas side, but also from the hotter coolant of the first water cycle. In this framework, the experimental data can be revised on the basis of the trends of numerical solutions to counteract the axial energy exchange between S4 and S5, and to consider only the heat transferred from the hot gases (gray bars in Fig. 22). Accordingly, the experimental data (black bars in Fig. 22) are supposed to follow the percentage variation of API numerical results between S3 and S4, which is evaluated as 1%.

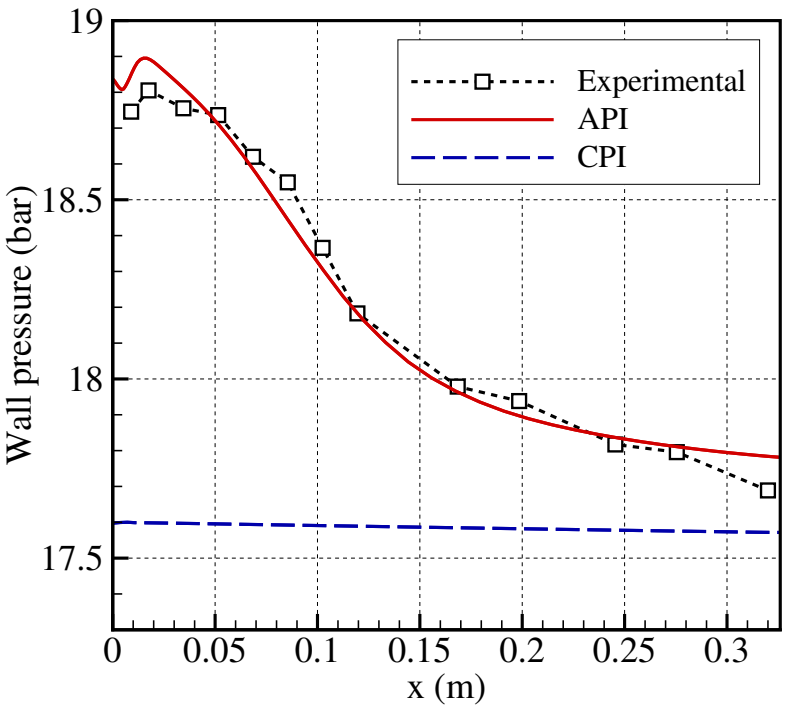

Figure 23: Numerical and experimental [17] wall pressure along the combustion chamber.

Hence, the revised value of the experimental average heat flux in S4 is obtained by lowering the experimental heat flux in S3 by the same amount, reaching a value of 6.65 MW/m^2 (grey bar in S4, Fig. 22) instead of the original one of

5.39 MW/m^2, thus showing a discrepancy of 11.26 MW/m^2. Being the revised value higher than the original one in S4, a certain amount of heat has to be provided by the fifth segment because of energy conservation. Such amount of heat, in particular equal to 4.97 kW, is obtained by multiplying the above–mentioned heat flux difference of 1.26 MW/m^2 and the wall surface of S5. Due to the same reasoning, the heat content in the fifth segment decreases by the same amount. As a result, the revised value in the nozzle is equal to 11.93 MW/m^2 (grey bar in S5, Fig. 22). The agreement between numerical and experimental heat fluxes in the nozzle segment S5, while already satisfactory if considering the original measurements (-15% and -8% for CPI and API, respectively), is improved by considering the revised experimental data (-6% and +0.5%). As far as the experimental pressure is concerned, measurements show an initial peak due to the presence of a recirculation zone close to the injection plate, and then a monotonic decrease because of heat release and flow acceleration. A satisfactory comparison between numerical and experimental wall pressure is achieved if considering the API results (Fig. 23). On the other hand, the CPI wall pressure shows a slight decrease only due to friction (because of the lack of combustion modeling) and reaches a value close to the experimental one at the nozzle entrance.

4.7 COMPARISON WITH THE LITERATURE

To better appreciate the representativeness of API simulations as a benchmark for the evaluation of the CPI approach for the purpose of evaluating throat heat flux, both API and CPI results are compared with the fully 3–D simulations performed in the literature for the present test case. Several studies in the literature have been gathered by Perakis et al. [25]. Table 7 briefly summarizes the features of the computational approaches used by the different research groups, including computational domain details, combustion and turbulence-chemistry interaction (TCI) modeling, and the number of species (s) and reactions (r) involved in the employed chemical mechanism. As far as the JL–R reaction mechanism is concerned (see Tab. 1), only 8 species and 5 reactions are needed in the CPI approach because of the injection of combustion products. Indeed, the first two reactions in Table 1 are neglected, and methane is not present among the species (see also Table 5).

Notice also that all the literature models present in Table 7 consider the experimental 7–element injector plate, hence including near–injector 3–D effects and a more comprehensive treatment of mixing and combustion than the present API and CPI approaches. This leads to computational meshes with an order of magnitude of millions of cells. On the other hand, the CPI and API approaches are based on 2–D axisymmetric computations, which allow reducing the number of grid cells by about two orders of magnitude, leading to a significant reduction of the computational burden. Average wall heat fluxes

Table 7: Features of different computational approaches used in the literature to reproduce the selected test case [25].

	CPI	API	TUM	ArianeGroup	HIT	JAXA	DLR
Domain	2–D	2–D	3–D	3–D	3–D	3–D	3–D
Grid cells	$9.6 \cdot 10^3$	$1.68 \cdot 10^4$	$2.9 \cdot 10^6$	$2.7 \cdot 10^6$	$1.3 \cdot 10^6$	$4.7 \cdot 10^6$	$1.4 \cdot 10^6$
Combustion	CEA	Finite rate	Flamelet	Flamelet	EDC	Finite rate	Flamelet
TCI	Laminar	Laminar	β-PDF	β-PDF	EDC	Laminar	β-PDF
Chemistry	8s – 5r	9s – 7r	21s – 97r	35s – 217r	14s – 18r	21s – 97r	35s – 217r

EDC stands for eddy dissipation concept, and PDF for probability density function.

provided by the different models are shown in Fig 24. Experimental data are revised in the last two segments according to Sec. 4.6. Overall, despite their high computational cost, the 3–D numerical results show non–negligible scattering among each other, which does not allow one to identify an approach that is more appropriate than the others to reproduce the experiment. However, except for the CPI approach in the first segment, the CPI and API results appear to be comparable to all other predictions. In particular, it is interesting to underline once again that the CPI approach, which neglects the details of injection and combustion, but models the finite–rate reactions in the boundary layer, is still capable of producing an acceptable prediction of the heat flux in the nozzle section with minimal computational effort.

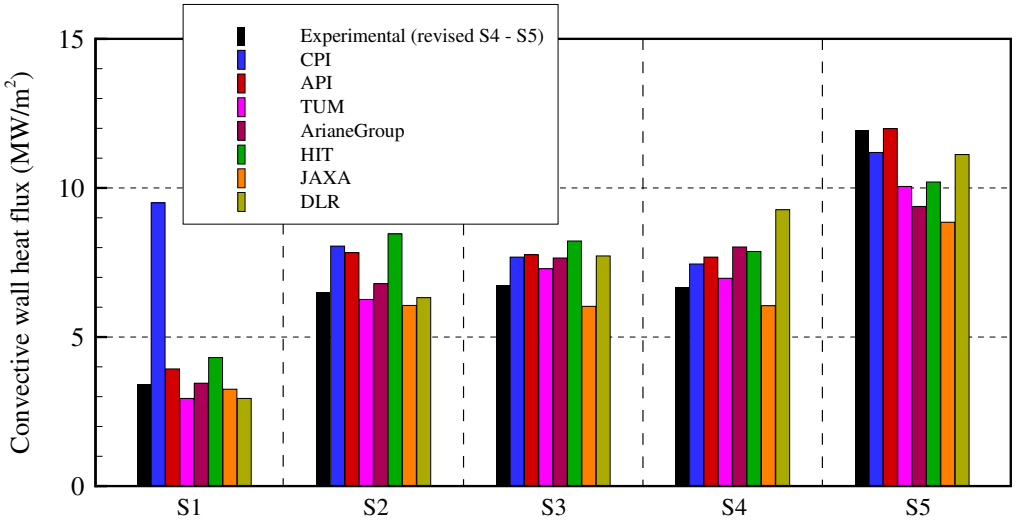

Figure 24: Comparison between numerical results and average wall heat flux obtained in the literature [25] for the selected test case [17]. Revised experimental data are shown in S4 and S5.

Regarding the wall pressure profile comparison, the qualitative trends are similar among the literature results and the API solution. However, a quantitative comparison shows that experimental data are both overestimated and underestimated by the different approaches present in the literature (Fig 25). These variations can be attributed to differences in combustion and TCI modeling [25].

As already observed above, the CPI approach is not capable of accurately predicting the wall pressure profile due to its modeling assumptions. However, the API result is in close agreement with the experimental wall pressure profile.

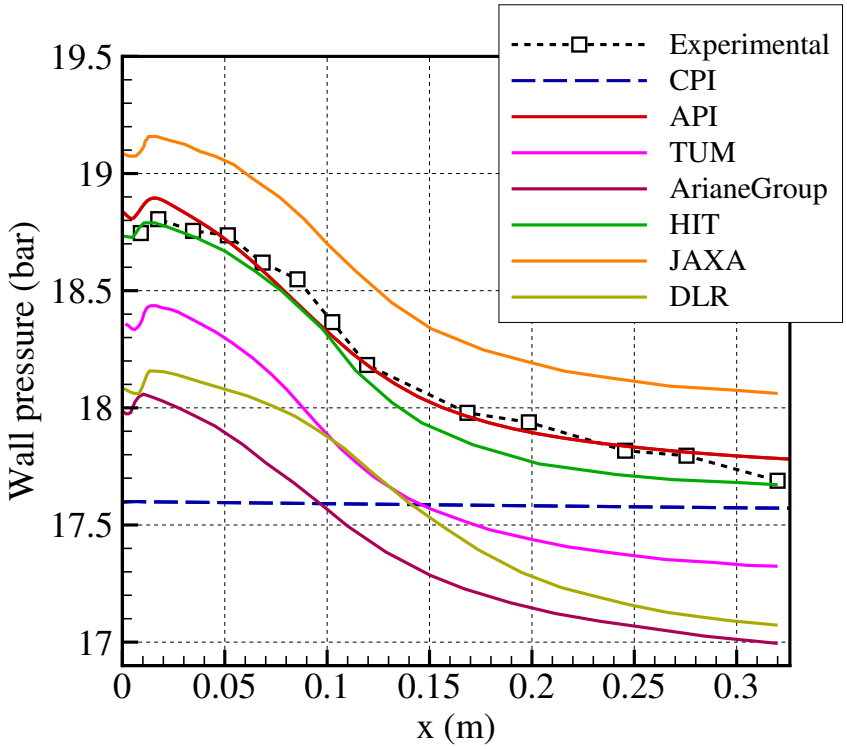

Figure 25: Comparison of numerical wall pressures obtained in the literature [25] with CPI and API results for the selected test case [17].

4.8 FLOWFIELDS

The API and CPI flowfields are compared in Fig. 26 in order to analyze more in detail the numerical solutions obtained with the two approaches, and to further discuss reasons for the differences in wall heat flux obtained at throat (Fig. 21). In the CPI solution, combustion products are injected uniformly at the adiabatic flame temperature at the inlet (Fig. 26a). The hot core flow remains mainly unchanged from the equilibrium inflow condition. The boundary layer starts developing from the injector plate and large temperature variations occur from the wall to the core flow, as also shown in Fig. 27. In the API solution, on the other hand, the flow from the injectors generates two counter–rotating vortexes and a third wide vortex at the corner (Fig. 26a).

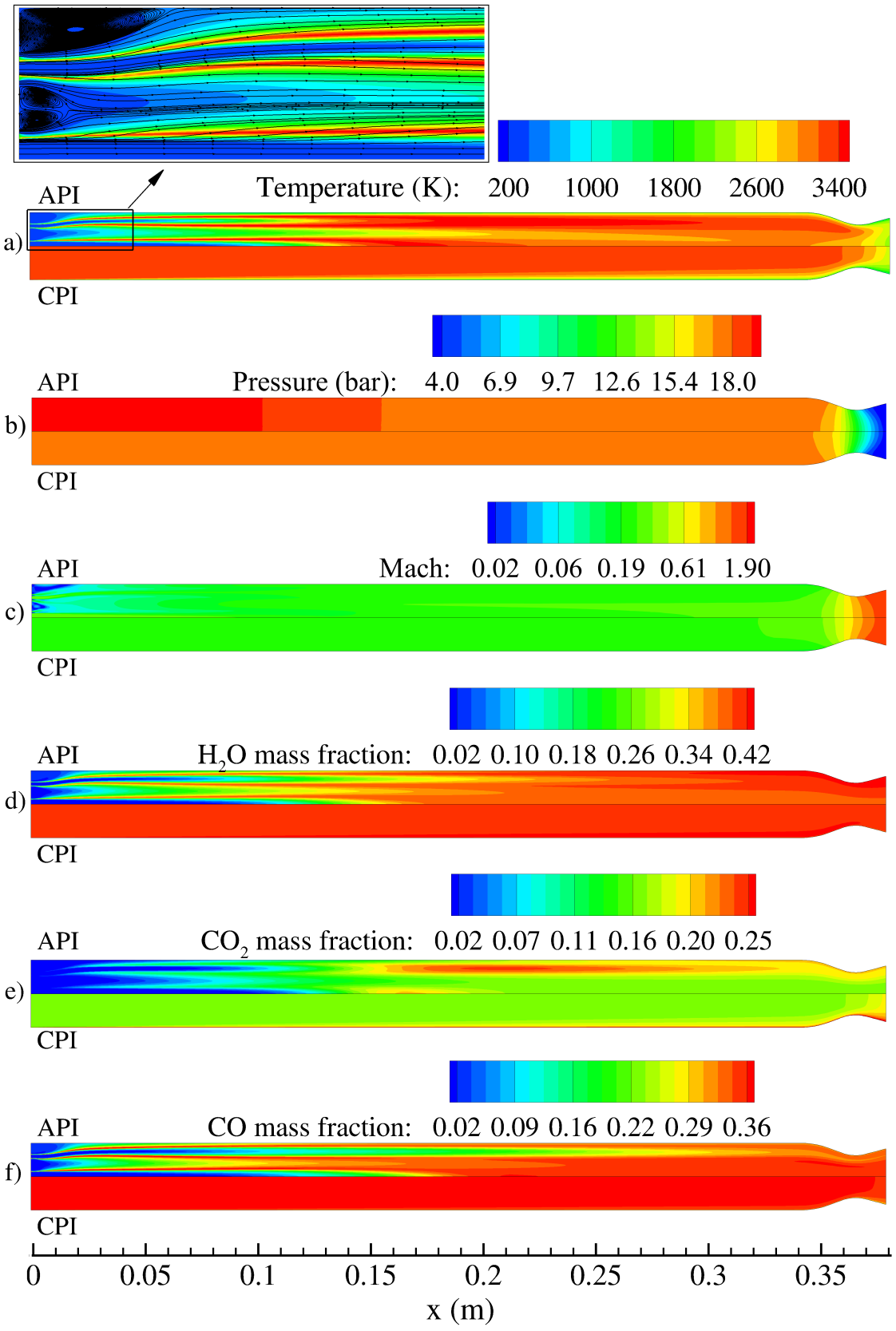

Figure 26: Computed flowfields for reference API (top) and CPI (bottom) simulations.

Three flames develop from the injectors reaching typical temperatures expected in oxygen–methane combustion, eventually merging downstream in a single hot core, which becomes gradually more uniform towards the convergent part of the nozzle (see also Fig. 27). Nevertheless, the API approach provides only a rough representation of the injection and rapid combustion zones (see Fig. 1), due to its modeling assumptions and limitations. A more suitable numerical approach for such zones would have to consider 3–D computational domains, higher grid resolution, turbulence–chemistry interaction (TCI), modeling of detailed and optimized kinetic mechanisms with a realistic amount of species and reactions, which would naturally make it more complete but also much more computationally demanding.

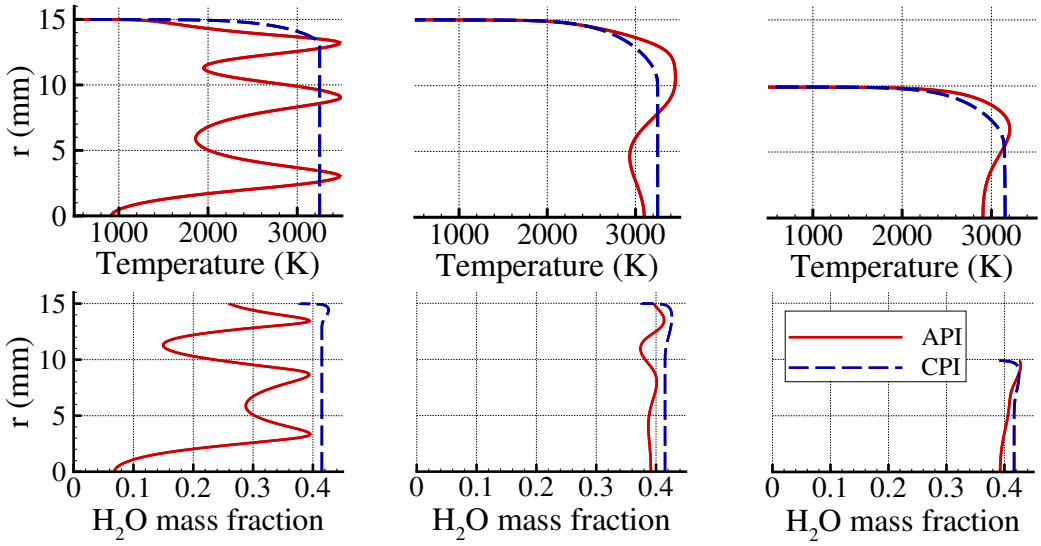

Figure 27: Radial profiles of temperature and H_2O mass fraction for API and CPI calculations at three different locations (x=100 mm, x=250 mm, and throat from left to right).

For these reasons, diffusive mixing is observed to occur to a lesser extent with respect to more detailed simulations performed in the literature [17, 24, 145], which provide a more uniform flowfield already halfway through the combustion chamber. In particular, Eiringhaus et al. [145], carried out and compared 2–D and 3–D simulations for the present test case, and underlined that the correct representation of injectors and momentum exchange provided by a 3–D configuration is the main reason of the enhanced mixing. Therefore, the API simulation provides a more persisting trace of the injectors further downstream from the faceplate with respect to what would be expected in a realistic reproduction of the experiment due to the intrinsic limitations of a 2-D diffusive mixing. This leads to two main consequences: (i) the temperature flowfield is not uniform close to the chamber axis, which is, however, of secondary importance in the framework of this study; (ii) differences with respect to CPI results are expected to be greater than those between CPI and fully 3–D simu-

lations. In this aspect the API result can be considered a *conservative* term of comparison with respect to CPI simulations in the evaluation of nozzle throat heat flux, as if CPI and API results are in agreement, the agreement is expected even better with fully 3D simulations due to their enhanced mixing. Due to the poor mixing entailed by the API simulations, a radial thermal stratification is still visible at the nozzle entrance. Nevertheless, the API radial temperature profiles tend to converge towards the CPI ones (see Fig. 27), yielding a difference in the average temperature of 3% at the throat. The larger temperature gradient at the wall caused by the higher boundary layer edge temperature explains the slightly higher peak wall heat flux of API with respect to CPI shown in Fig. 21.
Regarding the pressure and Mach number contour plots (see Fig. 26b and 26c), the API and CPI solutions do not differ significantly apart from the fore–end of the combustion chamber. In the region where the vortexes are present, the API solution shows a lower Mach number than the CPI one. Moreover, the API

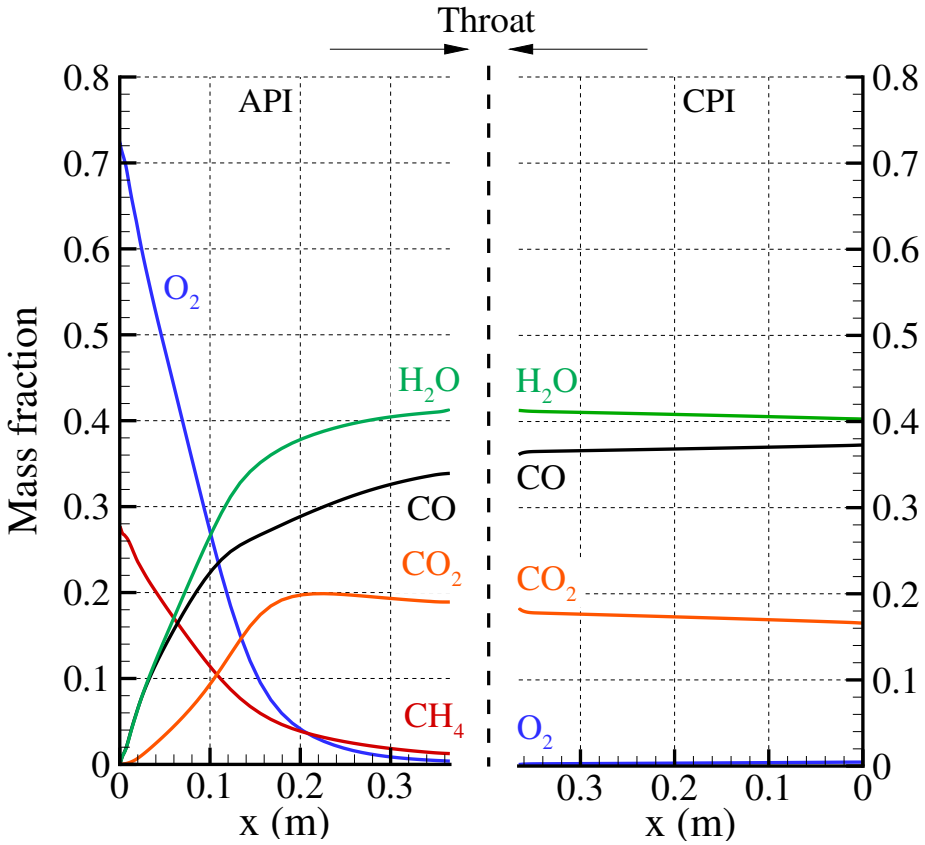

Figure 28: Mass flow-weighted average mass fractions along the combustion chamber.

chamber pressure decreases along the whole chamber (see also Fig. 23), even if a steeper gradient is present in the first half of the chamber due to developing combustion. Pressures obtained from the CPI and API approaches are comparable in the second half of the chamber. The API mass flow–weighted average mass fractions of O_2 and CH_4 rapidly decrease until x$\approx$ 200 mm, where the

combustion process is expected to end according also to Figs. 21 and 23, reaching negligible values of unburned oxygen and only 1.3% of residual methane at the nozzle throat (Fig. 28). Even if methane should not be present at equilibrium conditions, most of its residual is observed close to the chamber axis, hence not affecting significantly the wall conditions.
The main combustion products of oxygen/methane combustion, i.e H_2O, CO_2, and CO, are shown in Fig. 26d-f, respectively. All of them show significant radial variations in the first half of the chamber due to developing combustion. As already observed for the temperature flowfield, the mass fraction of H_2O becomes gradually more uniform towards the nozzle throat, where good agreement with the CPI solution is obtained especially in the near–wall region (see also Fig. 27). However, CO_2 and CO mass fractions show a peculiar behavior in the second half of the chamber, where production of CO_2 occurs in correspondence of a consumption of CO, yielding strong radial non–uniformities which fade away towards the nozzle. Moreveor, fuel–rich zones are characterized by a larger presence of CO, and stoichiometric zones by a larger mass fraction of CO_2. These observations are in agreement with results obtained by Perakis et al. [17]. An increase of CO_2 and H_2O, due to the enhancement of chemical recombinations caused by the enforced low wall temperature, is present in the near–wall region close to the nozzle, in agreement with the CPI solution. The latter shows, in fact, slightly varying average mass fractions due to chemical recombinations (Fig. 28).
The limited predictive capabilities regarding the local species evolution during the combustion process of the API approach should be owed to the global kinetic mechanism employed in this study, which is not as comprehensive and accurate as more detailed and optimized kinetic mechanisms for oxygen/methane combustion. Nevertheless, the mass flow–weighted average mass fractions along the combustion chamber of the API solution tend to converge towards their respective CPI values as the throat is approached, with a maximum error of 6% for the CO mass fraction (Fig. 28). Given the sufficiently complete mixing and combustion inferred on average by the API approach (considering it conservative due to its modeling assumptions), it can be concluded that a characteristic length of $L^* = 0.90$ m, which characterizes the present test case, can be considered valid to promote sufficiently high combustion efficiencies in oxygen–methane LREs. The L^* is calculated as the ratio between the chamber volume until the nozzle throat and the throat area. This also justifies the adoption of the simplified CPI approach for design purposes regarding nozzle throat wall heat flux, as it will be even clearer from the analysis of combustion efficiency reported in Section 4.9.

4.9 COMBUSTION EFFICIENCY

A further parameter assessing the completion of combustion and mixing obtained with the different numerical approaches and the experiment is the characteristic velocity. Its value is usually compared in terms of combustion efficiency that is the ratio of the measured or computed characteristic velocity to its ideal value. More specifically, the combustion efficiency is calculated as

$$\eta_{c^*} = \frac{c^*}{c^*_{id}} = \frac{p_c \, A_{th}}{\dot{m} \, c^*_{id}} \tag{125}$$

using the experimental mass flow rate and throat area (see Sec. 4.1) and clearly identified values of chamber pressure and reference (ideal) characteristic velocity. For this purpose, a suitable value of the chamber pressure p_c in both API and CPI approaches is computed as the radial integral average of total pressure at the nozzle entrance ($x = 341$ mm):

$$p_c = \frac{1}{\pi r_c^2} \int_0^{r_c} 2\pi r p_0(r) \, dr \tag{126}$$

where $p_0(r)$ is the local total pressure, approximately evaluated as:

$$p_0(r) = p(r) \left(1 + \frac{\gamma - 1}{2} M^2\right)^{\frac{\gamma}{\gamma - 1}} \tag{127}$$

being γ and M the local specific heat ratio and Mach number, respectively. The CEA program has been employed to calculate the ideal characteristic velocity c^*_{id} with the equilibrium and adiabatic assumptions given the experimental mixture ratio of 2.65 and chamber pressure as calculated by Eq. (126). As a result, the computed combustion efficiencies of the reference API and CPI numerical solutions are 93.3% and 94%, respectively (see Table 8). Since experimental information on total pressure is not readily available, a direct comparison with measured data is performed by computing a different efficiency, obtained with the wall rather than the total pressure. This efficiency is defined here as:

Table 8: Experimental and numerical combustion efficiencies calculated by means of wall pressure (p_w) and chamber pressure (p_c, see Eq. (126)) evaluated at nozzle entrance ($x = 341$ mm) for different flow models.

	p_w(bar)	$\eta_{c^*,w}$	p_c(bar)	c^*_{id}(m/s)	η_{c^*}
EXP	17.7	0.913	18.3	1887.8	0.945
API	17.5	0.901	18.1	1887.7	0.933
CPI isothermal	17.6	0.907	18.2	1887.8	0.940
CPI adiabatic	18.7	0.965	19.4	1888.7	0.999

$$\eta_{c^*,w} = \frac{p_w A_{th}}{\dot{m} c^*_{id}} \tag{128}$$

With $\eta_{c^*,w}$, the numerical combustion efficiencies (90.1% for API and 90.7% for CPI) are in good agreement with the experimental value of 91.3%, calculated with the most downstream wall pressure measurement shown in Fig. 23. To obtain a more realistic value of η_{c*}, the experimental total pressure can be estimated on the basis of the numerical computations, for which the chamber pressure p_c is about 3.5% higher than the wall pressure p_w at the nozzle entrance. Therefore, the estimated value of the experimental chamber pressure is 18.3 bar, and the resulting experimental combustion efficiency is 94.5% (see Table 8). According to the literature [2], the mentioned values of combustion efficiencies are quite low, which implies that a considerable amount of losses is occurring. Such energy losses may occur due to three main factors: heat exchange, friction, and incomplete combustion. To analyze the different impacts of such phenomena on combustion efficiency, a further CPI simulation that enforces the experimental mass flow rate (0.291 kg/s) with adiabatic wall boundary conditions was carried out. By comparing the CPI isothermal and adiabatic results in Table 8, it is clear that the predominant phenomenon lowering the combustion efficiency is the heat loss caused by the low wall temperature, which yields about 6% efficiency reduction. Since $\eta_{c*} \approx 1$ for the CPI adiabatic simulation, combustion efficiency losses due to friction are negligible for this test case. Moreover, since the value of η_{c*} of the CPI isothermal compares well to the experimental one, incomplete combustion losses are also negligible. Differences in efficiencies are small enough to be considered within the measurement and computation uncertainties. On the other hand, it is interesting to note that the API efficiency is the lowest, which confirms the expected lower mixing and combustion efficiency given by the simplified combustion model.

4.10 WALL HEAT FLUX NUMERICAL CORRELATION

A satisfactory prediction of the wall heat flux at the nozzle throat has been obtained by both CPI and API approaches at the reference condition ($p_c = 18.3$ bar and $\dot{m} = 0.291$ kg/s). This section aims at evaluating the agreement between the two approaches in an extended range of operating conditions, in order to finally provide a numerical correlation for the wall heat flux as a function of pressure.

The chamber pressure in the API simulations is varied by increasing the mass flow rates of the propellants up to doubling the reference value, achieving a maximum chamber pressure of 37.2 bar (as calculated by Eq. (126)). On the other hand, for the CPI approach the total pressure is directly imposed at the inlet in the range 18.3 – 100 bar and the corresponding mass flow rate is computed. The mixture ratio is kept constant in both approaches. Wall heat flux results are shown as a function of chamber pressure in Fig. 29a and mass flow rate in Fig. 29b for the mid chamber ($x = 191.5$ mm) and the nozzle throat

(x = 365.6 mm). Solutions computed with both CPI and API approaches follow a power law over the considered pressure ranges. Similar distributions are observed as a function of mass flow rate. A good agreement between the two numerical results is observed at the reference condition (see also Fig. 21) and also at a higher chamber pressure for both mid chamber and throat locations. This indicates that the effects of a detailed modeling of injection and combustion processes (zones 1 and 2 in Fig. 1) can be reasonably considered negligible in the evaluation of wall heat flux even upstream of the transonic region of the thrust chamber (zone 4).

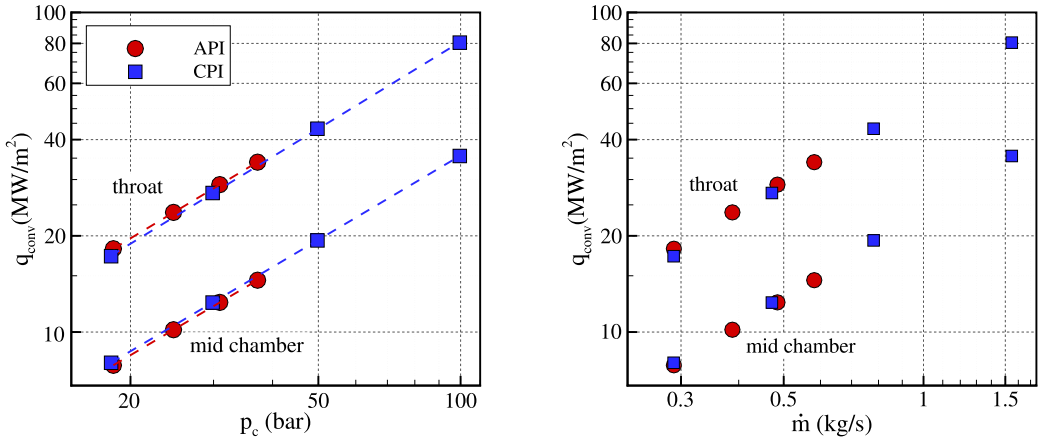

Figure 29: Convective wall heat fluxes at mid chamber and throat locations for different conditions obtained using the API and CPI approaches for O/F = 2.65. Dashed lines correspond to Eq. (129) and Table 9.

The convective wall heat flux as a function of chamber pressure is well described by the following correlation law (see Fig. 29a):

$$q_{conv} = a\, p_c^b \tag{129}$$

where q_{conv} is in MW/m², p_c in bar, and the coefficients a and b are listed in Table 9. The pressure exponents obtained with the two numerical approaches are in excellent agreement with each other, and are slightly higher than the one predicted by the Bartz equation [1], which is 0.8. Despite the lack of experimental data in the literature, the extension of the pressure range up to 100 bar in case of CPI simulations allows for a reasonable comparison with a few analyses considering different setups and operating conditions. Kumakawa et al. [14] obtained similar trends to those of Fig. 29a in the pressure range 35 – 96 bar with a wide range of O/F. In addition, Betti et al. [116] presented heat flux at mid chamber at O/F = 3.34 in a pressure range of 10 – 100 bar, which can be fitted with a power law with a pressure exponent of 0.88, in line with what presented in Table 9. Such favorable comparisons provide a reasonable expectation that

the wall heat flux regression laws presented in this work might be used to aid the design of LRE. The correlation law in Eq. (129) can be considered valid

Table 9: Regression coefficients of Eq. (129) for convective heat flux evaluation as a function of chamber pressure at mid chamber and throat locations.

	CPI		API	
Location	Throat	Mid chamber	Throat	Mid chamber
b	0.90	0.88	0.89	0.87
a, MW/(bar^b· m^2)	1.25	0.63	1.37	0.62

also to carry out acceptable predictions of the total wall heat flux, especially at throat. In fact, the radiative wall heat flux, even if always increasing with pressure, reaches values up to $\approx$ 2 MW/m^2 in the considered pressure range (Fig. 30), and is considerably lower than the convective contributions shown in Fig. 29a. Radiative heat flux is calculated using the model presented in Sec. 2.2.

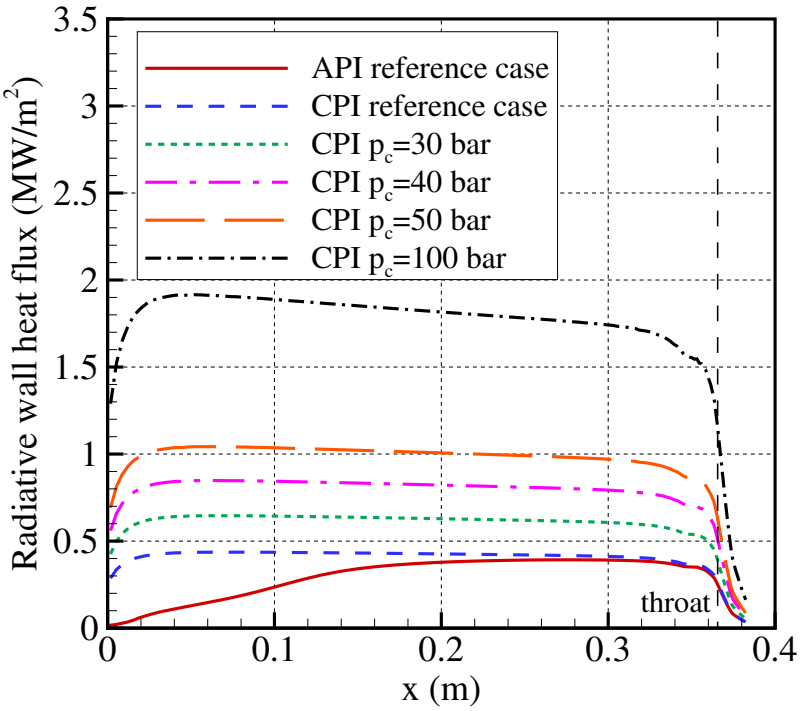

Figure 30: Radiative wall heat flux obtained using the API and CPI approaches at different pressures and O/F=2.65.

It is interesting to note that good agreement between API and CPI radiation heat profiles is obtained in the second half of the chamber at the reference case. The radiation contribution to the total wall heat flux in the considered pressure range is limited to 5% in the cylindrical part of the combustion chamber, while it is negligible at throat ($\approx$ 1%). This is in agreement with previous

oxygen–methane radiation evaluations [124], which predicted a radiative–to–total contribution less than 20% for chamber diameters lower than 0.1 m. The same predominance of convective heat flux has been observed also for other values of mixture ratio.

4.11 MODEL SUITABILITY FOR LONGER CHAMBERS

The numerical simulations of the investigated thrust chamber have shown from different points of view that the CPI approach is capable to provide a reliable and quick estimation of the throat heat flux. It has been shown that no matter how complex the flowfield is until the end of the streamtube region, the flowfield close to the throat wall will be reproduced within reasonable computational times by CPI numerical simulations.

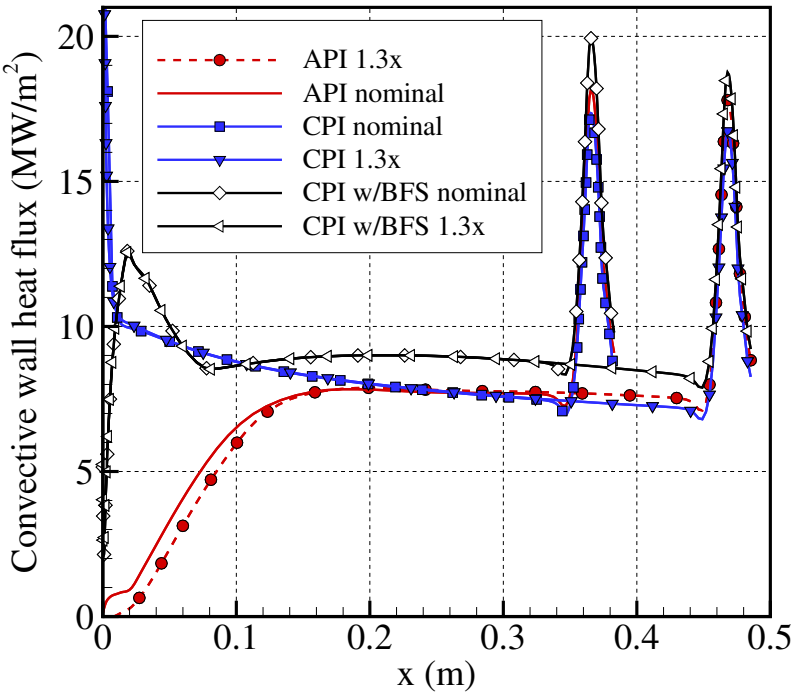

Figure 31: Throat heat flux comparison among different simulation approaches of the reference and elongated (1.3x) thrust chambers.

However, an important point to focus on is to verify that the agreement found between the CPI and API simulations on the throat heat flux ($\approx 5\%$) does not depend critically on the chamber geometry. In particular, in this section the effect of a combustion chamber elongation on the flowfield development, and thus on the near–wall throat region, is investigated. For this purpose, the thrust chamber described in Sec. 4.1 is modified by elongating the rapid com-

bustion/streamtube regions by 1/3 of their original length (321 mm), yielding a combustion chamber total length of 448 mm. Note that the L^* is increased from 0.90 to 1.17 m. Therefore, the CPI and API approaches have been employed to carry out numerical simulations on such a new thrust chamber, eventually comparing the agreement observed on the throat heat flux to that obtained at the reference case. To mantain the experimental mass flow rate, the CPI simulations of the longer chamber are performed enforcing mass flow rate and not total pressure. Heat flux profiles are shown in Fig. 31, whereas percentage discrepancies among peak heat fluxes are shown in Table. 10.

Table 10: Percentage discrepancies between convective wall heat flux at throat using different approaches and chamber lengths.

(%)	API	CPI	CPI_{BFS}	$API_{1.3x}$	$CPI_{1.3x}$	$CPI_{1.3x,\ BFS}$
API	0	5.2	-9.7	2.0	–	–
CPI	-5.4	0	-14.9	–	3.6	–
CPI_{BFS}	8.8	12.9	0	–	–	5.9
$API_{1.3x}$	-2.1	–	–	0	6.0	-5.3
$CPI_{1.3x}$	–	-3.7	–	-6.4	0	-12.1
$CPI_{1.3x,\ BFS}$	–	–	-6.3	5.1	10.8	0

As shown in Table. 10 concerning the CPI and the API approaches, it can be observed how the discrepancy begins to diverge, starting from 5.2% and increasing to 6% when the combustion chamber is elongated. This happens due to the further development of the boundary layer, which becomes very thick as the throat is approached. In this regard, Fig. 32 shows the temperature fields for the reference and elongated chambers employing the different numerical approaches. Note that the shorter chambers are right–shifted to match the throat abscissa with the longer ones. The difference on boundary layer thicknesses at throat is clearly visible in case of the CPI simulations. On the other hand, a better mixing occurs in case of API, yielding lower temperature gradients toward the throat.

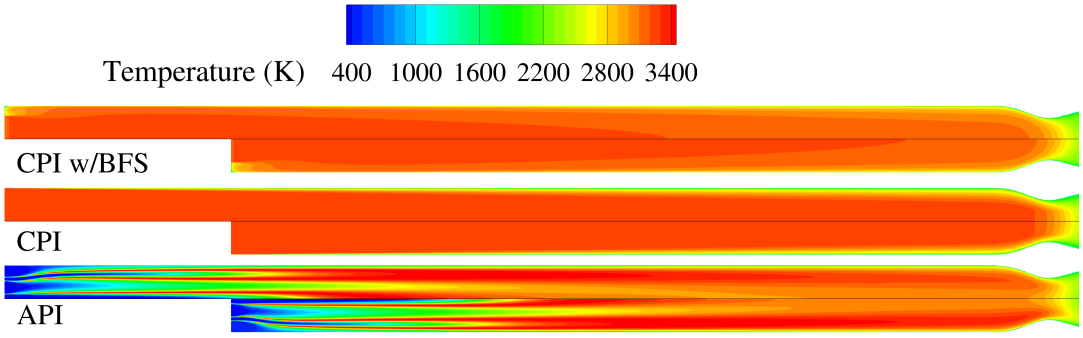

Figure 32: Temperature fields obtained by means of different approaches for the reference and elongated thrust chambers.

As it can be inferred from these results, the boundary layer growth represents a problem for the CPI approach, since the longer the chamber is, the more discrepant the throat heat flux becomes with respect to API results. To overcome such a modelling problem, a modification is introduced in the CPI approach, maintaining at the same time its characteristic simplicity and computational burden. In particular, a backward–facing step (BFS) is introduced at the injection plate between the hot gas inflow and the wall. The CPI approach with the BFS, hereafter called *CPI w/BFS*, is employed to perform further numerical simulations, as a term of comparison for the original CPI. To be coherent with the API simulations, the height of the BFS is chosen in such a way to match the distance between the most external fuel injector and the wall in the API injector plate configuration, i.e. $(r_c - r_9)$ according to Fig. 15. Nevertheless, different near–injector features are observed.

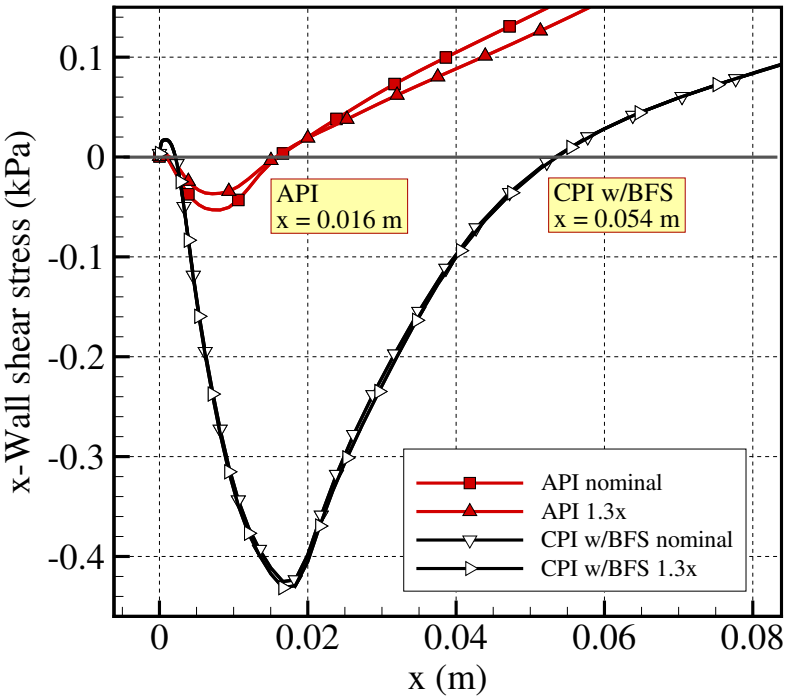

Figure 33: Wall shear stresses observed in the vicinity of the injection plate for API and CPI w/BFS simulations.

In particular, the extension of the recirculation zone is different between API and CPI w/BFS simulations. This can be inferred by observing the sign change on the x–component of the wall shear stress obtained in the two cases as shown in Fig. 33. The latter is negative as far as the wall is wet by the counterclockwise–rotating vortex (see also inset in Fig. 26), and becomes positive in correspondence of the flow impingement point. Such a difference can be explained through the velocity fields, shown in Fig. 34. As far as the CPI w/BFS solution is concerned, a higher injection velocity is obtained due to the lower

injection area. That leads to a wider recirculation zone and, thus, a farther flow impingement point.

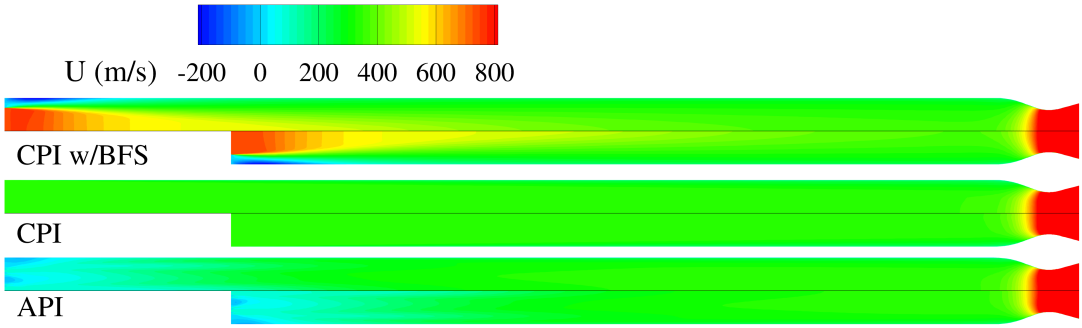

Figure 34: Velocity fields obtained by means of different approaches for the reference and elongated thrust chambers.

Moreover, it has been observed that enforcing the total pressure at the inlet boundary, as done for the CPI simulations, yields a lower mass flow rate of 5.2%, thus not providing an appropriate term of comparison for the other numerical approaches. For this reason, the experimental mass flow rate is enforced at the left boundary in CPI w/BFS simulations. The resulting temperature fields are shown in Fig. 32. The effect of the BFS is well distinguishable with respect to the CPI flowfield, and, in particular, the effect of the boundary layer growth is attenuated. The discrepancies on the throat heat fluxes with respect to the API approach shown in Table. 10 confirm this observation. Although the CPI w/BFS approach provides a higher discrepancy than the CPI concerning the API reference chamber (-9.7%), the latter is reduced as the chamber gets longer (-5.3%). That indicates that the BFS addition to the near–injector modelling is a good improvement to the CPI approach, since the throat heat flux tends to converge toward that of API. Nevertheless, it should be noted that the CPI approach provides better results in the shorter case, so the employment of one model or the other one still remains a decision to take carefully. The characteristic length, evaluated above in the two cases, represents an indicator which might help in the choice during the design.

5 FILM–COOLED AND MIXTURE RATIO BIASED CHAMBERS

As a continuation of the work presented in Chap. 4, this part of the thesis aims at presenting and discussing the CFD numerical results obtained analyzing the throat wall region in film cooled and mixture ratio biased LRE thrust chambers. The main idea driving this part of the work is to define and fix the operating conditions of the engine in terms of mass flow rate and mixture ratio to those of the uncooled configuration, and to study how the secondary flow should be designed in order to obtain a desired effect on the throat wall heat flux with acceptable engine performance loss. In this framework, a sensitivity analysis is performed to select the design parameters producing major effects on the throat wall heat flux reduction, eventually obtaining a numerical correlation which allows to immediately predict the necessary information during the design phase. In this regard, it should be said that the design of the secondary flow is a delicate procedure in which decisions have to be taken carefully, since an high amount of coolant, which yields a high heat flux reduction at throat, would end up in an excessive performance loss. For this reason, CFD throat heat flux numerical results will be presented with their performance loss counterpart to directly evaluate the trade–off.

In the second part of this chapter, a different configuration is employed on the same thrust chamber to study the effect of a bias in the peripheral injectors mixture ratio on the throat wall heat flux and engine performance reduction. The peripheral flow mixture ratio is investigated within a comprehensive range from oxidizer–rich to fuel–rich conditions. In this regard, although the bias of the outer injectors mixture ratio is usually used to yield a fuel–rich mixture close to the wall in order to reduce the thermal load, the oxidizer–rich region has been also investigated despite the lower practical interest.

The test chamber is illustrated in the first part of the chapter together with the computational setup used to carry out CFD simulations in presence of film cooling and mixture ratio bias, whereas numerical results are presented in the final part.

5.1 TEST CASE

A thrust chamber representative of a possible methane-fueled upper stage (MFUS) has been selected as test case. This thrust chamber has been used also in Ref. [124] to investigate radiative heat loads in LRE thrust chambers without the application of any active cooling system. However, the design and the

operating conditions have been considered suitable to introduce a secondary flow injection at the injection plate, and to study the behaviour of peak heat flux according to different configurations in a parametric analysis. A depiction of the thrust chamber is shown in Fig. 35.

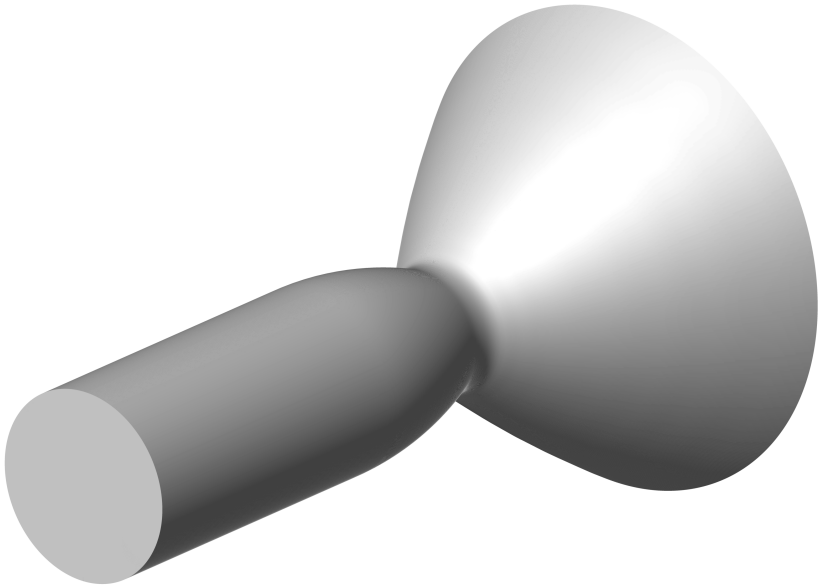

Figure 35: Depiction of the methane–fueled upper stage thrust chamber used to perform numerical simulations.

The geometry has been taken from Ref. [146], whereas a chamber pressure of 60 bar and a mixture ratio of 3.4 have been arbitrarily selected as reasonable for oxygen–methane upper stage operations [10]. The mentioned test case features a 730 mm long thrust chamber with a throat diameter of 116 mm, and a combustion chamber contraction ratio of 2.25. Total and fuel mass flow rates are 34.5 and 7.84 kg/s, respectively. As attention is focused on the wall heat transfer far away from the injector plate, details of the plate geometry are relatively unimportant. Nevertheless, a set of parameters defining the secondary flow injection geometry are necessary for the present investigation. The latter are described in Sec. 5.2.

5.2 NEAR–INJECTOR GEOMETRY

Being this chapter aimed at investigating the effects of a secondary flow injection in an already–identified (uncooled) thrust chamber, it is reasonable to consider such a configuration as a reference condition for all the film cooling calculations. This is not appropriate for mixture ratio bias simulations, as will be explained later in the chapter.

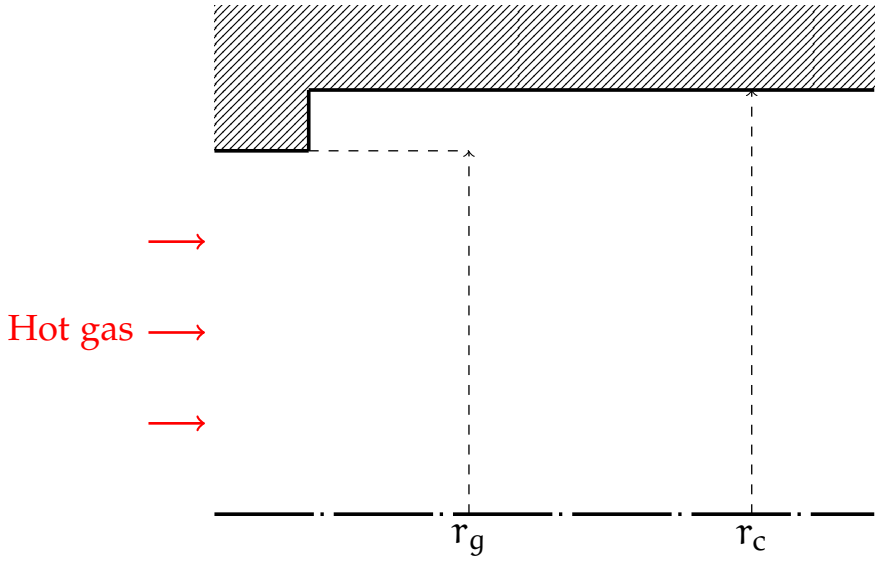

Figure 36: Schematic of the near–injector region in case of uncooled simulations performed by means of the CPI w/BFS approach.

The CPI w/BFS approach, mentioned and validated in Sec. 4.11, has been considered more suitable to carry out the numerical simulation of the uncooled configuration than the CPI (see Sec. 4.2), since it is more comparable to the typical film cooling geometry featuring two inflows and a separating wall in between. A schematic of the near–injector region is shown in Fig. 36, where $r_g = 82$ mm and $r_c = 87$ mm. In case of film cooling simulations, the near–injector region of the combustion chamber shown in Fig. 36 has been modified by introducing the film injection slot close to the wall. The new geometry is shown in Fig. 37, where $r_{film} = 86$ mm. Note that, as a result, a total distance of 5 mm ($r_c - r_g$) is then interposed between the hot gas inflow and the chamber upper wall. In sight of the parametric analysis, a nominal configuration has been identified in terms of four design parameters, i.e. the film injection slot height h_{slot} ($r_c - r_{film}$ in Fig. 37), the thickness of the wall which separates the hot gases and the film inflows t_{wall} (i.e. $r_{film} - r_g$), the blowing ratio $B = (\rho u)_g / (\rho u)_{film}$, and the film injection temperature T_{film}. The values of such parameters for the nominal configuration have been arbitrarily determined in the frame of this research, as reasonable for a possible upper–stage application also on the basis of the literature [101, 140]. They are $h_{slot} = 1$ mm, $t_{wall} = 4$ mm, $B = 0.66$, and $T_{film} = 300$ K. Eventually, as foreseen by the CPI–like approaches, combustion products obtained at chemical equilibrium under the mentioned operating conditions are considered as hot gases. Pure gaseous methane is instead retained as film coolant, which is expected to mix and react with the hot gases according to the employed chemical reaction mechanism. On the other hand, numerical simulations featuring mixture ratio bias do not foresee a secondary flow injection in the immediate vicinity of the wall. In fact, a bias in mixture ratio usually occurs at the outer injector row, close to the

hot gas inflow as modeled by the CPI w/BFS approach. Such a geometry is modeled as shown in Fig. 38, where $r_g = 80$ mm, $r_{bias} = 81$ mm, and $r_{wall} = 82$ mm.

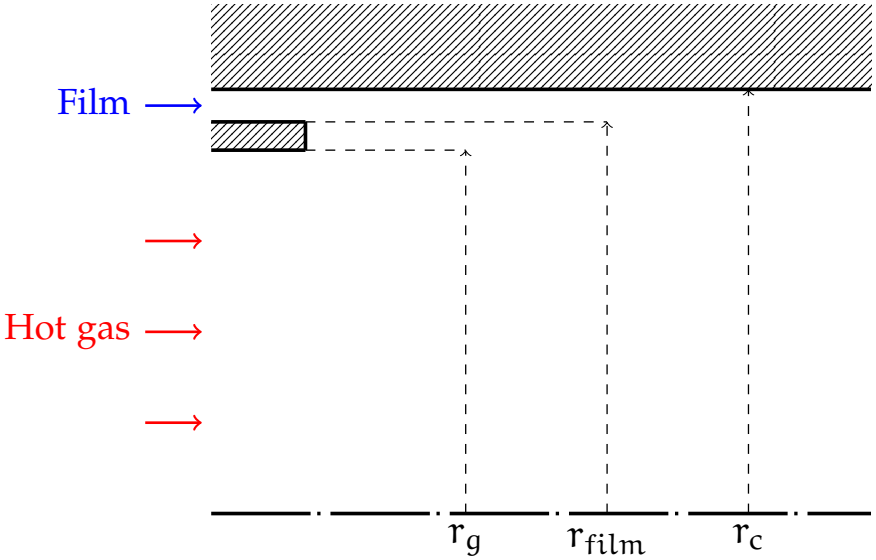

Figure 37: Schematic of the near–injector region in case of film cooling simulations. Not to scale.

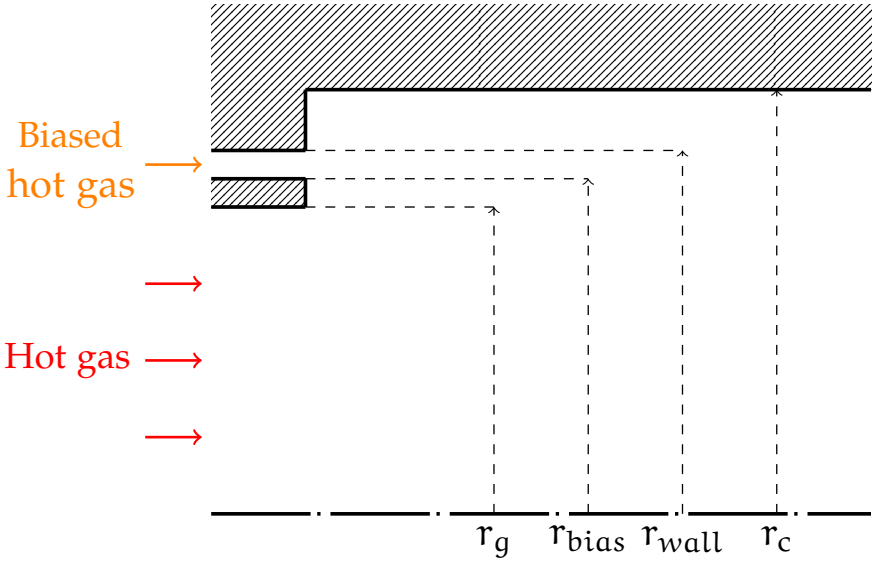

Figure 38: Schematic of the near–injection region in case of mixture ratio bias simulations. Not to scale.

Two different mixture ratios can be identified in such a configuration, one for the hot gas (O/F_g), and one for the peripheral flow (O/F_{bias}). Moreover, differently from the film injection of pure methane, the peripheral mixture is

possibly composed of all the species involved in the chemical reaction mechanism, depending on the operating conditions. For this reason, in this case the CEA program is used to determine not only the composition of the hot gases, but also that of the peripheral flow according to chamber pressure and the mixture ratio O/F_{bias}. The peripheral mixture temperature is then provided by CEA. The peripheral mixture ratio is the only varying parameter in this case, therefore the values of the near–injector geometric quantities are always the same. In particular, $t_{wall,1} = r_{bias} - r_g = 1$ mm and $t_{wall,2} = r_c - r_{wall} = 5$ mm (see Fig. 38). For the sake of simplicity, the blowing ratio, now defined as the ratio between the hot gas and peripheral flow mass fluxes, is fixed to that of the film cooling nominal configuration, i.e. 0.66.

5.3 MASS FLOW RATE MANAGEMENT

A central point of this analysis is represented by the mass flow rate management, which is accurately described in this section. As mentioned in Sec. 5.2, in this analysis the injection of the secondary flow occurs in a previously well–designed combustion chamber, thus assuming that the design of the uncooled engine has been already performed. Hence, the total mass flow rate $\dot{m} = \dot{m}_f + \dot{m}_{ox}$ and the global mixture ratio O/F can be considered fixed to those of the uncooled configuration provided in Sec. 5.1, i.e. 34.5 kg/s and 3.4, respectively. Having that as a starting point, the total available mass flow rate is supposed to be split between the hot gas ($\dot{m}_g$) and the secondary flow ($\dot{m}_2$, later distinguished between $\dot{m}_{film}$ and $\dot{m}_{bias}$) to study the resulting effect on the throat heat flux and performances. The blowing ratio, the secondary flow methane mass fraction y_{CH_4}, and the near injector geometry, defined through the injection slot height and the separating wall thickness in case of film cooling or through the same height and the two wall thicknesses $t_{wall,1}$ and $t_{wall,2}$ in case of mixture ratio bias, are the parameters driving the mass flow rate splitting process. In particular, after fixing the near–injector geometry to that of the desired configuration, the blowing ratio and the secondary flow methane mass fraction are varied to define the two mass flow rates according to the procedure described in the following.

In this context, the split hot gas and secondary mass flow rates are subjected to two constraints:

$$\dot{m}_g + \dot{m}_2 = \dot{m} \qquad \text{and} \qquad \frac{\dot{m}_{g,ox} + \dot{m}_{2,ox}}{\dot{m}_{g,f} + \dot{m}_{2,f}} = O/F \tag{130}$$

where subscripts f and ox refer to fuel and oxidizer, respectively. The first constraint is satisfied by solving the following 4–unknowns 4–equations system:

$$\begin{cases} \dot{m}_g + \dot{m}_2 = \dot{m} \\ \dot{m}_2 = (\rho u)_2 A_2 \\ \dot{m}_g = (\rho u)_g A_g \\ (\rho u)_g = B(\rho u)_2 \end{cases} \tag{131}$$

where A_2 is the secondary flow injection area. The solution of such a system of equations is the following:

$$\dot{m}_g = \frac{\dot{m}\, B\, A_g}{B\, A_g + A_2} \tag{132}$$

$$(\rho u)_g = \frac{\dot{m}_g}{A_g} = \frac{\dot{m}\, B}{B\, A_g + A_2} \tag{133}$$

$$(\rho u)_2 = \frac{(\rho u)_g}{B} = \frac{\dot{m}}{B\, A_g + A_2} \tag{134}$$

$$\dot{m}_2 = (\rho u)_2 A_2 = \frac{\dot{m}\, A_2}{B\, A_g + A_2} \tag{135}$$

As shown in Eqs. 132 and 135, split mass flow rates depend only on known parameters, i.e. the total mass flow rate, the blowing ratio and injection areas.

Once the split mass flow rates have been obtained, their fuel and oxidizer contents can be calculated. For this purpose, the secondary flow methane mass fraction is employed to compute the secondary flow mixture ratio:

$$O/F_2 = \frac{1 - y_{CH_4}}{y_{CH_4}} \tag{136}$$

Notice that, being the coolant pure methane, film cooling simulations are always characterised by a secondary flow mixture ratio of 0. Then, the secondary flow fuel and oxidizer contents are calculated as:

$$\dot{m}_{2,f} = \dot{m}_2 \frac{1}{1 + O/F_2} \qquad \dot{m}_{2,ox} = \dot{m}_2 \frac{O/F_2}{1 + O/F_2} \tag{137}$$

and, therefore, the corresponding contents in the hot gases are:

$$\dot{m}_{g,f} = \dot{m}_f - \dot{m}_{2,f} \qquad \dot{m}_{g,ox} = \dot{m}_{ox} - \dot{m}_{2,ox} \tag{138}$$

The hot gas mixture ratio can be now calculated as:

$$O/F_g = \frac{\dot{m}_{g,ox}}{\dot{m}_{g,f}} \tag{139}$$

A simple manipulation of Eq. (138) proves that also the second constraint shown in Eq. (130) is satisfied.

This procedure is applied both to film cooling and mixture ratio bias applications, except for the calculation of the secondary flow injection areas, which, in the two cases, are given by:

$$A_{film} = A_c - \pi (r_c - h_{slot})^2 \tag{140}$$

$$A_{bias} = \pi \left[(r_c - t_{wall,2} + h_{slot})^2 - (r_c - t_{wall,2})^2 \right] \tag{141}$$

As described above, the mass flow rate splitting procedure and, in particular, the constraints shown in Eq. (130), establish a specific relationship between the two mixture ratios attributed to the hot gas and to the secondary flow. With regard to the mixture ratio bias simulations computational setup, which is the most interesting case from this point of view, the resulting behaviour of the two mixture ratios as a function of the peripheral flow methane mass fraction is shown in Fig. 39.

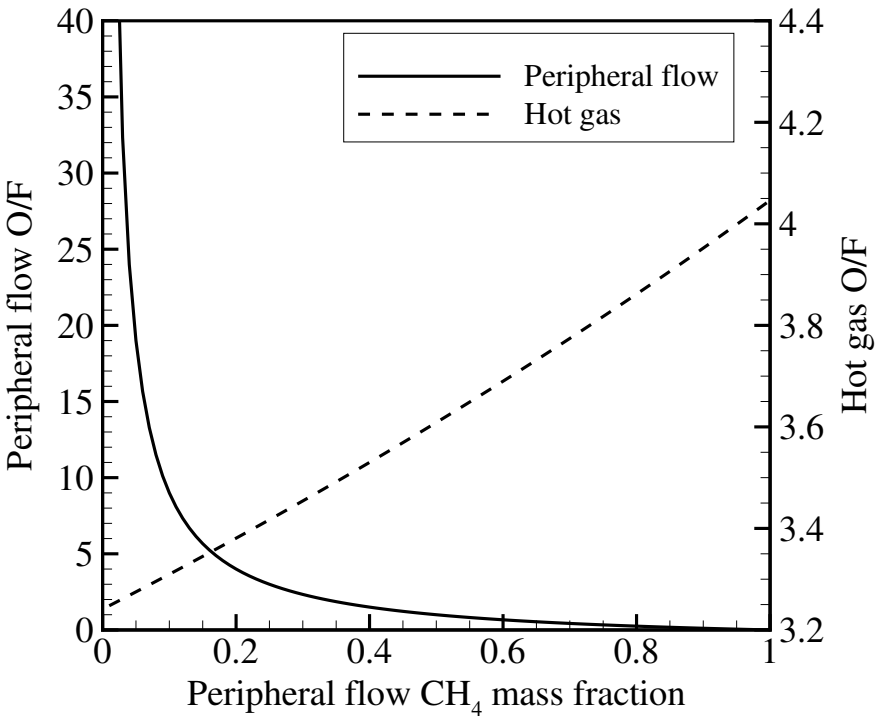

Figure 39: Hot gas and peripheral flow mixture ratio as resulting from the mass flow rate splitting procedure in case of mixture ratio bias simulations keeping the global mixture ratio to 3.4.

It can be observed that, for a fixed blowing ratio (0.66 in the present case), an almost pure oxidizer peripheral flow corresponds to the minimum hot gas mixture ratio since the maximum oxidizer content has been transferred from the hot gas to the secondary flow. On the other hand, a pure methane peripheral flow yields the maximum hot gas mixture ratio since the maximum

amount of fuel has been subtracted from the hot gas and added to the secondary flow. Note that, for blowing ratios of practical interest, the hot gas mixture ratio does not undergo significant modifications, varying between 3.25 and 4.05 in the present case. Peripheral flow methane mass compositions in the range 0.025 – 0.90 have been considered in this analysis, for a total of 15 pairs of hot gas and peripheral flow mixture ratios. The latter are shown in Table. 11.

Table 11: Hot gas and peripheral mixture ratios for different peripheral flow methane mass fractions.

y_{CH_4}	O/F_g	O/F_{bias}
0.025	3.26	39.00
0.05	3.275	19.00
0.10	3.31	9.00
0.15	3.34	5.67
0.20	3.38	4.00
0.25	3.42	3.00
0.30	3.45	2.33
0.35	3.49	1.86
0.40	3.53	1.50
0.45	3.57	1.22
0.50	3.61	1.00
0.60	3.69	0.67
0.70	3.77	0.43
0.80	3.86	0.25
0.90	3.95	0.11

It should be observed that, when investigating the whole range of methane mass compositions, conditions in which the peripheral flow is such to provide a higher equilibrium temperature than the hot gases may occur. Of course, such a situation is not appropriate to achieve an effective wall thermal protection. To overcome this problem, all the peripheral flow mixture ratios capable to provide a higher equilibrium temperature than that of the uncooled configuration (3531 K) have been neglected. As shown in Fig. 40, a mixture ratio of 4.15 provides an equilibrium temperature of 3531 K at the design chamber pressure of 60 bar. Therefore, being the design mixture ratio equal to 3.4, all the peripheral flow mixture ratios between 3.4 and 4.15 have been neglected in the present analysis (see the shaded area in Fig. 40).

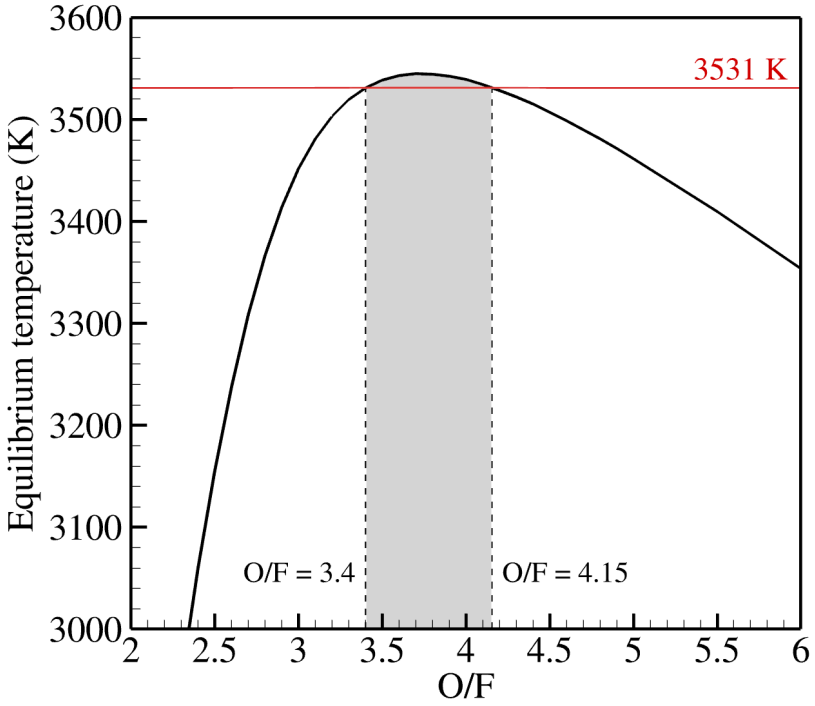

Figure 40: Oxygen–methane equilibrium temperature provided by CEA at different mixture ratios and chamber pressure of 60 bar. The shaded area corresponds to the neglected peripheral flow mixture ratios.

As a result, the methane mass fraction of 0.20 has not been investigated by means of CFD simulations since, according to Table. 11, it provides a peripheral flow mixture ratio $O/F_{bias} = 4.00$.

5.4 COMPUTATIONAL GRIDS AND BOUNDARY CONDITIONS

The computational domain is a single–block 2–D axisymmetric structured grid for both film cooling and mixture ratio bias simulations.

5.4.1 Film cooling simulations

A 100×100 cells computational grid is employed for film cooling simulations. The latter is shown in Fig. 41. A cell clustering toward the upper wall is used over the whole chamber length to properly resolve the viscous sublayer, resulting in a non–dimensional wall distance $y^+ \approx 1$. On the other hand, in the axial direction, the domain is divided into three zones to reasonably resolve the main features of the flowfield, namely an injection, streamtube, and nozzle region. In

this regard, the first zone covers the first 100 mm of the combustion chamber starting from the left boundary, toward which cells are clustered to better capture the injection of the secondary flow. Furthermore, as shown in the inset of Fig. 41, a proper cell clustering is also introduced in the radial direction to sufficiently resolve the mixing layer and the recirculation region between the hot gas and film inflows. A uniform streamtube region is identified from the end of the injection zone until the nozzle entrance. Eventually, the nozzle region extends until the end of the thrust chamber. Cells are here clustered toward the throat to properly resolve the transition through sonic conditions and to manage the higher axial gradients. Smooth transitions between mesh regions are guaranteed by a suitable axial cell clustering, which allows to consider larger cells where the propellants are mixed and hence to reduce computational time.

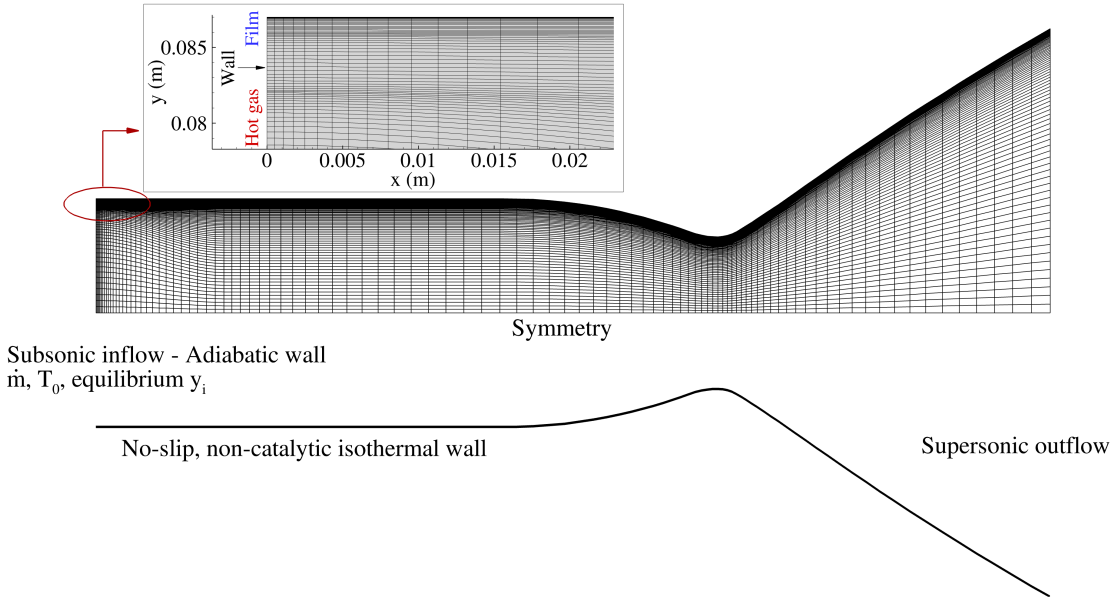

Figure 41: Computational grid with boundary conditions used in film cooling simulations. Details of inflow boundary conditions are shown in the inset.

As shown also in Fig. 37, adiabatic wall and subsonic inflows conditions are applied to the left boundary. Mass flow rate, total temperature, and mixture mass composition in terms of the species included in the chemical reaction mechanism are prescribed at the inlet boundaries. The CEA program [113] is used to compute T_0 and equilibrium mass fractions y_i at the design chamber pressure and mixture ratio assuming reactants in liquid phase. At the nominal conditions (see Sec. 5.2) a hot gas mass flow rate of 33.22 kg/s (6.56 kg/s fuel and 26.66 kg/s oxidizer), a film mass flow rate of 1.28 kg/s (~ 3.7% $\dot{m}$), a hot gas temperature of 3536 K, and a film temperature of 300 K are employed. Symmetry is enforced at the centerline. The upper wall is characterized by a no–slip, non–catalytic, and isothermal boundary condition. For the sake of simplicity, a wall temperature of 400 K has been arbitrarily selected as similar to that of the thrust chamber described in Chap. 4, and enforced on the upper wall. Such a

low wall temperature is not representative of a real LRE application, where the actual wall temperature is the result of the interaction between the hot gas side, the chamber wall, and the cooling channels. However, this choice has been made to make the two test chamber near–wall chemical reaction behaviours as comparable as possible. The outflow is supersonic.

Notice that the computational domain shown in Fig. 41 has been designed to simulate the nominal near–injector geometry chamber configuration. Minimal variations in the discretization of the near–injector region are made in the framework of the parametric analysis, when the film slot injection height or the separating wall thickness are changed. Nevertheless, the cell number and the grid topology are unchanged.

5.4.2 Mixture ratio bias simulations

The grid used for mixture ratio bias simulations is shown in Fig. 42, and it is similar to that employed in film cooling simulations. A further radial cell clustering is applied in the injection region due to the different geometrical configuration (see inset in Fig. 42) , whereas the axial discretization is unchanged from Sec. 5.4.1. The resulting grid is composed by 13400 volumes, 100 in the axial direction and 134 in the radial direction. Boundary conditions are the same as the film cooling ones as well, except for the injection plate where a further adiabatic wall (*Wall 2* in Fig. 42) is introduced up to the chamber wall.

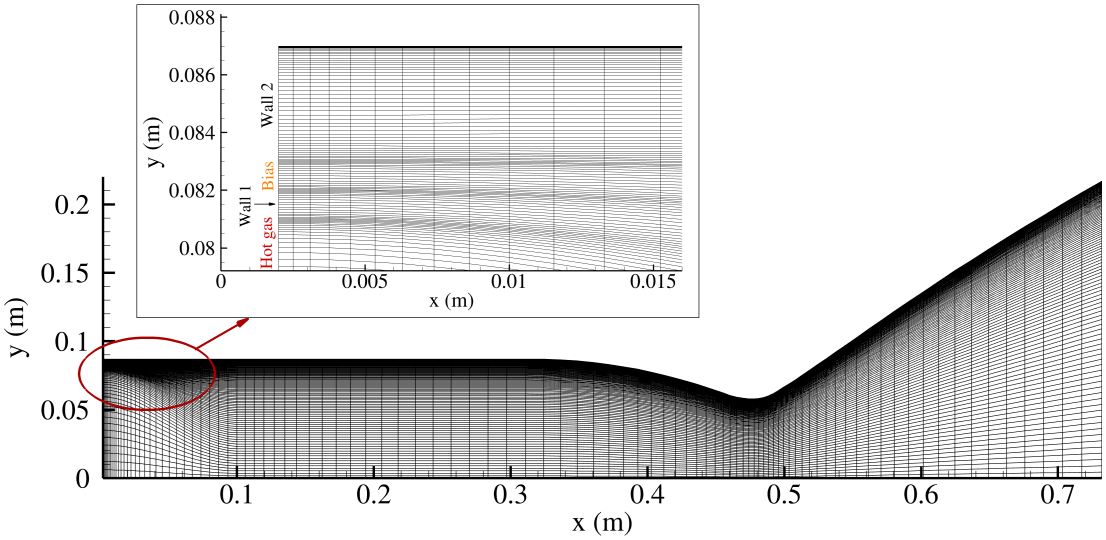

Figure 42: Computational grid used in mixture ratio bias simulations. Details of inflow boundary conditions are shown in the inset.

The same mesh has been retained to carry out numerical simulations over the whole peripheral flow mixture ratio range of investigation.

5.5 GRID CONVERGENCE ANALYSIS

As done in Sec. 4.4 for the API approach, two levels of grid refinement are considered to verify grid independence and evaluate the numerical error in case of film cooling and mixture ratio bias numerical simulations. Coarser levels are not considered in the two cases since a lower number of cells would not be sufficient to resolve the mixing layers between the hot gas and the secondary flow developing from the near–injector region. Similarly, a further finer grid level is not considered due to the excessive computational cost. The finer level is made of 200 cells in the axial direction and 200 cells in the radial direction for film cooling and 200 cells in the axial direction and 268 cells in the radial direction for mixture ratio bias. Such grids are obtained by doubling the number of cells in both axial and radial directions with respect to the coarse–level 100×100 and 100×134 grids shown in Sec. 5.4.1 and 5.4.2, respectively, therefore doubling the characteristic spatial discretization Δx. Appropriate resolution of the boundary layer physics is guaranteed by the maximum dimensionless wall distance, y^+, obtained at nozzle throat wall, which ranges between 1.2 and 0.5 for the above-mentioned grid levels.

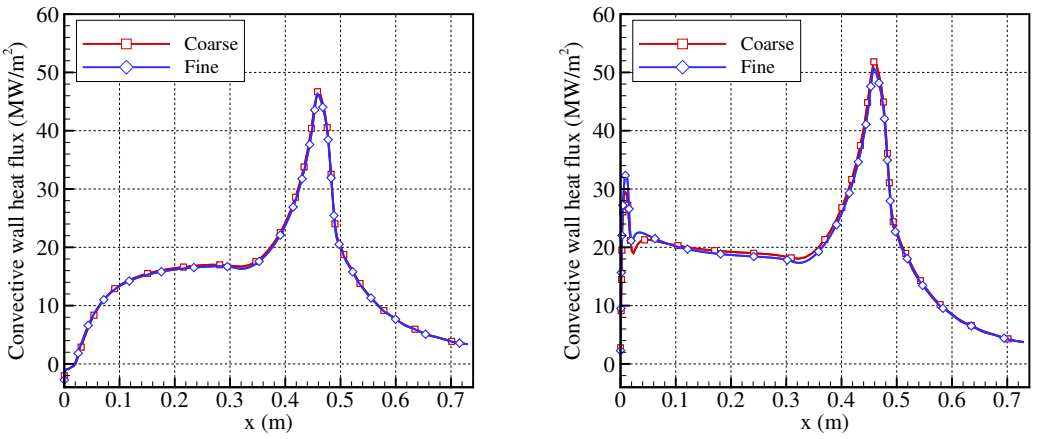

(a) Film cooling

(b) Mixture ratio bias

Figure 43: Grid convergence analysis on convective wall heat flux for film cooling and mixture ratio bias simulations.

To ensure such a wall resolution, in both cases a cell height at nozzle throat wall of 0.1 and 0.06 µm is used for coarse and fine grid levels, respectively. Two specific numerical simulations have been chosen to carry out the present grid convergence analysis, in particular the reference film cooling configuration, presented in the following (Sec. 5.6.1), and the mixture ratio bias simulation featuring a peripheral mixture ratio of 2.33. The latter has been chosen without any particular reason with respect to the others. Axial profiles of wall heat flux carried out by means of coarse and fine grid levels in the two cases are shown

in Figs. 43a and 43b. As shown in Table. 12, the convective wall heat flux at throat obtained with the coarse grid level differs from the value obtained with the fine grid of 0.36 MW/m^2 (0.8%) and 1.13 MW/m^2 (2.2%) in case of film cooling and mixture ratio bias simulations, respectively.

Table 12: Computational grids and convective throat wall heat flux values at throat used in the grid convergence analysis for film cooling and mixture ratio bias simulations.

	Film cooling		Mixture ratio bias	
Quantity	Grid 1	Grid 2	Grid 1	Grid 2
Number of cells	10000	40000	13400	53600
Throat heat flux, MW/m^2	46.69	46.33	51.82	50.69

As a result, due to the low discrepancies with respect to the finer levels, the coarse 100×100 and 100×134 grids are adopted to perform film cooling and mixture ratio bias simulations, respectively.

5.6 FILM COOLING ANALYSIS

The drawbacks yielded by film injection on engine performances may affect critically the engine design despite the beneficial effects obtained on the throat heat load. For this reason it is important to have numerical tools to carry out predictions of this twofold aspect in the design phase, with the possibility to perform several iterations before obtaining results of practical interest. As mentioned also for the CPI approach in Chap. 4, such a numerical tool should rely on a simple but effective formulation, capable to provide predictions with reasonable accuracy in reasonable times. In this section, a sensitivity analysis is performed on the throat wall heat flux reduction and performance loss in terms of the four parameters identifying the film cooling nominal operating condition described above, namely h_{slot}, t_{wall}, $B = (\rho u)_g / (\rho u)_{film}$, and T_{film}. Numerical correlations are eventually provided as a function of the observed most relevant quantities as effective and versatile numerical tools for film cooled LRE design.

5.6.1 Uncooled and nominal film cooling configurations

The temperature fields obtained under the nominal film cooling conditions and in case of the uncooled MFUS thrust chamber are shown in Fig. 44.

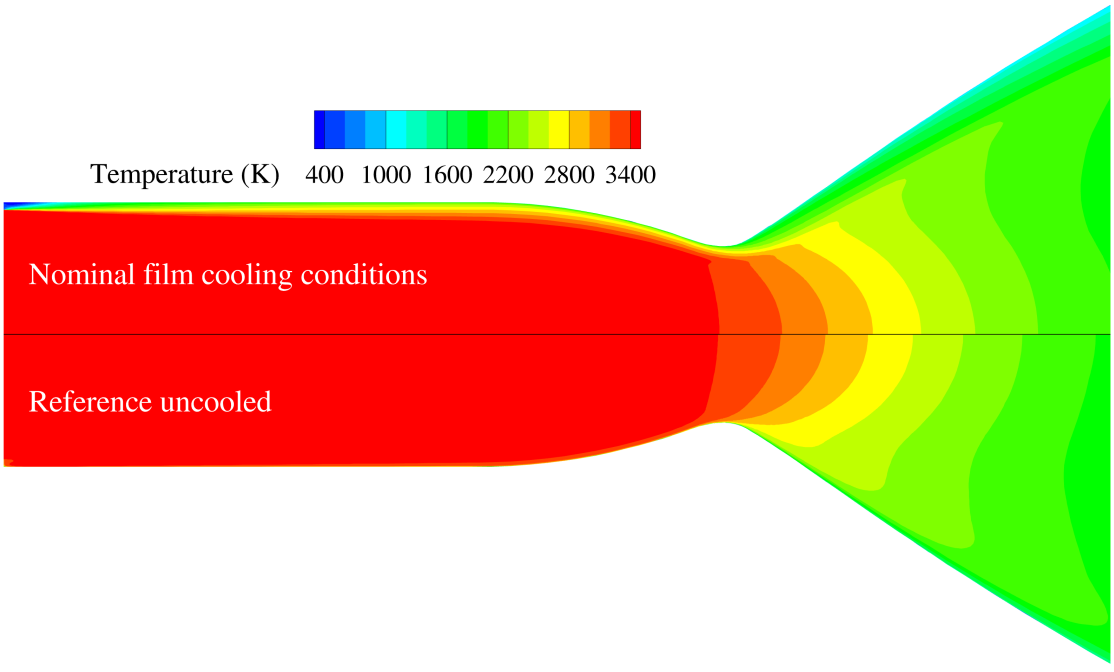

Figure 44: Comparison between the temperature fields obtained in case of nominal film cooling conditions and reference uncooled configuration.

The features of the uncooled thrust chamber flowfield are similar to that shown on the bottom of Fig. 26a. and in Fig. 32 regarding the CPI and CPI

w/BFS solutions, respectively. A weaker boundary layer development is observed in case of the MFUS chamber due to the much higher mass flow rate and chamber pressure, yielding a much higher abscissa–based Reynolds number and thus a much lower boundary layer thickness. On the other hand, the film cooled MFUS chamber is characterized by a clear temperature stratification in the vicinity of the wall. The ambient temperature film can be observed being injected right at the injection plate, fading slowly away downstream. In fact, the film starts mixing and reacting with the hot gas upon injection, yielding a fresh mixing layer close to the wall with a temperature of about 1500 K. Under the selected nominal operating conditions, the fresh mixture is capable to effectively reach the nozzle and, in particular, the throat region, where a clear difference with respect to the uncooled case can be observed.

The convective wall heat flux axial profiles obtained in the two cases are compared in Fig. 45.

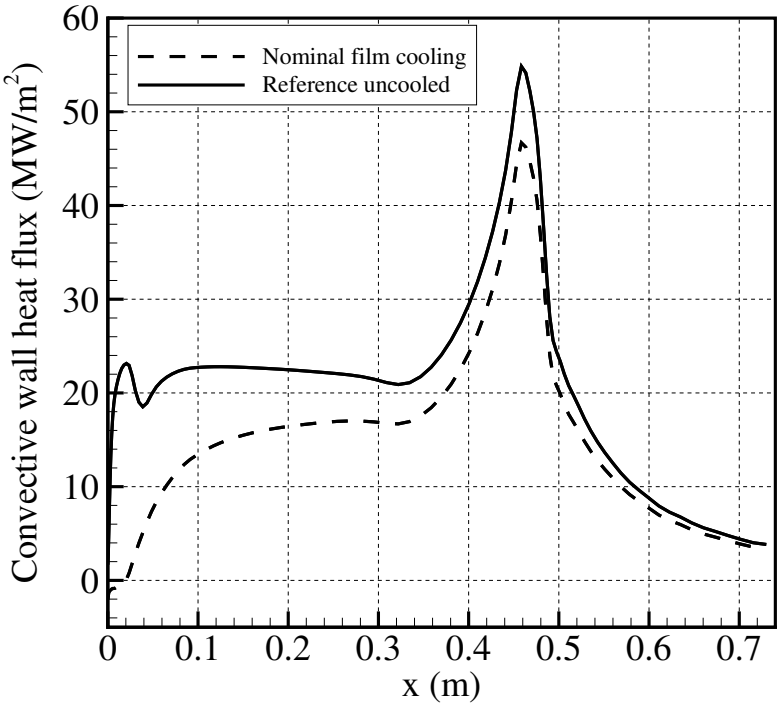

Figure 45: Comparison between the convective wall heat flux axial profiles obtained in case of nominal film cooling conditions and reference uncooled configuration.

After a sharp increase and a single oscillation due to the presence of the backward facing step–induced recirculation region, the uncooled MFUS chamber shows a slightly decreasing convective wall heat flux profile due to the weak boundary layer development. Then, a sharp increase is observed in the convergent part of the nozzle as expected, until a peak of 54.8 MW/m^2 and,

eventually, a decrease in the divergent part. Note that a vacuum specific impulse of 306 s has been calculated for the uncooled MFUS.
With regard to the wall heat flux, film injection produces beneficial effects over the whole combustion chamber. Negative values of convective wall heat flux are observed until $x = 20$ mm, that is until the ambient–temperature methane film core extends. Being the nominal film temperature (300 K) lower than the enforced wall temperature (400 K), the heat flux is directed inwards in such a region. A wall heat flux increase characterizes the rest of the combustion chamber until the nozzle due to the interaction between the film and the hot gas, leading to a progressive increase of the mixing layer temperature. A peak heat flux of 46.7 MW/m^2 occurs at the throat, i.e. nearly 15 % lower than the uncooled simulation. On the other hand, the vacuum specific impulse calculated for the film cooled MFUS thrust chamber is 297 s, hence involving a non–negligible performance loss of about 3 % due to the incomplete mixing and burning of the propellants. It is worth specifying that the vacuum specific impulse is calculated from the CFD solution as $F_{vac}/(\dot{m} g_0)$, where thrust in vacuum is obtained by integrating the momentum flux over the nozzle exit cross section:

$$F_{vac} = \int_{A_e} (\rho u^2 + p)\, dA \tag{142}$$

The choice to evaluate performances in terms of vacuum specific impulse is motivated by two reasons: (i) vacuum specific impulse does not require the calculation of chamber pressure, which should be evaluated arbitrarily according to a certain criterion (see Sec. 4.9 for instance); (ii) being the specific impulse the product between the characteristic velocity and the thrust coefficient, it accounts for different kinds of losses at the same time, i.e. divergence, friction, heat exchange, and incomplete mixing and combustion. The latter, in particular, represents a significant contribution to the performance reduction due to film cooling as will be shown later in the chapter.

5.6.2 Sensitivity analysis

The four investigated parameters are varied within the following ranges: $h_{slot} \in [0.75, 1.50]$ mm, $t_{wall} \in [5.00, 7.50]$ mm, $B \in [0.40, 0.83]$, and $T_{film} \in [200, 500]$ K. Blowing ratios, in particular, have been specifically chosen in such a way to provide film mass flow rates from 2 to 6 % of the total mass flow rate using the reference film injection slot height of 1 mm. Numerical simulations are performed varying one parameter at a time starting from the nominal operating conditions, retaining the superposition principle assumption.

Numerical results of the sensitivity analysis are shown in Fig. 46, where the throat wall heat flux reduction and the vacuum specific impulse loss are presented as a function of each parameter under investigation. For the sake of

clarity, the the throat wall heat flux reduction and the vacuum specific impulse loss are defined as follows:

$$\left.\frac{\Delta q_w}{q_{w,nofilm}}\right|_{th} = 1 - \left.\frac{q_{w,film}}{q_{w,nofilm}}\right|_{th} \tag{143}$$

$$\frac{\Delta I_{vac}}{I_{vac,nofilm}} = 1 - \frac{I_{vac,film}}{I_{vac,nofilm}} \tag{144}$$

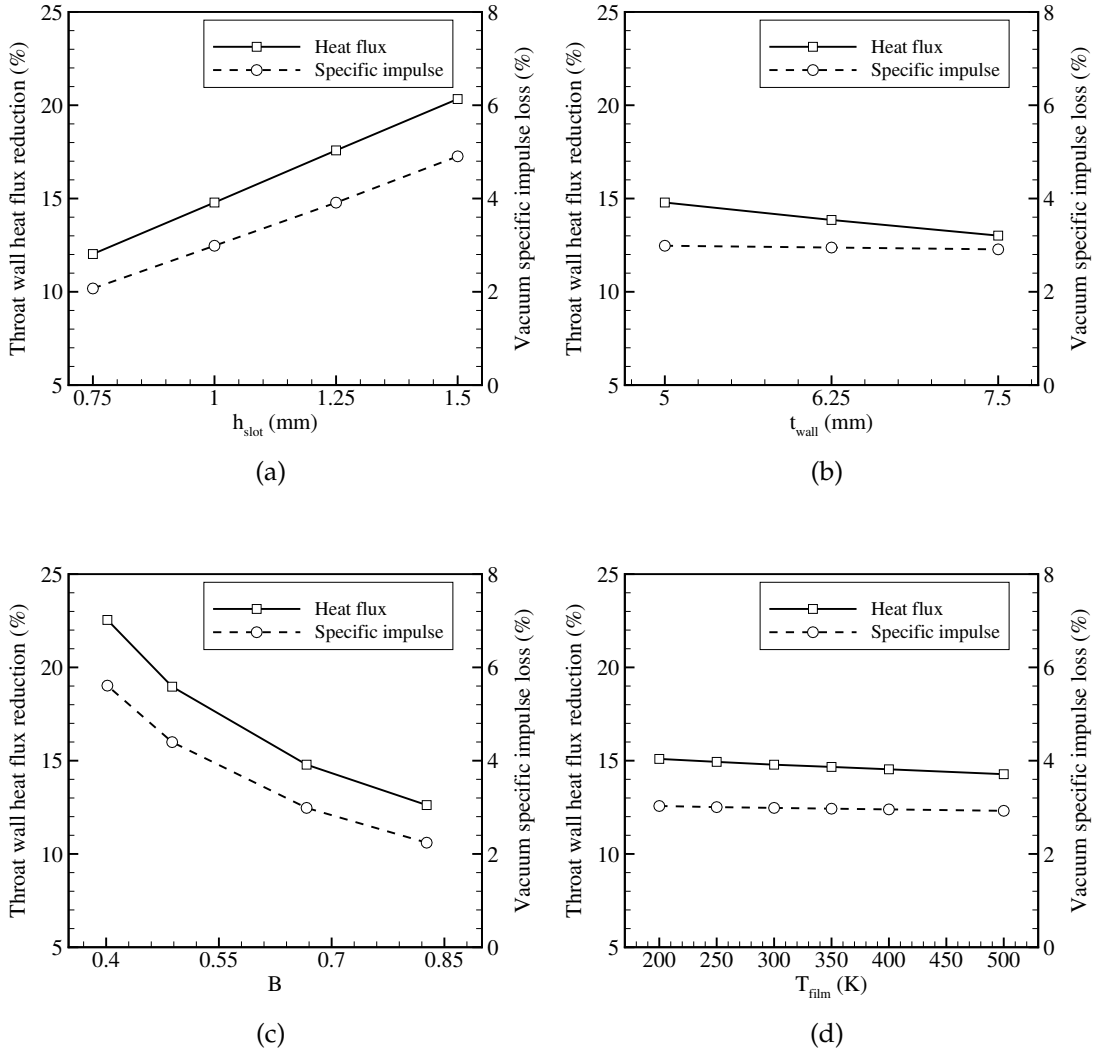

Figure 46: Numerical throat wall heat flux reduction and vacuum specific impulse loss with respect to the uncooled case as a function of the investigated parameters: (a) film injection slot height, (b) separating wall thickness, (c) blowing ratio, and (d) film injection temperature.

The separating wall thickness (Fig. 46b) and the film injection temperature (Fig. 46d) are the two parameters providing weaker effects on throat wall heat flux and vacuum specific impulse. It has been observed that such two parameters affect the flowfield mostly in the first half of the combustion chamber,

where mixing and reaction with the hot gas occur, without influencing significantly the throat region. An example is given in Fig. 47, where the effect of varying film injection temperature on the wall heat flux is observed to be significant only in the near–injector region, then vanishing downstream. Negative, zero, and positive wall heat flux is obtained close to the injector plate for film temperatures lower, equal, and greater than the enforced wall temperature of 400 K, respectively. A variation of almost 1 % is obtained on the throat wall heat flux reduction varying the film injection temperature over the whole range of investigation (see Fig. 46d), whereas a slightly higher variation of nearly 2 % is shown by varying the separating wall thickness (see Fig. 46b). Nevertheless, such a variation can be reasonably considered negligible if compared with the other results obtained for the other parameters described in the following. Variations of vacuum specific impulse loss are negligible in both cases, below 1 %.

On the other hand, major effects are observed to occur varying the film injection slot height (Fig. 46a) and the blowing ratio (Fig. 46c). A linear increase of the throat wall heat flux reduction is observed by increasing the film injection slot height, with a variation of 8 % across the whole range. The same happens for the vacuum specific impulse loss, which undergoes a variation around 3 %.

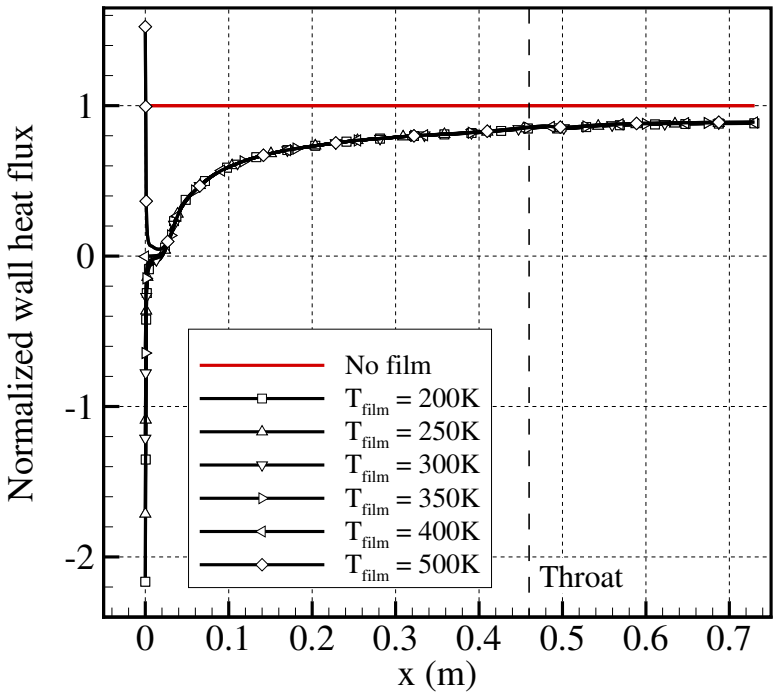

Figure 47: Axial wall heat flux for different values of film injection temperature. Results are normalized with the uncooled simulation results.

The more important role played by such a parameter is motivated by the greater influence it has on the film mass flow rate, as shown by the solution of the sys-

tem of equations in Eq. (131). In fact, a higher slot height yields a higher film injection area which, in turn, leads to a lower hot gas mass flux (Eq. (133)). Accordingly, being the blowing ratio constant, a lower film mass flux is obtained (Eq. (134)). Nevertheless, a net increase is observed as a result on the film mass flow rate (Eq. (135)), showing that the effect of the injection area increase is predominant on the decrease of the film mass flux. As a consequence of the higher coolant flow, chamber pressure is observed to decrease with increasing film mass flow rate, leading to the non–negligible vacuum specific impulse losses shown in Fig. 46a.

The blowing ratio is observed to be the most influential parameter in this analysis, providing a quadratic decrease of both throat wall heat flux reduction and vacuum specific impulse loss, with a variation of about 10 and 3.5 %, respectively. According to the solution of the system of equations shown in Eq. (131), increasing blowing ratios inevitably correspond to decreasing film mass flow rates, hence providing progressively lower cooling capabilities and performance losses.

Numerical results presented so far have shown that the throat wall heat flux reduction and the vacuum specific impulse loss show higher sensitivity to the blowing ratio and the film injection slot height. For this reason, the effects yielded by variations of separating wall thickness and film injection temperature are hereafter neglected. It has been also pointed out that both parameters significantly affect the film mass flow rate according to the mass flow rate splitting procedure shown in Sec. 5.3.

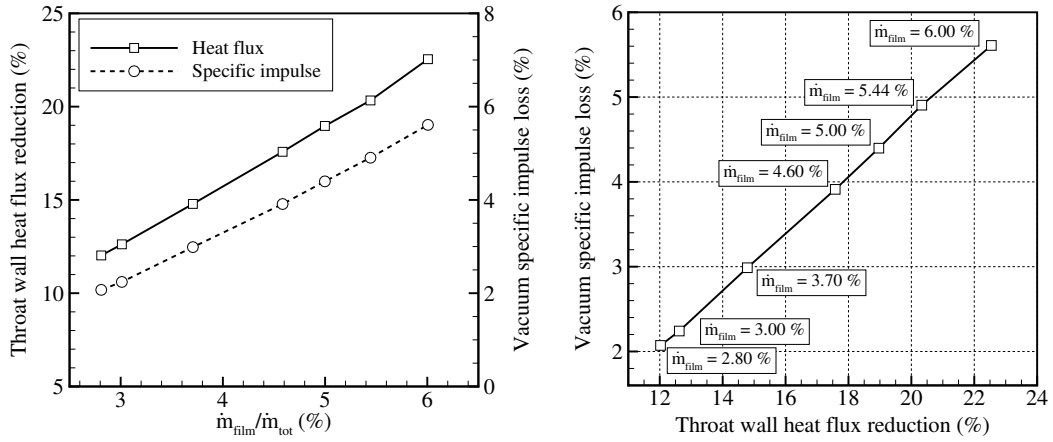

Figure 48: Numerical results as a function of film mass flow rate percentage.

For this reason, the film mass flow rate, suitably calculated according to each configuration, can be retained to reduce all the most significant numerical results (Figs. 46a and 46c) as a function of a single parameter. As a result,

Fig. 48a shows the throat wall heat flux reduction and the vacuum specific impulse loss as a function of the film mass flow rate percentage with respect to the total mass flow rate $\dot{m}_{tot}$. As mentioned above, the latter correspond to the 7 combinations of blowing ratio and film injection slot height investigated so far. As expected, high film mass flow rates yield high throat wall heat flux reductions at the expense of engine performances, showing a linear proportionality between them (Fig. 48b).

5.6.3 Throat wall heat flux and performance reduction numerical correlations

On the basis of the interesting and encouraging results obtained from the sensitivity analysis, the dependency of the throat wall heat flux reduction and vacuum specific impulse loss on the film mass flow rate is further investigated in the following to eventually provide two numerical correlations accounting for a comprehensive range of operating conditions. For this purpose, 9 new numerical simulations are performed considering all the possible combinations between the blowing ratios and film injection slot heights investigated in Sec. 5.6.2. The film mass flow rates corresponding to the latter are shown in Table. 13.

Table 13: Film mass flow rate percentages obtained with all the possible combinations of the investigated blowing ratios and film injection slot heights.

	$B = 0.4$	$B = 0.49$	$B = 0.66$	$B = 0.82$
$h = 0.75$ mm	4.58	3.80	2.81	2.28
$h = 1.00$ mm	6.00	5.00	3.40	3.00
$h = 1.25$ mm	7.39	6.16	4.26	3.73
$h = 1.50$ mm	8.72	7.29	5.44	4.44

Note that 7 of the 16 combinations (second row and third column in Table. 13) have been already presented in Figs. 46a and 46c. It should be observed also that all the operating conditions considered in Table 13 correspond to film–driven configurations, i.e. with blowing ratios lower than 1. For the sake of completeness, the film mass flow rate range of investigation is further extended by considering operating conditions yielding core–driven configurations ($B > 1$), and unitary blowing ratio, as well. The latter are achieved by keeping the film injection slot height unchanged to the lower value considered in Table 13, which is 0.75 mm, and progressively increasing the blowing ratio until a maximum value of 10. The uncooled configuration is also indicated as theoretically corresponding to $B \to \infty$. All the new operating conditions with the resulting film mass flow rate percentages are shown in Table 14.

Table 14: Film mass flow rate percentages corresponding to core–driven and unitary blowing ratio configurations with $h_{slot} = 0.75$ mm.

B	1.00	1.33	2.00	4.00	10.00	∞
$\dot{m}_{film}/\dot{m}_{tot}$ (%)	1.89	1.42	0.95	0.48	0.19	0.00

The throat wall heat flux reduction obtained for all the combinations of blowing ratio and slot height as a function of the film mass flow rate percentage is shown in Fig. 49a, whereas the vacuum specific impulse loss is shown in Fig. 49b. Film–driven, unitary blowing ratio, and core–driven regimes are distinguished by means of different symbols and colors.

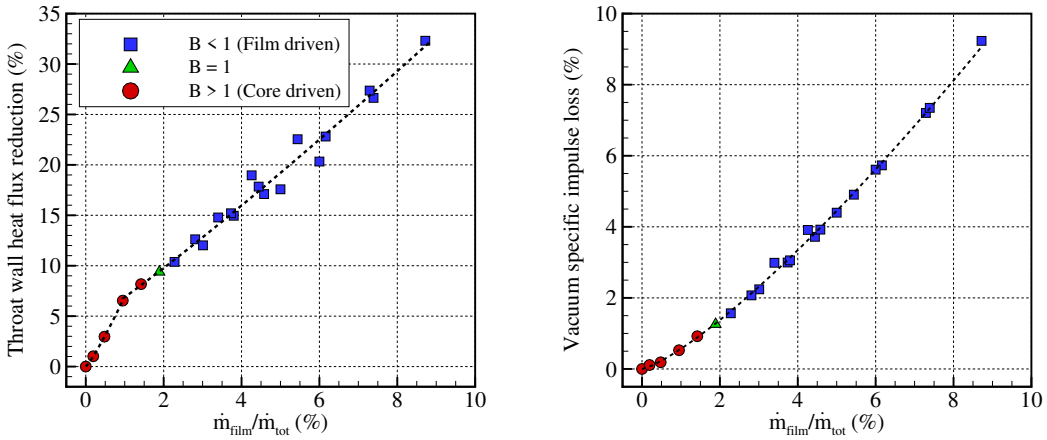

(a) (b)

Figure 49: Throat wall heat flux reduction and vacuum specific impulse loss as a function of the film mass flow rate percentage. Dashed lines correspond to Eq. (145) (subFig. a) and Eq. (146) (subFig. b).

The throat wall heat flux reduction and vacuum specific impulse loss are both well described by the correlation laws shown in Eqs (145) and (146), and represented as dashed lines in Figs. 49a and 49b.

$$\left.\frac{\Delta q_w}{q_{w,nofilm}}\right|_{th} = \begin{cases} 0.0694\left(\dfrac{\dot{m}_{film}}{\dot{m}_{tot}}\right)^{1.16} & \text{if } \dfrac{\dot{m}_{film}}{\dot{m}_{tot}} \leqslant 0.0095 \\ 0.0436 + 0.0251\left(\dfrac{\dot{m}_{film}}{\dot{m}_{tot}}\right)^{1.1} & \text{otherwise} \end{cases} \tag{145}$$

$$\frac{\Delta I_{vac}}{I_{vac,nofilm}} = 0.00568\left(\frac{\dot{m}_{film}}{\dot{m}_{tot}}\right)^{1.28} \tag{146}$$

A power law with a film mass flow rate percentage exponent of 1.16 is found to provide the best interpolation of throat wall heat flux reduction numerical

results at low film mass flow rate percentages until the value of 0.0095, whereas the rest of the data are well represented by a nearly–linear regression law featuring an exponent of 1.1. On the other hand, a power law with an exponent of 1.28 is obtained for the vacuum specific impulse loss. A clear relationship can be established also for the throat wall heat flux reduction as a function of the vacuum specific impulse loss, which is well described by the following correlation law for all the investigated film mass flow rates:

$$\left.\frac{\Delta q_w}{q_{w,nofilm}}\right|_{th} = 1.43 \left(\frac{\Delta I_{vac}}{I_{vac,nofilm}}\right)^{0.64} \tag{147}$$

The fitting procedure showed a goodness (R^2) between 98 and 100 % in the three cases. It is worth to recall that the two regression laws are valid for film mass flow rates percentages in the range $[0, 8.72]$ %, obtained as a combination of blowing ratios and film injection slot heights in the range $[0.4, 10.00]$ and $[0.75, 1.50]$ mm, respectively.

As far as the throat wall heat flux reduction is concerned, film–driven data are slightly scattered among each other but following an overall increasing trend with film mass flow rate as previously observed in Fig. 48a. Data scattering occurs since each film mass flow rate under investigation is the result of a specific pair of blowing ratio and film injection slot height, which produce two independent effects on the resulting flowfield. No appreciable scattering is shown by unitary blowing ratio and core–driven numerical results since the slot height is not varied in the simulations. Throat wall heat flux reduction is observed to increase with a different slope for low film mass flow rates, until a value of about 0.95 %. In this range, the throat wall heat flux reduction appears to be more sensitive to a variation of film mass flow rate with respect to higher film amounts. That may occur due to the effects produced locally at the throat wall by the different film mass flow rates. As shown by radial profiles of temperature taken at the throat abscissa in Fig. 50a, film injection always produces a temperature decrease in the throat near–wall region. The higher sensitivity shown by the throat wall heat flux reduction to low film mass flow rates can be appreciated by comparing the different temperature profiles. This explains the increasing monotonic behaviour shown in Fig. 48a. The different slope provided by core–driven numerical results at low film mass flow can be justified by the local chemical composition yielded at the throat wall by mixing and reaction of the hot gas with the coolant methane. In this regard, Figs. 50b–f show radial profiles of propellants and main combustion products taken at the throat abscissa. Firstly, 1.5 % of residual methane is observed at the throat wall for a film mass flow rate percentage of 1.42 %, as shown in Fig. 50b. Methane mass fraction increases to 3.3 % in case of a film mass flow rate percentage of 1.89 %, showing a nearly–constant rate of change. No methane is observed at throat for numerical solutions with lower film amounts (including the uncooled case of course), since methane is completely mixed upon injection with the hot gas.

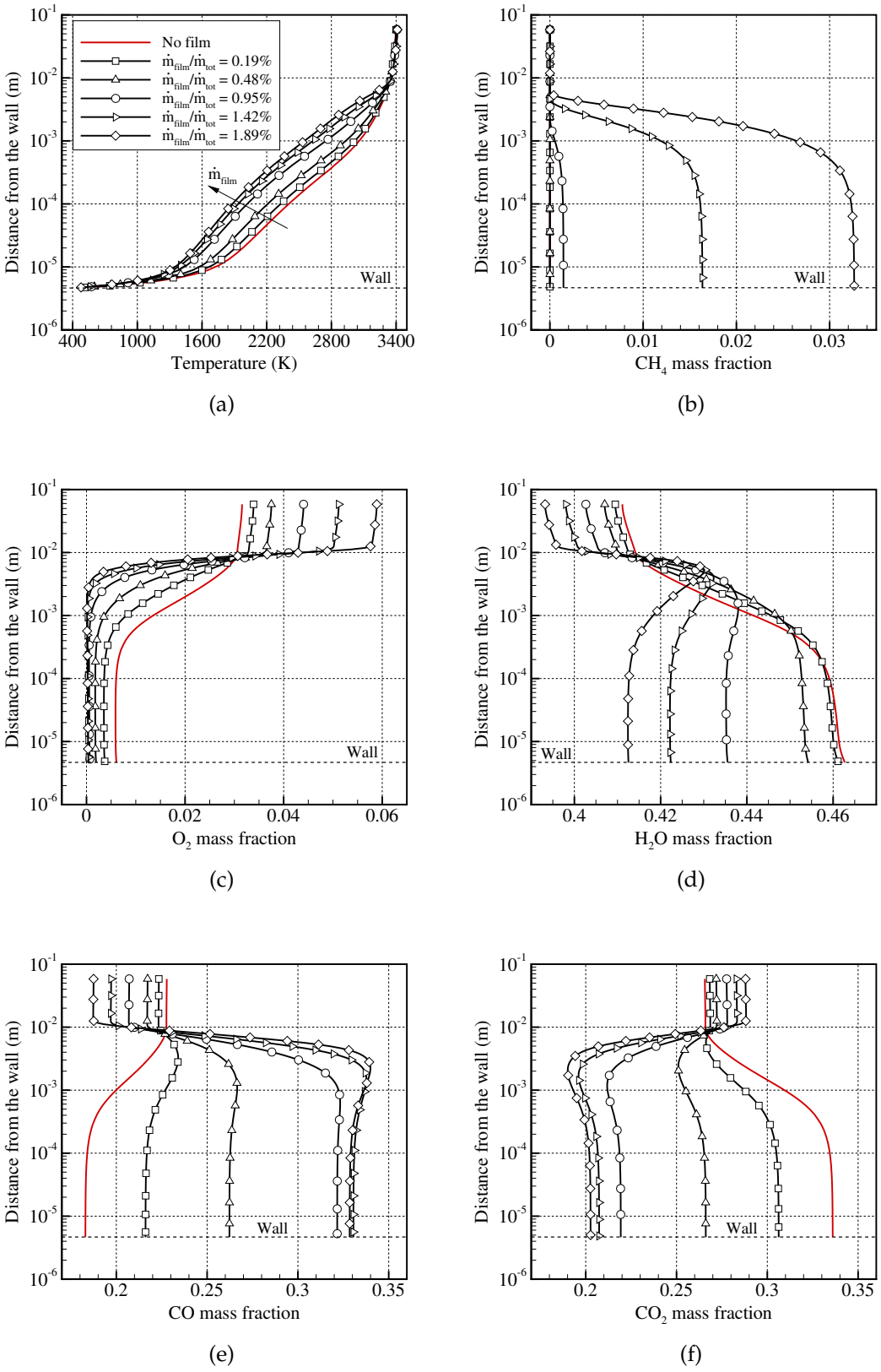

Figure 50: Radial profiles of temperature (a) and species mass fraction (b–f) at throat abscissa for different mass flow rate percentages.

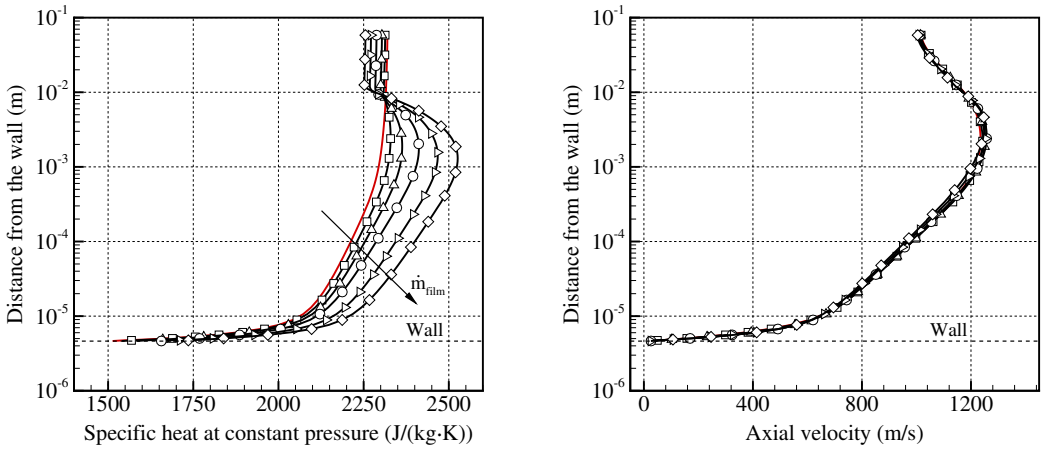

Figure 51: Radial profiles of specific heat at constant pressure (a) and axial velocity (b) at throat abscissa for different mass flow rate percentages.

On the other hand, the oxygen mass composition at the throat wall (Fig. 50c) decreases with increasing film mass flow rate until depletion, although in a very narrow range. Quite complex behaviour is shown by the main combustion products (H_2O, CO, and CO_2) in the boundary layer, which is observed to extend and produce major effects on the flowfield just within the last centimeter before the chamber wall. Overall, a depletion of recombined species (Figs. 50d and 50e) and a production of carbon oxide (Fig. 50f) are observed in the boundary layer for increasing film mass flow rate. As a result, different mixture thermophysical properties are obtained in the boundary layer at the throat abscissa, as shown for the specific heat at constant pressure in Fig. 51a. The specific heat at constant pressure has been observed to be the predominant term in the calculation of the mixture turbulent thermal conductivity (Eq. (3)). In particular, under the assumption of constant turbulent Prandtl number (0.9), the turbulent thermal conductivity has been found to be up to three orders of magnitude higher than the laminar contribution. No significant variations are observed on axial velocity profiles (see Fig. 51b) at such low film mass flow rates, concluding that the behaviour of the wall heat flux shown in Fig. 48a should be owed only to aspects related to chemistry. In addition to the considerations regarding the throat, different features are observed also in the near–injector region for varying film mass flow rates. As shown on the top of Fig. 52, a wide recirculation zone is observed to occur at the top–left corner of the combustion chamber due to the clear predominance of the hot gas momentum on the film flow at the very low film mass flow rate percentage of 0.48 %. The vortex is observed to move downstream and to gradually flatten toward the upper wall as the film mass flow rate is increased, until vanishing starting from a film mass flow rate of 3 %.

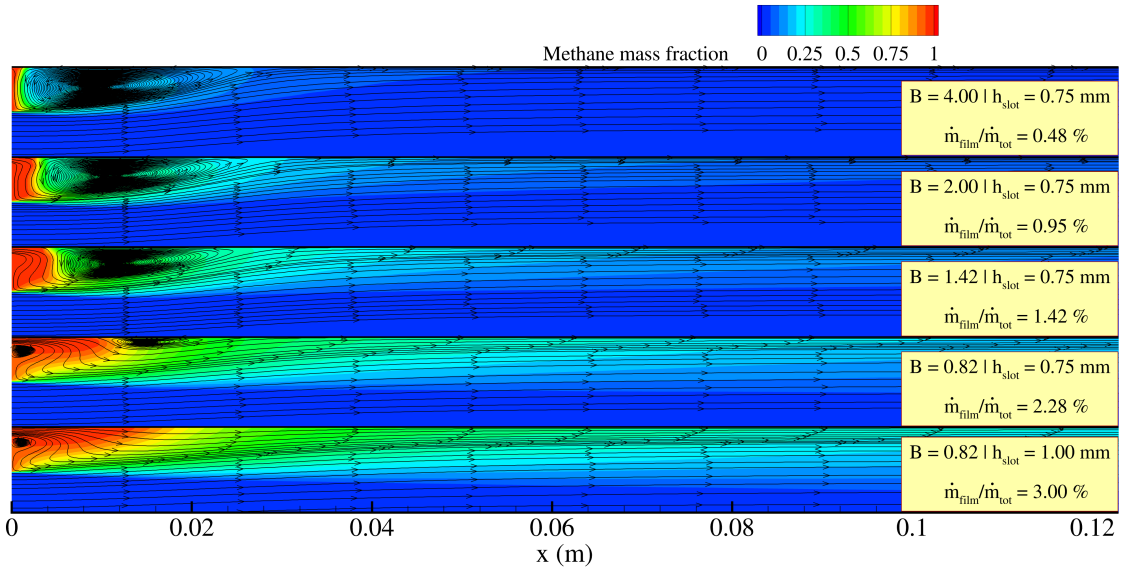

Figure 52: Flow structures produced upon film injection at different mass flow rates.

As far as the vacuum specific impulse loss is concerned (see Fig. 48b), numerical results show a well–defined functional dependence on the film mass flow rate. It is important to notice that the specific impulse is an integral quantity, hence it is not affected by the local effects occurring at the throat wall.

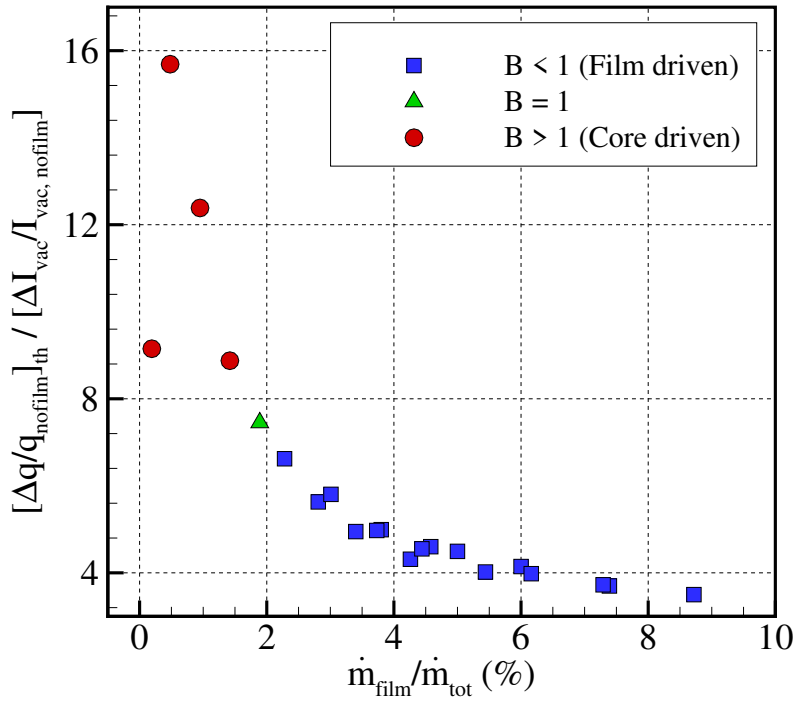

Figure 53: Ratio between the throat wall heat flux reduction and vacuum specific impulse loss as a function of the film mass flow rate percentage.

Moreover, the different behaviours characterized by the two slopes shown by the throat wall heat flux reduction numerical results in Fig. 49b are not observed. Increasing vacuum specific impulse losses with film mass flow rate are mainly due to the increasing characteristic velocity reduction yielded by incomplete mixing and combustion of the cooling methane with the hot gas. In this regard, it has been observed that, by computing the c^* and c_F from the numerical solutions featuring film mass flow rates percentages greater than 4 %, the characteristic velocity reduction represents 95 % of the vacuum specific impulse loss. Therefore, the regression law shown in Eq. (146) may be used also to carry out acceptable predictions of characteristic velocity losses for the mentioned mass flow rate percentages within 5 % error.

Table 15: Summary of film cooling numerical results obtained varying blowing ratio and film injection slot height in the range [0.4, 10.00] and [0.75,1.50] mm, respectively.

$\dot{m}_{film}/\dot{m}_{tot}$ (%)	B	h_{slot} (mm)	$\frac{\Delta q_w}{q_{w,nofilm}}\Big\vert_{th}$ (%)	$\frac{\Delta I_{vac}}{I_{vac,nofilm}}$ (%)
0.0	∞	0.00	0	0
0.19	10.00	0.75	1.02	0.11
0.48	4.00	0.75	2.97	0.19
0.95	2.00	0.75	6.54	0.53
1.42	1.33	0.75	8.17	0.92
1.89	1.00	0.75	9.38	1.26
2.28	0.82	0.75	10.38	1.57
2.81	0.66	0.75	12.61	2.07
3.00	0.82	1.00	12.02	2.24
3.40	0.66	1.00	14.78	2.99
3.73	0.82	1.25	15.19	3.00
3.80	0.49	0.75	14.95	3.05
4.26	0.66	1.25	18.96	3.91
4.44	0.82	1.50	17.84	3.72
4.58	0.40	0.75	17.11	3.92
5.00	0.49	1.00	17.58	4.40
5.44	0.66	1.50	22.54	4.90
6.00	0.40	1.00	20.33	5.61
6.16	0.49	1.25	22.81	5.73
7.29	0.49	1.50	27.37	7.20
7.39	0.40	1.25	26.64	7.35
8.72	0.40	1.50	32.31	9.23

It is interesting to notice that, as far as the ratio between the throat wall heat flux reduction and the vacuum specific impulse loss is concerned, the film mass flow rate percentage of 0.48 % might represent an optimal solution in the framework of the thrust chamber design. In fact, as shown in Fig. 53, the

very low film mass flow rate range is capable to provide good trade–off design solutions, where the reduction of the throat wall heat flux is predominant with respect to the vacuum specific impulse loss. A peak is observed at a film mass flow rate percentage of 0.48 %, after which the ratio between the two quantities lowers to approximately 4 in the range [4.00, 8.72] %.

To conclude this section, all the presented numerical results concerning film cooling simulations are summarized in Table 15.

5.7 MIXTURE RATIO BIAS ANALYSIS

As done for film cooling simulations analyzing the throat wall heat flux and vacuum specific impulse on the basis of the main design parameters, in this section the effects of mixture ratio biased peripheral injectors on the same quantities is investigated. The configuration shown in Fig. 38 has been employed to carry out numerical simulations in the framework of a parametric analysis. In this regard, the peripheral flow mixture ratio is retained as the only varying parameter, in the range [0.11,39.00]. Accordingly, the near–injector geometry and the blowing ratio are kept unchanged. Numerical simulations have been initially performed by means of the JL–R global reaction mechanism, and then compared to other chemical kinetics, such as frozen flow to highlight the role of chemical reactions on the quantities of interest. Moreover, the TSR–CDF–13 skeletal reaction mechanism, described in detail in sec. 2.1, is considered as a further term of comparison for the JL–R to evaluate the suitability of such a global mechanism in the framework of this analysis, especially when operating conditions far from the reference are considered.

5.7.1 Reference configuration

A reference configuration is identified also in case of mixture ratio bias simulations to observe how the throat wall heat flux and vacuum specific impulse behave varying the peripheral mixture ratio. As already mentioned in the chapter, the reference uncooled simulation performed in case of film cooling, where the secondary inflow is replaced with an adiabatic wall, is no longer considered appropriate since it is not representative of the geometry under investigation in this part of the work. For this reason, a different reference setup has been considered. In particular, the peripheral flow and the hot gas are injected in the combustion chamber with the same mixture ratio of 3.4, i.e. the design global mixture ratio. Therefore, both flows enter the chamber with a temperature of 3531 K. The temperature field corresponding to the reference configuration is shown in Fig. 54, with an inset providing the details of the near–injector region. The JL–R reaction mechanism has been employed to carry out the numerical simulation. Note that, even if not shown, the reference configuration has been simulated employing the other chemical kinetics too. Such results will be exploited later in the parametric analysis, when the different chemical models are compared. A uniform temperature field is observed along the whole combustion chamber due to the same injection conditions of the two inflows. Nevertheless, the streamlines shown in the inset on the top of Fig. 54 allow to identify some flow structures characterizing the flowfield in the near–injector region. A wide recirculation zone is observed on the top–left corner of the combustion chamber, induced by the presence of the walls and the peripheral flow. Accordingly, the peripheral flow develops below reaching the wall region, reattaching downstream of the wide vortex.

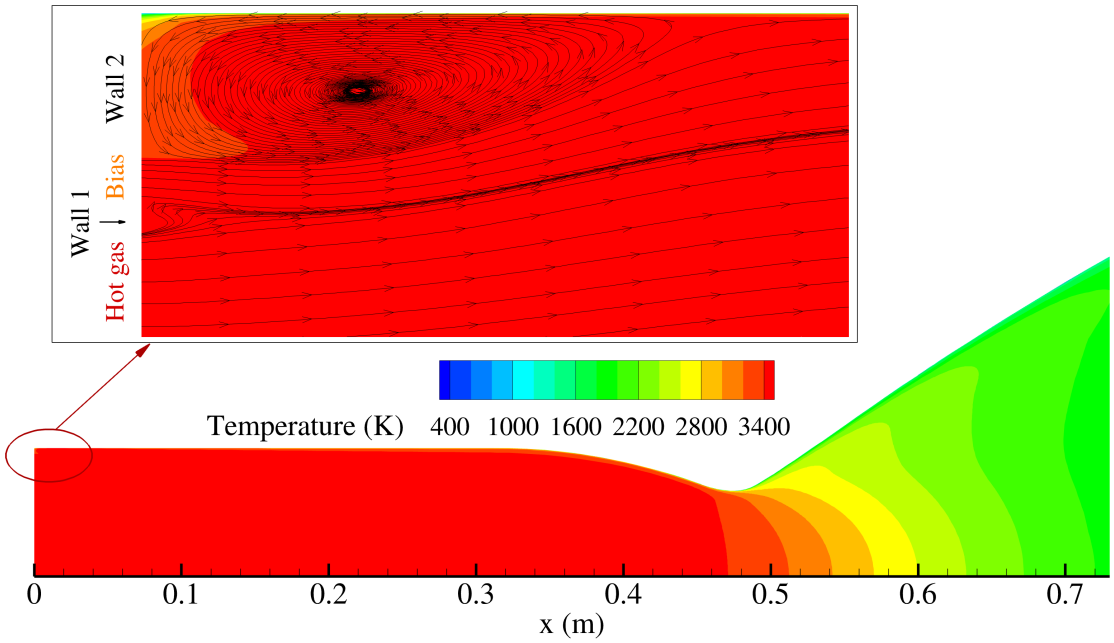

Figure 54: Temperature field obtained for the mixture ratio bias reference configuration. Details of flows injection are shown in the inset.

A small zone of interaction between the peripheral flow and the hot gas is then observed in correspondence of the separating wall (*Wall 1* in Fig. 54). The hot gas flow dominates the rest of the combustion chamber.

The axial wall heat flux profile does not show particular features with respect to those shown in Fig. 45 for the uncooled reference numerical solution. However, it is worth specifying that a peak wall heat flux of 54 MW/m^2 and a vacuum specific impulse of 306 s are obtained.

5.7.2 Peripheral mixture ratio parametric analysis

Throat wall heat flux and vacuum specific impulse numerical results obtained by means of the JL–R reaction mechanism are shown in Fig. 55. The latter are normalized with respect to the reference numerical solution (see Sec. 5.7.1). The peripheral equivalence ratio ϕ_{bias} has been considered more appropriate than mixture ratio to observe how such numerical results change with respect to the reference case, which is close to stoichiometric conditions. The peripheral equivalence ratio is calculated as:

$$\phi_{bias} = \frac{O/F_{st}}{O/F_{bias}} \tag{148}$$

where O/F_{bias} is obtained from Table 11 and $O/F_{st} \approx 4$. Being the investigated peripheral mixture ratios between 0.11 and 39, numerical results are represented for peripheral equivalence ratios in the range [0.10, 36.40].

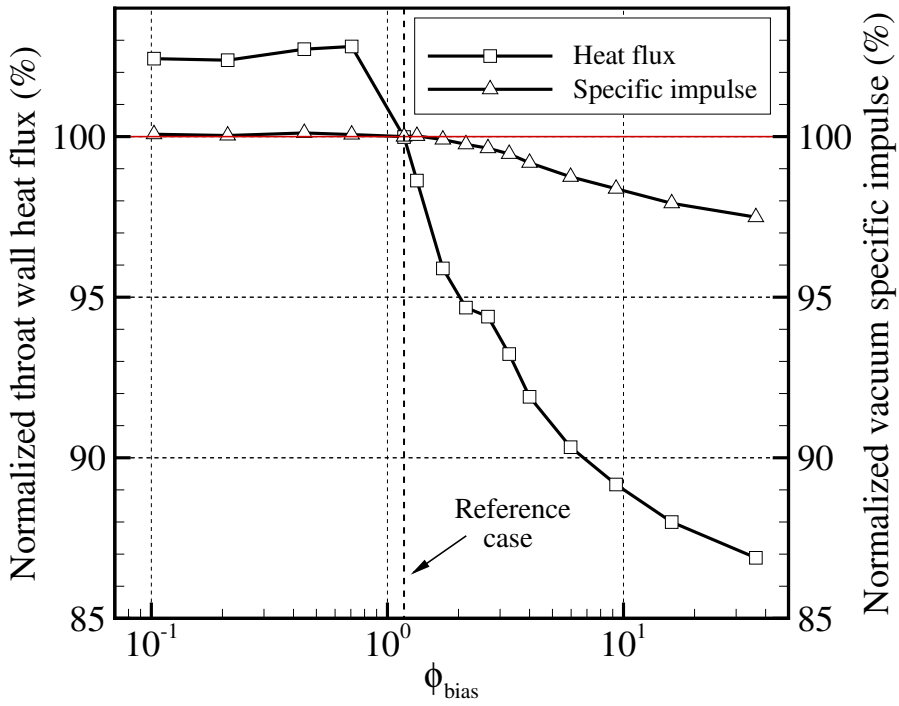

Figure 55: Throat wall heat flux and vacuum specific impulse obtained at different peripheral equivalence ratios using the JL–R reaction mechanism. Results are normalized with those obtained at the reference case.

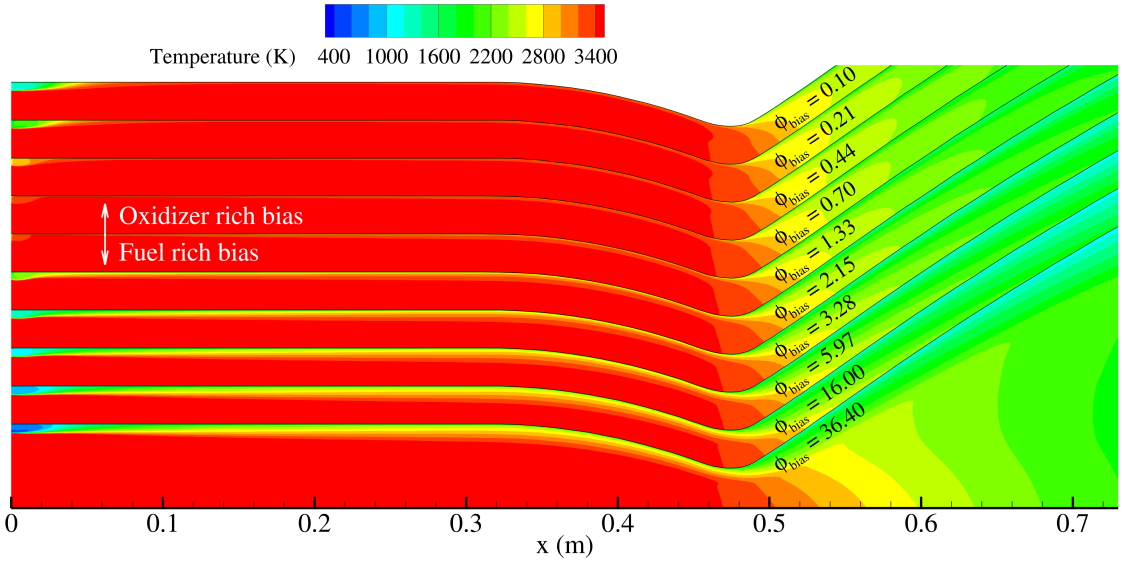

Figure 56: Temperature fields obtained at different peripheral flow equivalence ratios for the mixture ratio bias configurations. Simulations are performed employing the JL–R reaction mechanism.

A variation ranging from +3 % to -13 % of the reference numerical solution is observed on the throat wall heat flux. As expected, fuel–rich conditions

($\phi_{bias} > 1$) effectively yield an improvement on the throat heat flux, which shows a monotonic decrease with increasing equivalence ratio. Accordingly, vacuum specific impulse decreases as also shown for film cooling calculations, reaching a maximum reduction of about 2.5 %. On the other hand, an increase of the throat wall heat flux is observed in the oxidizer–rich region ($\phi_{bias} < 1$), with negligible vacuum specific impulse variations. Relying on the well–known role of chemical recombination reactions on wall heat flux in oxygen–methane LRE thrust chambers, such a result suggests that chemistry may have a significant impact on the evaluation.

Furthermore, temperature fields are shown in Fig. 56 for different values of the peripheral equivalence ratio. Different behaviours can be observed under oxidizer and fuel–rich conditions. In the former, the oxidizer–rich peripheral flow gets quickly mixed with the hot gas, producing a hot layer of carbon dioxide due to the intense chemical activity. Actually, no temperature reduction is observed in the near–wall throat region, in agreement with the high heat fluxes shown in Fig. 55. Due to the oxidizing high–temperature environment yielded close to the chamber wall by the peripheral flow, oxidizer–rich mixture ratio bias applications are generally not recommended. The near–injector mixing process becomes weaker as the peripheral mixture ratio approaches the stoichiometric conditions, being the two injection temperatures and chemical compositions very similar. On the other hand, a fresh mixing layer is observed to develop under fuel–rich conditions. The peripheral injection temperature decreases with increasing equivalence ratio due to the different equilibrium conditions calculated by the CEA program. Accordingly, the mixing layer thickness increases monotonically, reaching in all the cases the throat region and yielding an effective wall heat flux reduction (see Fig. 55).

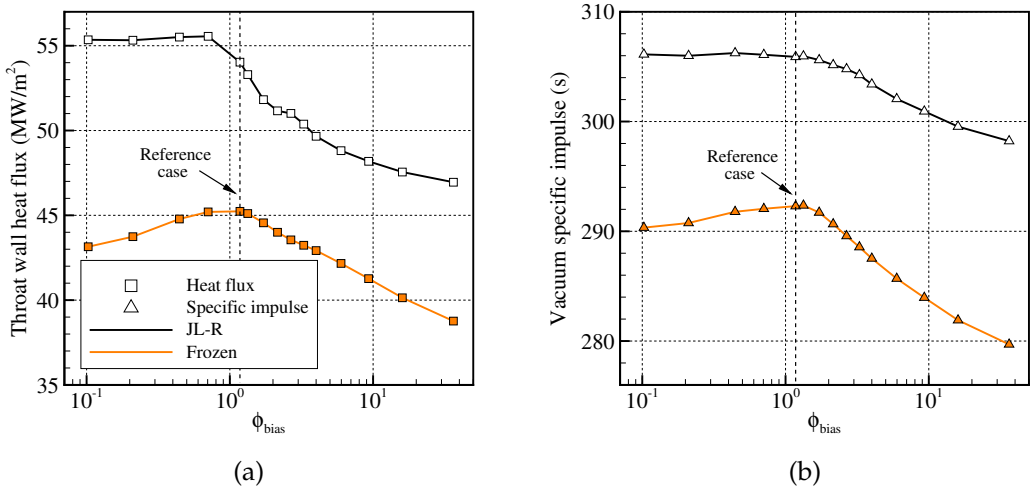

Figure 57: Comparison between throat wall heat flux and vacuum specific impulse obtained at different peripheral equivalence ratios using the JL–R reaction mechanism and frozen chemistry.

Important information about the behaviour of the throat wall heat flux and vacuum specific impulse can be obtained by comparing JL–R finite–rate results with frozen chemistry. The comparison of the throat wall heat fluxes and vacuum specific impulses obtained by means of the two chemical kinetics is shown in Fig. 57, highlighting the differences yielded by the flow reacting behaviour. Results are initially presented in absolute value to evaluate the quantitative differences between the two chemical models, whereas qualitative behaviours are illustrated in the following. As expected, frozen calculations provide significantly lower throat wall heat fluxes than those obtained employing the JL–R reaction mechanism, with an average discrepancy of -15 %. Moreover, a reduction rather than an increase of throat wall heat flux is shown in the oxidizer–rich region in case of frozen chemistry due to the progressively lower equilibrium temperature yielded by decreasing equivalence ratios. Being chemical reactions not modeled, propellants are not capable to release their chemical energy, which represents a significant contribution to the wall heat flux. This phenomenon acquires significant importance under oxidizer–rich conditions, when a high amount of oxygen is available for the production of recombined species as carbon dioxide. In this regard, a higher carbon dioxide mass fraction of up to 86 % is observed locally at the throat wall in case of JL–R oxidizer–rich results with respect to frozen chemistry. Therefore, it is reasonable to attribute the throat wall heat flux increase observed in Fig. 55 employing the JL–R kinetics at low equivalence ratios to the additional heat released by chemical recombination reactions. Similarly, frozen vacuum specific impulse is overall observed to be lower than JL–R finite–rate chemistry numerical results, with an average discrepancy of -5 %. The latter is mainly justified by the significant amount of losses yielded by the incomplete mixing and reaction of the peripheral flow with the hot gas. In this regard, Fig. 58 shows the chamber pressure calculated in case of the different chemical kinetics using Eq. (126). Note that, being mass flow rate enforced at the left boundary, the behaviour shown by chamber pressure and characteristic velocity is the same. As expected from vacuum specific impulse numerical results, frozen chamber pressure is lower than the JL–R over the whole range of peripheral equivalence ratios, with an average discrepancy of -2 %. It may be interesting to compare such results also to the ideal equilibrium calculations performed by means of the CEA program. A discrepancy slightly higher than 2 % is obtained on the characteristic velocity comparing the ideal frozen case to ideal equilibrium conditions employing CEA, indicating that the JL–R global reaction mechanism is promoting chemical recombination activity, providing results close to chemical equilibrium. However, a discrepancy of 6 % is obtained on vacuum specific impulse, slightly higher than that obtained by means of numerical simulations (5 %). In this regard, it should be noted that the nozzle geometry features an area ratio of 14, yielding a non–negligible role of the thrust coefficient on the evaluation of the specific impulse discrepancy, and a certain amount of friction

and divergence losses which are not taken into account by the CEA ideal nozzle model.

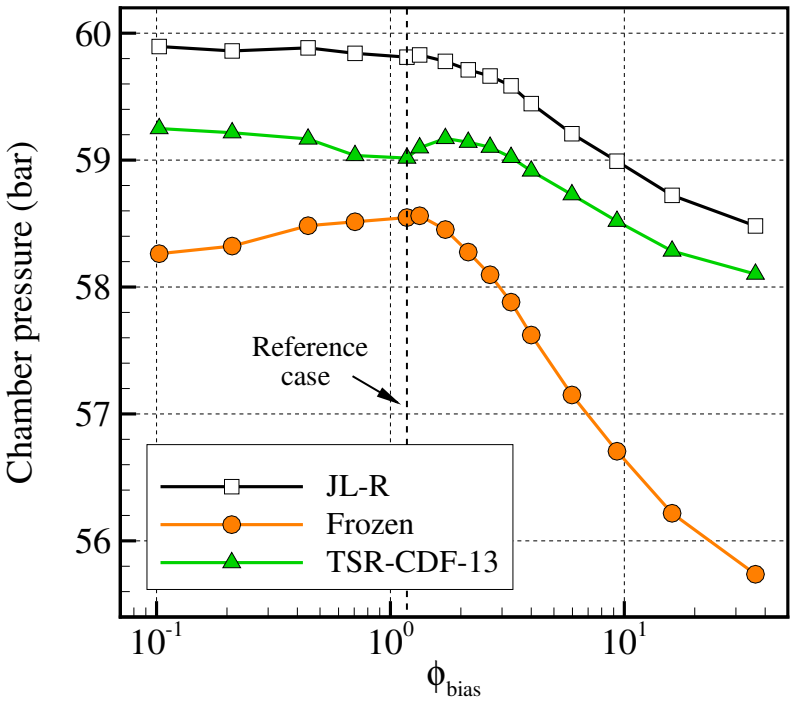

Figure 58: Chamber pressures obtained at different peripheral equivalence ratios (see Eq. (126)) using frozen, JL–R, and TSR–CDF–13 chemical kinetics.

A further comparison between frozen and JL–R finite–rate chemical kinetics can be performed by considering the qualitative behaviour of numerical results. Such a comparison is shown in Fig. 59, where the two set of numerical results are normalized by means of the reference solution featuring the respective chemical modeling. The unsuitability of the frozen approach to perform heat flux analyses in oxygen/methane LRE combustion chambers is highlighted in the low equivalence ratio region, where the two chemical models behave very differently as described above. However, a questionable behaviour of JL–R numerical results is observed in this region (i.e. high peripheral mixture ratios), since the slightly decreasing trend shown on top–left of Fig. 59 may be not representative of what observed for frozen calculations. In fact, an increasing trend would be expected as more suitable to represent the higher and higher chemical activity yielded by the recombination of carbon dioxide as the equivalence ratio is decreased.
On the other hand, a higher slope is observed for JL–R finite rate results than frozen chemistry in most of the fuel–rich region, providing lower throat heat flux for the same value of peripheral equivalence ratio. That might be justified as a direct consequence of the local chemical behaviour yielded by the peripheral flow injection on the throat near–wall region. Differently from the case

in which no chemical reactions occur, the peripheral flow has the capability to generate a layer of fuel–rich combustion products with lower equilibrium temperature, providing beneficial cooling effects. As it can be observed from the two profiles of throat wall heat flux in Fig. 59, such an effect depends on the peripheral flow chemical composition as well as on the blowing ratio, which is constant in this analysis.

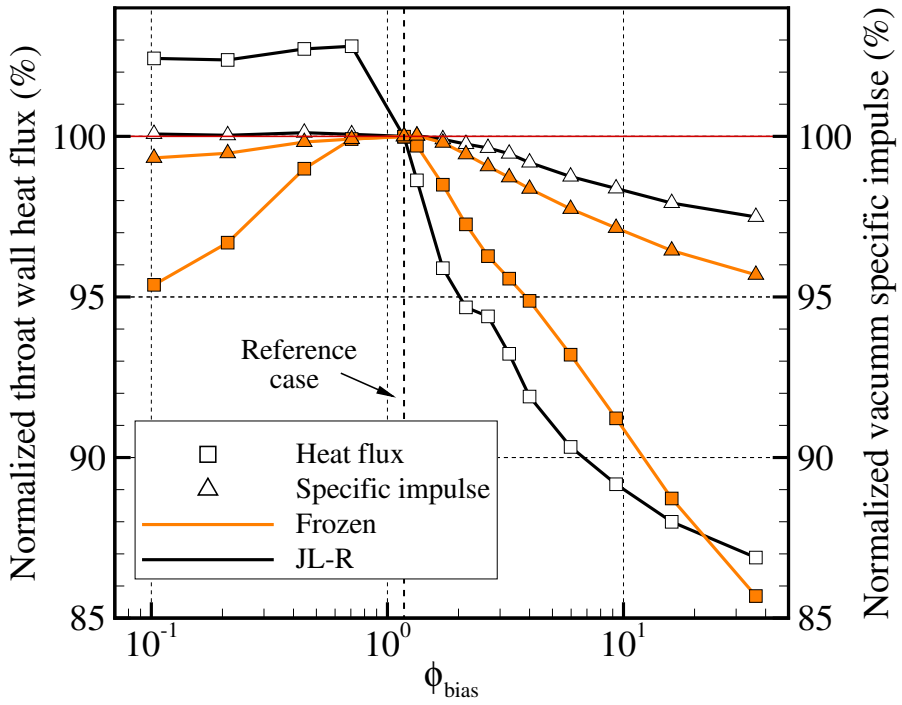

Figure 59: Comparison between throat wall heat flux and vacuum specific impulse obtained at different peripheral equivalence ratios using the JL–R reaction mechanism and frozen chemistry. Results are normalized with respective reference cases.

Results are distributed almost on a straight line in case of frozen simulations, whereas a nearly–quadratic trend is shown when chemical reaction are taken into account by means of the JL–R reaction mechanism. The TSR–CDF–13 skeletal reaction mechanism is employed as a second term of comparison for the JL–R chemistry model to assess the reliability of numerical results obtained by means of a global chemical kinetics in the framework of the present analysis, which involves a large spectrum of operating conditions. Throat wall heat fluxes and vacuum specific impulses obtained by means of the two reaction mechanism are shown in Fig. 60. Overall, the TSR–CDF–13 skeletal reaction mechanism yields more effective cooling capabilities than the JL–R, as lower throat wall heat fluxes are shown over the whole range of equivalence ratios (Fig. 60a). However, good agreement is found between the two reaction mechanisms, with a maximum discrepancy of 3 % in the oxidizer–rich region and

2 % in the fuel–rich region. In particular, excellent agreement is observed for equivalence ratios between 2.15 and 3.27, with errors highly below 1 %. A difference between throat wall heat fluxes calculated by means of the two chemical models is obtained also in the reference case, where the hot gas and peripheral mixture ratios are the same.

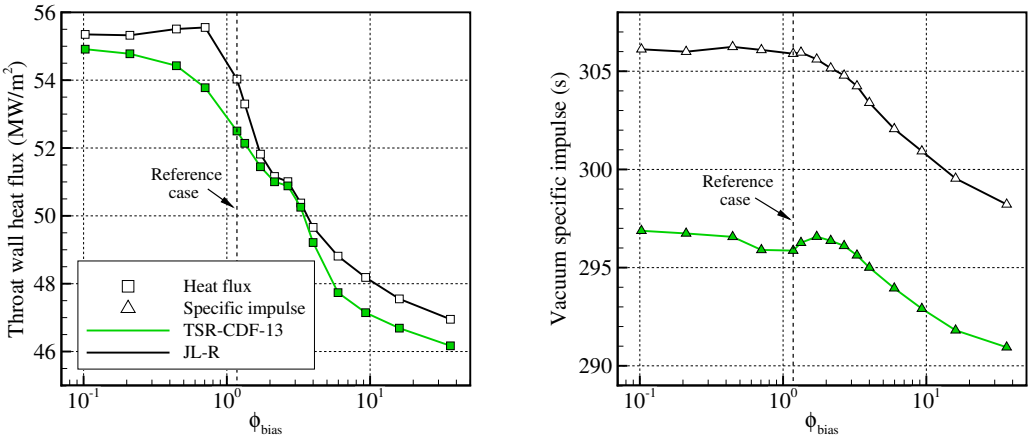

(a) (b)

Figure 60: Comparison between throat wall heat flux and vacuum specific impulse obtained at different peripheral equivalence ratios using the JL–R and TSR–CDF–13 reaction mechanisms.

This is probably justified by the different boundary layer chemical kinetics occurring as a result of the low wall temperature with the two chemical models. On the other hand, the TSR–CDF–13 skeletal reaction mechanism provides lower vacuum specific impulse than the JL–R, with an average discrepancy of -3 % (Fig. 60b). That is justified by the lower chamber pressure, and thus characteristic velocity, yielded by the skeletal mechanism due to the slower chemical recombination processes (see Fig. 58). Note that the TSR–CDF–13 vacuum specific impulses are still higher than those provided by frozen chemistry of about 2 %.

Normalized profiles of throat wall heat flux and vacuum specific impulse are compared also in case of the two reaction mechanisms. The comparison is provided in Fig. 61. It should be recalled that the JL–R reaction mechanism has been chosen to be used in this research due to its large employment in the literature for rocket–like applications. However, the high levels of bias in the peripheral mixture ratio considered in this analysis may yield peripheral flows very far from the reference condition, which is characterized by a reasonable rocket–like mixture ratio of 3.4. For this reason, the behaviour of JL–R numerical results starts to be less representative of that shown by a detailed chemical kinetics when conditions far from the reference one are considered (see Fig. 61). A different trend is shown by the TSR–CDF–13 reaction mechanism in the oxidizer–rich region with respect to the JL–R, more in line with the

increasing carbon dioxide recombination activity observed for frozen chemistry results. As previously mentioned, such conditions are of less practical interest in LRE applications than fuel rich-biased peripheral flows, which actually yield a reduction of throat heat flux with respect to the reference configuration. On the other hand, in the fuel–rich region, both throat heat fluxes and vacuum specific impulses decrease with similar slopes as the peripheral equivalence ratio is increased, showing very similar qualitative behaviours.

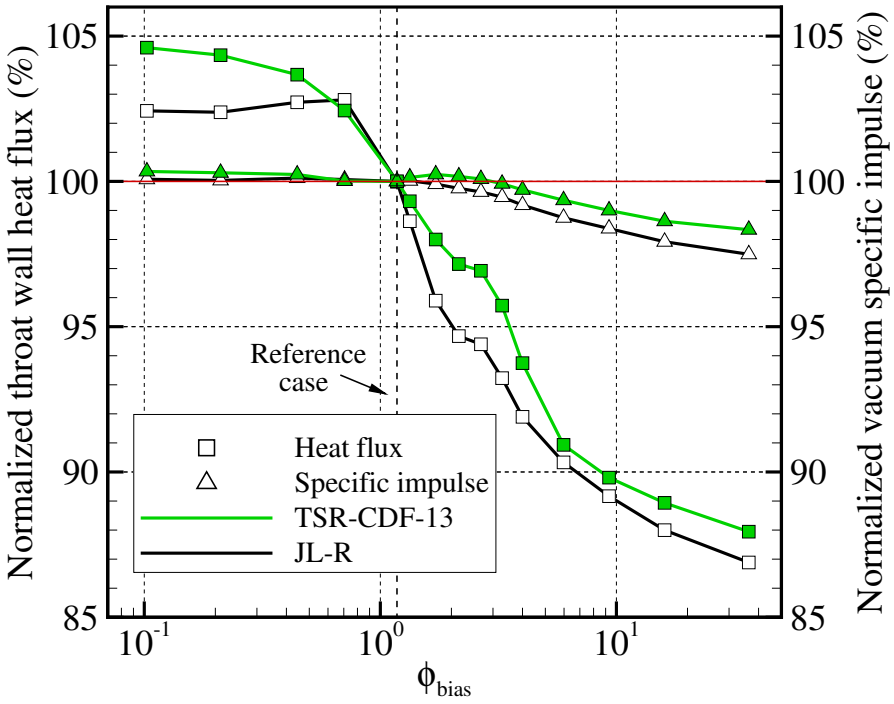

Figure 61: Comparison between throat wall heat flux and vacuum specific impulse obtained at different peripheral equivalence ratios using the JL–R and TSR-CDF-13 reaction mechanisms. Results are normalized with respective reference cases.

Overall, the discrepancies shown by the JL–R global reaction mechanism on the throat wall heat flux and vacuum specific impulse with respect to the TSR–CDF–13 skeletal reaction mechanism can be considered reasonably acceptable to carry out heat flux predictions of mixture ratio–biased LRE thrust chambers. The JL–R chemical model has been capable to well reproduce the behaviour provided by numerical simulations featuring a detailed chemical kinetics, representing a good compromise between accuracy and computational cost. In fact, it is worth noticing that the higher number of state variables (species) and reactions required by the TSR–CDF–13 skeletal reaction mechanism yield an increase of computational cost from 5 to 10 times with respect to the same simulation performed by means of the JL–R global chemistry.

A final comparison between the three chemical kinetics models is shown in Fig. 62.

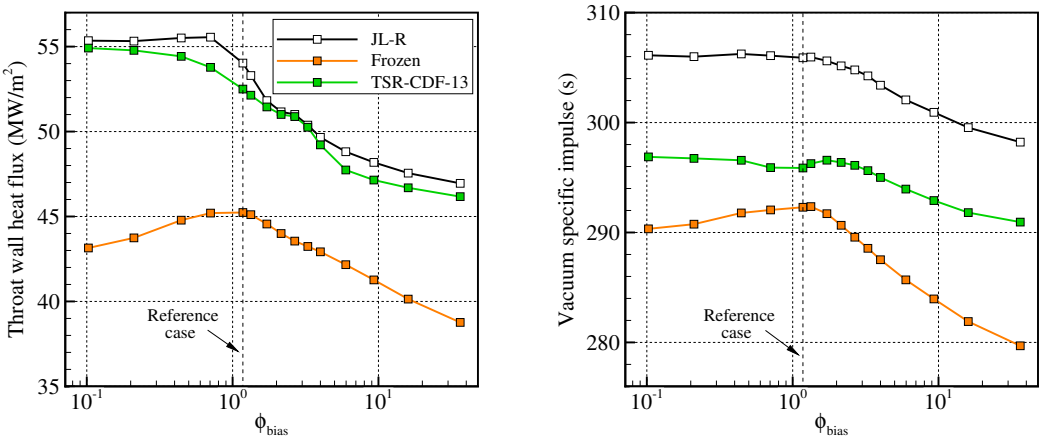

Figure 62: Comparison between throat wall heat flux (a) and vacuum specific impulse (b) obtained at different peripheral equivalence ratios and for frozen, JL–R, and TSR–CDF–13 chemical kinetics.

Moreover, all the presented numerical results concerning mixture ratio bias numerical simulations featuring the JL–R reaction mechanism are summarized in Table 16.

Table 16: Summary of mixture ratio bias numerical results obtained by means of the JL–R reaction mechanism.

O/F_g	O/F_{bias}	ϕ_{bias}	$\left.\frac{q_w}{q_{w,ref}}\right\|_{th}$ (%)	$\frac{I_{vac}}{I_{vac,ref}}$ (%)
3.26	39.00	0.102	102.43	100.08
3.275	19.00	0.210	102.38	100.03
3.31	9.00	0.444	102.72	100.11
3.34	5.67	0.705	102.81	100.07
3.38	4.00	1.176	99.99	100.00
3.42	3.00	1.333	98.63	100.02
3.45	2.33	1.717	95.90	99.91
3.49	1.86	2.150	94.68	99.76
3.53	1.50	2.667	94.40	99.64
3.57	1.22	3.279	93.23	99.46
3.61	1.00	4.000	91.90	99.18
3.69	0.67	5.970	90.33	98.75
3.77	0.43	9.302	89.17	98.38
3.86	0.25	16.00	88.00	97.92
3.95	0.11	36.36	86.89	97.49

6 VALIDATION OF REDUCED MODELS

In the present chapter, the validation of the liquid and gaseous film cooling low–order models presented in Chap. 3 is illustrated, with the presentation of the numerical results carried out by means of the EcosimPro/ESPSS simulation platform. Reduced models are validated against experimental data, suitably selected in the framework of the already–mentioned literature review, and CFD numerical simulations either taken from the literature and purposely carried out reproducing the test case under investigation. The selection of the test cases involved several difficulties due to the high unavailability of experimental data in the literature concerning film cooled rocket engines.
Recurring issues in the selection procedure have been:

- The employment of coolants unsuited for modern rocket engine applications (e.g. aniline–alcohol, ethyl alcohol, gasoline, B_2H_6, etc.), mainly belonging to the early age of film cooling experimental testing;
- Coolant injection performed close to the nozzle, hence not appropriate for the validation of the presented models, which do not model the flow evolution after the convergent part;
- The lack of test information, which made impossible the numerical reproduction of the experiment;
- Limited, poor–quality, or unappropriate observables;
- The employment of complex thrust chamber assembly configurations, for instance with the presence of a pre–burner, which might interfere in the estimations. Indeed, uncertainties in flow data might cause additional errors on top of the ones entailed from the simplified modeling of film cooling.

Nevertheless, some of those issues could be retained, at least for validation purposes. In the end, four experimental tests have been considered acceptable for the validation of numerical models, two for liquid film cooling and two for gaseous film cooling. Those are illustrated in the following, focusing on the chamber characteristics, operating conditions, film injection details, but also on how the configurations have been transposed in the EcosimPro/ESPSS environment, trying to best reproduce the experimental features. Numerical results aimed at reproducing the specific test observables are then presented and discussed in each case.

6.1 LIQUID FILM COOLING TEST CASES

The first experimental test selected for liquid film cooling reduced models validation is that by Morrell [29]. The investigation consisted in a series of 59 tests employing a liquid oxygen/liquid ammonia thrust chamber. Liquid ammonia, ethyl alcohol, and water have been used as coolants, injected in the chamber by means of different configurations, such as tangential and vertical slots. Wall integral heat load, thrust, and film cooled length are evaluated in a 21.6 cm–long test section located downstream of the injection plate, as shown in Fig. 63. The latter shows also the geometry of the chamber.

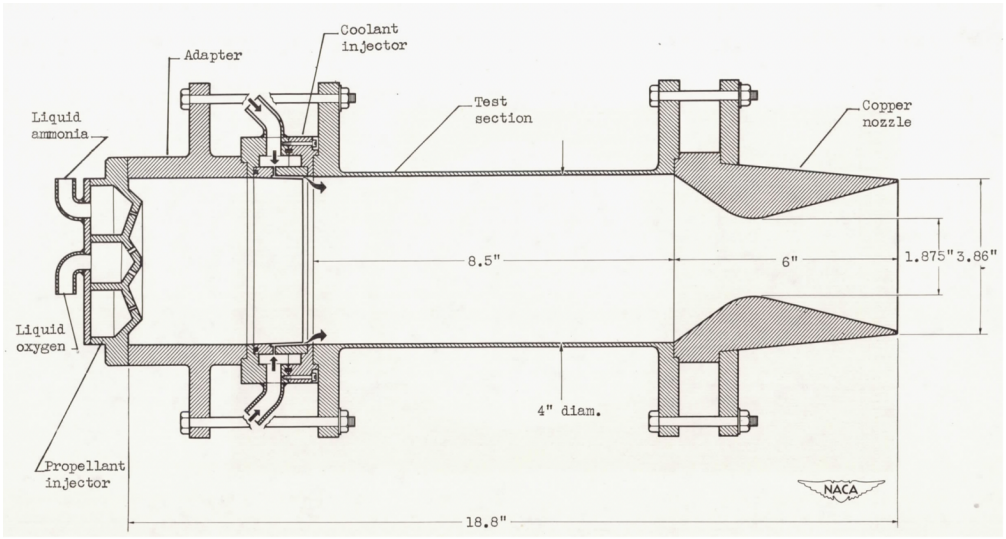

Figure 63: Sketch of test chamber used in Morrell experiment [29].

It is worth specifying that the heat load is computed from temperature measurements performed with thermocouples. Note that no details on the temperature and heat profiles are provided in Ref. [29], and that only heat integral values are provided. Tests have been performed using different coolants and mass flow rates. In this framework, not all the experimental tests have been considered suitable for validation due to the following reasons. First, the vertical slot injection configurations have been excluded since the new ESPSS thrust chamber component is capable to handle only tangential film injection. Moreover, a further aspect to consider is the choice of the coolant. Liquid ammonia showed unexpected behavior during the tests, since no sharp changes in wall temperature were observed as the coolant approached the boiling temperature [29]. In this regard, Morrell concluded that the coolant existed as a superheated fluid until the critical temperature of ammonia at the test conditions ($\approx$ 405 K), and the cooling process downstream was disregarded. On the other hand, ethyl alcohol was successfully used as coolant during the tests, but only employing vertical injection slot configurations. As far as the above–mentioned aspects are concerned, only 4 tests out of 59 are considered (from test 8 to 11). The tests

foresee water as coolant, injected tangentially at the injection plate. Experimental mass flow rates for such tests are shown in Table 17.

Table 17: Experimental oxidizer, fuel, and coolant mass flow rates used by Morrell [29] in different tests.

Test	$\dot{m}_o$ (kg/s)	$\dot{m}_f$ (kg/s)	$\dot{m}_c$ (kg/s)
8	0.99	0.70	0.084
9	1.05	0.69	0.084
10	1.16	0.66	0.093
11	1.14	0.68	0.095

The thrust chamber employed by Morrell has been reproduced in the EcosimPro/ESPSS environment using the schematics shown in Fig. 64 for all the four operating conditions shown in Table 17.

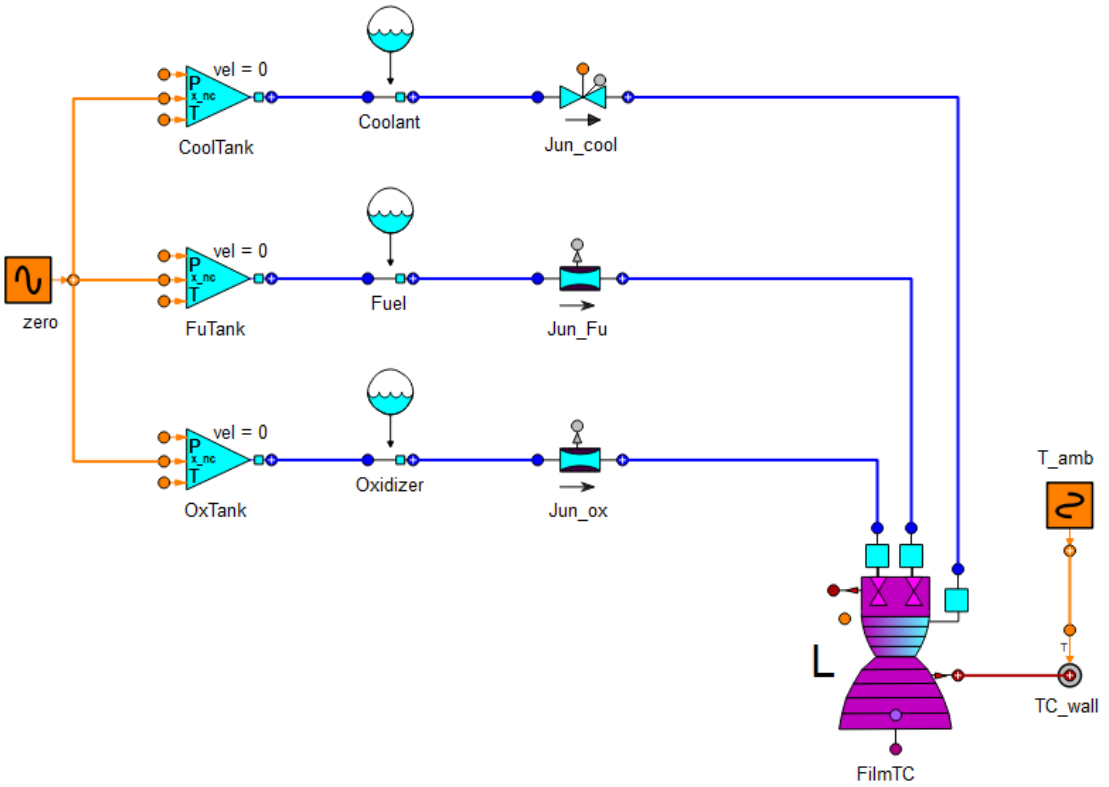

Figure 64: Schematics used to replicate experimental data by Morrell [29] in EcosimPro.

Apart from the new liquid film cooled thrust chamber, the model has been built by means of basic components included in the ESPSS libraries. Three time–dependant boundary condition components (*OxTank*, *FuTank*, and *CoolTank*) are employed for the propellants and the coolant, simulating tanks with infinite capacity. Pressure and temperature are then enforced before the simulation start.

Pressure and injection areas have been suitably tuned to match the experimental mass flow rates. The fluid chemicals are then defined by components *Oxidizer*, *Fuel*, and *Coolant*, linked to two junctions and a valve for the calculation of mass flow rate, species and energy fluxes. A valve is chosen for the coolant line since a slower and progressive opening sequence has been observed to improve robustness of the simulation. Ambient temperature is enforced at the chamber wall, which is not included in the thrust chamber component, and, for this reason, it is modeled by the *TC_wall* thermal node component. In this case and in all the other simulations, the thrust chamber has been discretized with 30 nodes, 20 for the combustion chamber until the throat and 10 for the divergent nozzle.

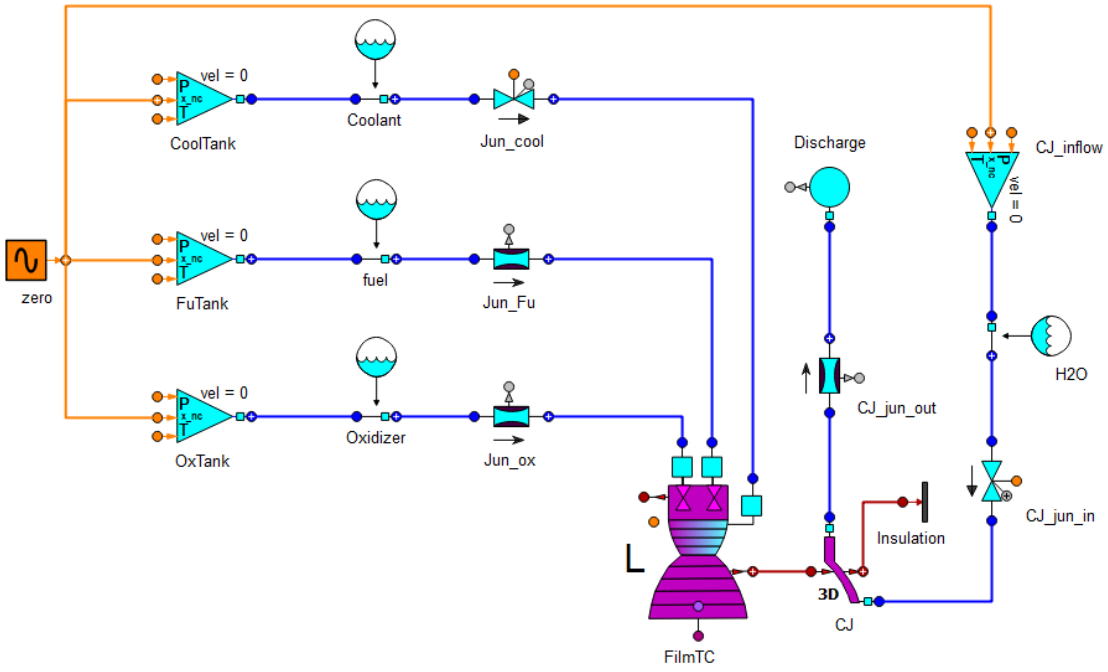

Figure 65: Schematics used to replicate experimental data by Kim et al. [42] in EcosimPro.

The second liquid film cooling experiment is provided by Kim et al. [42], and features a film– and regeneratively–cooled liquid oxygen/kerosene calorimetric thrust chamber. The thrust chamber is 488 mm–long, and consists of a cylindrical part with a diameter of 108 mm and a nozzle throat with a diameter of 50 mm. The contraction ratio is then 4.66. Kerosene is used either as fuel and as film coolant, and is injected tangentially right at the injector plate. The thrust chamber is surrounded by 19 copper–alloy cooling channels, 8 belonging to the cylindrical part, and 11 to the nozzle. The latter are used during the experiment to provide heat flux measurements, which are performed by evaluating the total enthalpy difference between cooling circuits manifolds. Good spatial resolution of measurements is ensured by the presence of many cooling circuits. Ambient temperature water is used in the cooling channels, with a

mass flow rate of 27 kg/s for each channel. In addition to heat flux axial profiles, the experiment provides an estimation of the average hot gas–side wall temperature and characteristic velocity.
The model in Fig. 65 is used to reproduce experimental data by Kim et al. [42]. Since the test hardware features a calorimetric thrust chamber equipped with cooling jackets, the model shown in Fig. 64 is no longer appropriate to suitably reproduce the present experiment. To improve model reliability, the film–cooled thrust chamber is connected to a 3–D cooling jacket component, namely *CJ* in the schematics, which distributes the cooling channels between the combustion chamber and the nozzle as explained above. The regenerative circuit belongs to a separated valve–controlled line with a high–pressure water inflow (*CJ_inflow*) which discharges in a high–capacity volume (*Discharge*). Volume capacity is high enough to have no influence on the system dynamics due to pressure increase. Cooling circuits outer wall is set as adiabatic through the component *Insulation*. Test conditions feature a chamber pressure of 52.5 bar, and oxidizer, fuel, and coolant kerosene mass flow rates of 4.42, 1.59, and 0.166 kg/s, respectively.
As far as kerosene is concerned, it should be noted that the ESPSS libraries does not foresee a real fluid modelling for this chemical, as done for instance for water, hydrogen, and methane. In fact, kerosene is modelled in EcosimPro according to a perfect liquid approach, which does not allow any phase change, hence entering in conflict with the liquid film cooling models which instead foresee coolant evaporation. For these reasons, some average properties have been roughly introduced in the EcosimPro/ESPSS fluid database for kerosene, to eventually reproduce the experiment. Properties include a decomposition (pseudo–evaporation) temperature of 500 K, a vaporization enthalpy of 251 kJ/kg, a density of 950 kg/m^3, a specific heat at constant pressure of 1800 J/(kg · K), a dynamic viscosity of 9.5 $\cdot 10^{-5}$ Pa·s, and a thermal conductivity of 0.17 W/(m·K) [147].

6.2 GASEOUS FILM COOLING TEST CASES

The experimental test performed by Arnold et al. [80] is considered as the first test case for gaseous film cooling reduced models validation. The latter foresees the investigation of film cooling performances in a high–pressure liquid oxygen/gaseous hydrogen combustion chamber. Test hardware features a subscale thrust chamber operating at about 111 bar. In particular, the latter is made by 5 segments, with cylindrical segments totalizing a length of 200 mm, and chamber and throat diameters equal to 50 and 33 mm, respectively. Coolant is ambient–temperature hydrogen, which is injected right at the injection plate by means of 10 rectangular slots, evenly distributed in the circumferential direction with an aspect ratio of about 10. The slot height, in particular, is 0.4 mm. Available observables are axial measurements of wall heat flux in the cylindri-

cal part of the combustion chamber. Information about heat flux distribution is provided on the hot inner surface of the combustion chamber, starting from thermocouple temperature measurements.

To reproduce such observables, the EcosimPro schematics shown in Fig. 66 is employed. As it can be noted, the schematic model is very similar to that used for Morrell experiment [29], with the exception of the different thrust chamber component.

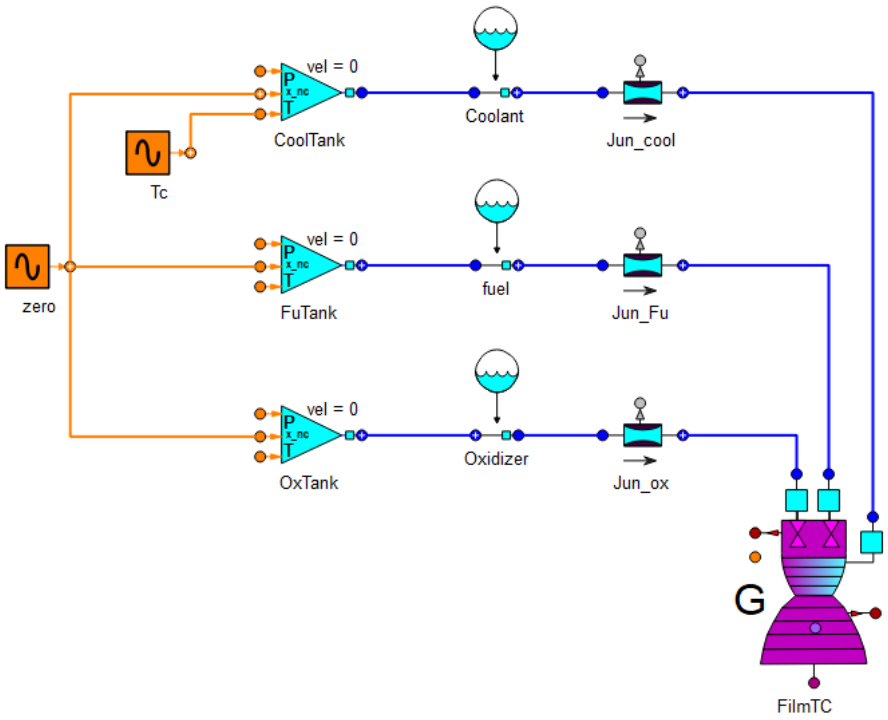

Figure 66: Schematics used to replicate experimental data by Arnold et al. [80] in EcosimPro.

Hot gas-side wall temperature thermocouple measurements are provided in Ref. [80], so it is possible to use them as boundary condition to retrieve the experimental heat flux numerically. Therefore, wall temperature data are linearly interpolated and taken as the boundary condition for the combustion chamber wall. The temperature after the last available measurement point is set constant. Ambient conditions were enforced at the nozzle exit in order to reproduce the same environmental conditions of the experiment.

Further experimental information for the present research is provided by Suslov et al. [101] who employed a low–pressure oxygen/methane thrust chamber to carry out wall heat flux measurements. This combustion chamber has been specifically designed to study the wall heat transfer characteristics, and the investigation focuses on the interaction of the reacting flow with film cooling in the cylindrical part of the combustion chamber near the injector plate, eventually providing information on heat loads distribution at chamber pressures up to 12 bar. Coolant is ambient–temperature methane, which is injected

tangentially at the injection plate by means of a ring injection slot. Therefore, coolant injection is axisymmetric, with a slot height of 0.46 mm. The combustion chamber is divided in 5 segments, and surrounded by cooling channels to carry out heat flux measurements, similarly to experiments presented in Refs. [15, 42]. As a result, the present experimental data consist only of 5 average wall heat flux values, one for each chamber segment. Operating conditions are shown in Table 18.

Table 18: Operating conditions for oxygen–methane reference test cases.

Test case	$\dot{m}_o$ (kg/s)	$\dot{m}_f$ (kg/s)	$\dot{m}_c$ (kg/s)	h_{slot} (mm)
Suslov et al. [101]	0.335	0.1	0.087 (20 % $\dot{m}_{tot}$)	0.46
CFD	0.335	0.1	0.022 (5 % $\dot{m}_{tot}$)	0.20

Note that experimental coolant mass flow rate is equal to 20% of the total mass flow rate, which is a very high amount to be used in a film cooling application. For this reason, this test is considered more as a case–study rather than a real application. For the sake of completeness, a second set of oxygen–methane validation data is provided by a CFD simulation performed in the framework of the present research. As shown in Table 18, the latter foresees the same propellant mass flow rates of Ref. [101], but a lower coolant mass flow rate, equal to 5% of the propellants. A lower film injection slot height of 0.20 mm has been also used to maintain an effective film velocity after the mass flow rate reduction. It is worth noticing that the two test conditions presented in Table 18 do not yield the wall–jet regime mentioned in Sec. 3.2, i.e. where the original and unmodified gaseous film cooling reduced model by Simon–Di Matteo et al. was valid. Hydrogen applications do usually generate a wall–jet flow due to the very low density of the coolant, which leads to high film velocities even using low film mass flow rates, and hence lowering the velocity ratio (see Eq. (76)) below 1. For instance, the experiment performed by Arnold et al. briefly described above yields a velocity ratio of 0.7 considering also the contribution of the factor k_R for discrete slot film injection (see Eq. (76)). On the other hand, coolant methane usually shows lower velocities than the hot gases for the opposite reason, thus yielding a different cooling performances in the first half of the combustion chamber being the velocity ratio higher than 1. A velocity ratio of 1.6 has been observed in the 5% film mass flow rate CFD simulation. Furthermore, being these oxygen–methane test cases outside of the applicability range of the original gaseous film cooling model, they represent a fundamental opportunity to show the capabilities of the improvements introduced in the formulation during this Ph.D. research. The same EcosimPro schematics used for the oxygen–hydrogen test (see Fig. 66) is employed here for both oxygen–methane cases, since no modifications are required with the exception of the different fuel and coolant. Although cooling channels have been necessary to carry out experimental heat flux measurements, they are not present in the schematics as done instead in Fig. 65. That is justified by the rea-

sonable accuracy provided by CFD simulations (see Fig. 71), obtained without any modelling of the cooling channels.

6.3 RESULTS

The numerical results obtained for all the test cases are presented in the following. First, the liquid film cooling models validation against Morrell experimental data is presented. Available observables have been reproduced using all the three liquid film cooling models presented in Chap. 3, and are shown in Table. 19.

Table 19: Experimental and estimated observables by Morrell [29].

Test 8	EXP	Grisson full	Grisson simpl	Shine	**Test 9**	EXP	Grisson full	Grisson simpl	Shine
F (kgf)	404.6	382.3	381.4	391.7	–	397.3	384	383.4	383.6
ε_F (%)	–	-5.52	-5.73	-5.65	–	–	-3.34	-3.49	-3.45
FCL (m)	0.1879	0.2167	0.221	0.2193	–	0.2073	0.2236	0.2343	0.229
ε_{FCL} (%)	–	15.32	17.61	16.71	–	–	7.86	13.03	10.46
Q_{tot} (btu/lb)	876	829.9	nr	nr	–	871	823.2	nr	nr
$\varepsilon_{Q_{tot}}$ (%)	–	-5.26	–	–	–	–	-5.49	–	–
Q_{conv} (btu/lb)	732	706.9	nr	nr	–	736	701.74	nr	nr
$\varepsilon_{Q_{conv}}$ (%)	–	-3.42	–	–	–	–	-4.65	–	–
Q_{rad} (btu/lb)	144	123	nr	nr	–	135	121.47	nr	nr
$\varepsilon_{Q_{rad}}$ (%)	–	-14.55	–	–	–	–	-10	–	–
Test 10					**Test 11**				
F (kgf)	415.9	393.88	393.53	394	–	415.9	397.56	397	397
ε_F (%)	–	-5.29	-5.37	-5.27	–	–	-4.40	-4.54	-4.54
FCL (m)	0.2042	0.2419	0.2671	0.2549	–	0.2174	0.2411	0.2663	0.2537
ε_{FCL} (%)	–	18.46	30.8	24.82	–	–	10.90	22.49	16.69
Q_{tot} (btu/lb)	856	559	nr	nr	–	856	560	nr	nr
$\varepsilon_{Q_{tot}}$ (%)	–	-34.69	–	–	–	–	-34.58	–	–
Q_{conv} (btu/lb)	731	450	nr	nr	–	721	456.02	nr	nr
$\varepsilon_{Q_{conv}}$ (%)	–	-38.44	–	–	–	–	-36.75	–	–
Q_{rad} (btu/lb)	125	110	nr	nr	–	135	103.9	nr	nr
$\varepsilon_{Q_{rad}}$ (%)	–	-12	–	–	–	–	-23.04	–	–

nr stands for not reliable.

In particular, F is the thrust, FCL is the film cooled length, Q_{tot}, Q_{conv}, and Q_{rad} are the total, convective, and radiative heats released at the wall, and $\varepsilon_.$ are the discrepancies evaluated with respect to the experimental data.
The mixing process between the coolant and the hot gas provides has been correctly reproduced, providing a good estimation of the thrust, which is in good agreement with experimental data for all the three models for each test. In fact, all the three formulations model the chamber pressurization due to coolant injection, yielding a maximum error ε_F of -5.73%. Film cooled length tends to be overestimated by all the models, in each test case, even if acceptable ranges of errors are provided, with an average level of about 15%. As expected, the best evaluations are provided by the most detailed model, i.e. Grisson model in full formulation. Moreover, 0–D models (Simplified Grisson and Shine) return higher errors with respect to Grisson full formulation due to their higher level of simplification, and show a particularly similar behavior dealing with this specific test case. Between the two, Shine model seems to

give a slightly better accuracy in the film cooled length estimation. Full Grisson model is the only one that can be considered reliable when comparing integral heat loads, since it employs a specific and detailed modeling for the estimation of the wall heat exchange coefficients. Moreover, it gives the best estimation of the FCL, which is a key parameter when comparing the integral heat load, since the temperatures and the fluid properties of the liquid phase and of the evaporated boundary layer might be very different and might influence such an observable significantly.

Table 20: Experimental and estimated scalar observables by Kim et al. [42].

	EXP	Grisson full	Grisson simpl	Shine
c^* (m/s)	1670	1730	1728	1702
ε_{c^*} (%)	–	3.59	3.47	1.91
$\bar{T}_w$ (K)	610	668.2	576.8	796
$\varepsilon_{\bar{T}_w}$ (%)	–	9.54	-5.44	30.49

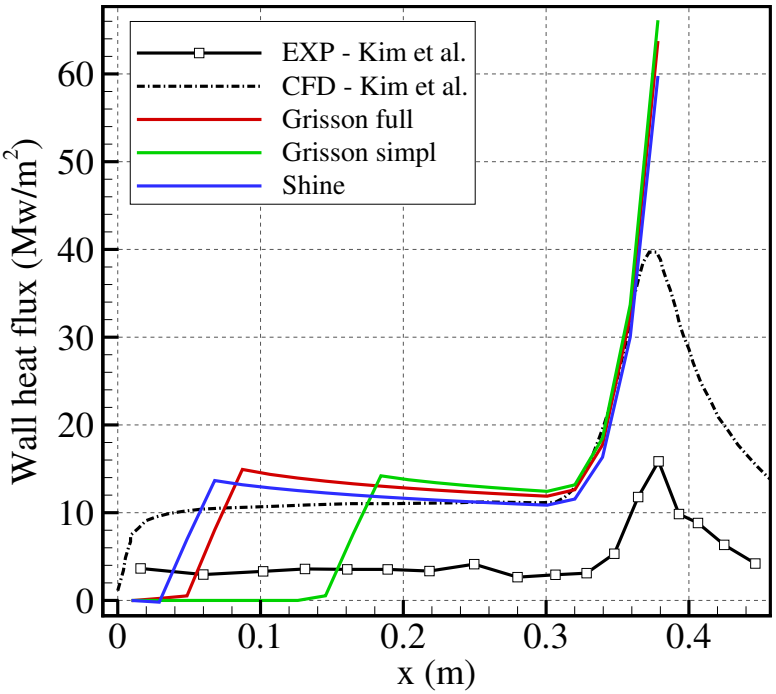

Figure 67: Experimental [42] and numerical wall heat flux computed with liquid film cooling models.

Performances are well predicted by each of the three models also dealing with the oxygen–kerosene experiment by Kim et al. Errors on characteristic velocity are confined below the 4% threshold, as shown in table 20. This proves that the assumptions made on the mixing process between the evaporated coolant and the hot gases are appropriate. Wall temperatures are in good

agreement with experimental data as well. As expected, also here the complete Grisson model provides the most reliable results, with an error of 9.5% with respect to the experiment, whereas the highest discrepancy is showed by Shine model, which overestimates the wall temperature by a factor of 30.5%. Nevertheless, the lowest error on the average wall temperature prediction is provided by the Simplified Grisson model, which provides a better prediction than the full formulation. Although the temperature averaging process is not explained in detail by the authors, this aspect is quite surprising because of the lower reliability expected by 0–D models concerning the heat transfer evaluation. One possible explanation might be the interplay of two different effects: on one hand, 0–D models generally tend to overestimate wall temperature; on the other one, simplified Grisson model provides a higher film cooled length than the other two models, as can be observed from Fig. 67, thus considering a higher wall region with low temperature which contributes to decrease the average value in the combustion chamber. As a possible consequence of this combined and counterbalanced effect, what is observed is an average wall temperature which is close to experimental data. Moreover, the simplified Grisson model would be expected to provide an error $\varepsilon_{\bar{T}_w}$ similar to that of Shine model due to the similar nature of the two. Instead, the trend is inverted providing a negative error (-5.44%), suggesting that something different is occurring. It should be also noted that such an effect on average wall temperature might be case dependent.

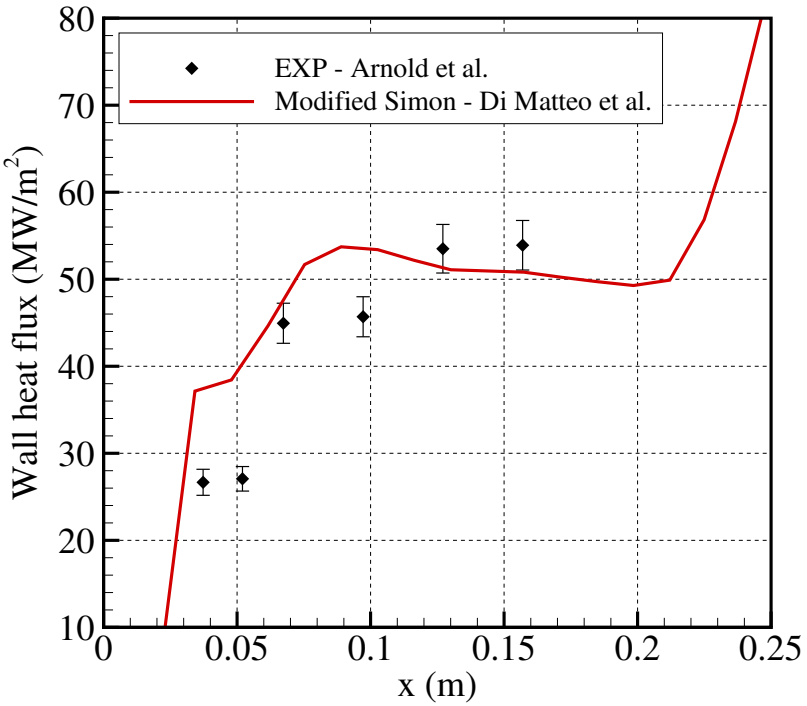

Figure 68: Experimental [80] and numerical wall heat flux computed with the gaseous film cooling model.

Concerning convective heat fluxes, all the three liquid film cooling models (red, green, and blue solid lines in Fig. 67) provide similar results and overestimate experimental data (black solid line with symbols). However, it must be pointed out that the results are in good agreement with CFD simulations performed by Kim et al., also shown in Fig. 67 with a point–dashed line. Such facts might be due to some physics happening in the experiment which is not properly modeled numerically. Eventually, the wall heat fluxes provided by reduced models in the convergent nozzle are also in good agreement with each other and with the CFD simulation performed in Ref. [42]. Nevertheless, they are hardly comparable at throat due to model limitations.

Figure 68 reports the comparison between experimental and numerical wall heat flux in case of Arnold et al. oxygen–hydrogen test case. Numerical solution is in overall good agreement with experimental data, which are also affected by some uncertainty as reported by the authors. Some discrepancies can be observed in the heat release zone, where the heat flux is increasing, but, nevertheless, judging from the experimental trend the film region extension seems to be well reproduced by the model. Maximum heat flux in the combustion chamber upstream of the nozzle is reproduced within the experimental uncertainty. Although in this case the film region extension is not an observable explicitly provided by the experiment, it is worth noticing that the potential core length yielded by the gaseous film cooling model is equal to 17 mm (recall that chamber length is 200 mm). As already mentioned in Sec 6.2, the hydrogen test case belongs to the wall–jet regime, hence providing a velocity ratio lower than 1, and equal to 0.7. For this reason, as far as the present test case is concerned, the potential core length is calculated using the Simon loop method described in Fig. 6, since all the applicability requirements are met. For the sake of completeness, the potential core length and velocity ratio EcosimPro simulation transients are shown in Fig. 69.

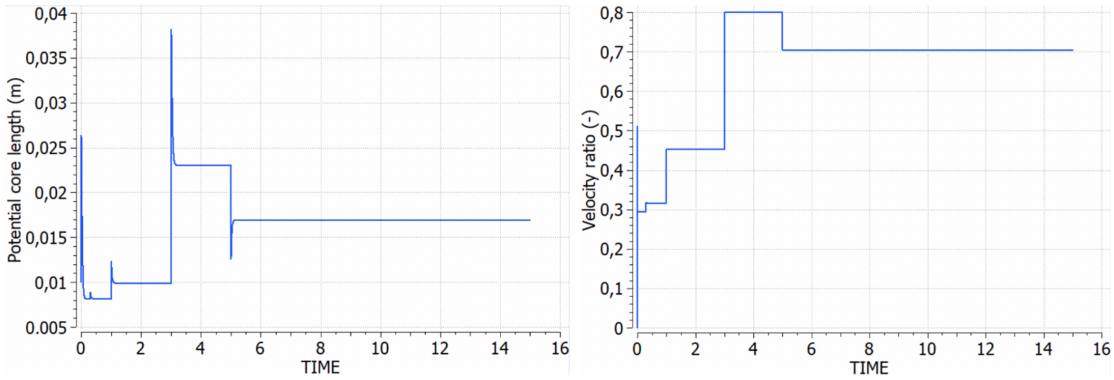

Figure 69: Potential core length (left) and velocity ratio (right) EcosimPro simulation transients reproducing the experimental test case by Arnold et al. [80]. Time is in seconds.

Eventually, the oxygen–methane numerical results are presented and compared to experimental data and CFD simulations. Experimental wall heat flux is well reproduced by the gaseous film cooling model (see Fig. 70), showing the increase due to heat release during combustion and the plateau after the end of the process. The typical sharp increase in the convergent part of the nozzle is also shown by the numerical solution (red line). Higher film extension is obtained by the numerical model, and thus higher error is shown close to the injection region. Downstream, experimental data are in good agreement with the numerical solution provided by the reduced model, with a maximum error of about 19%.

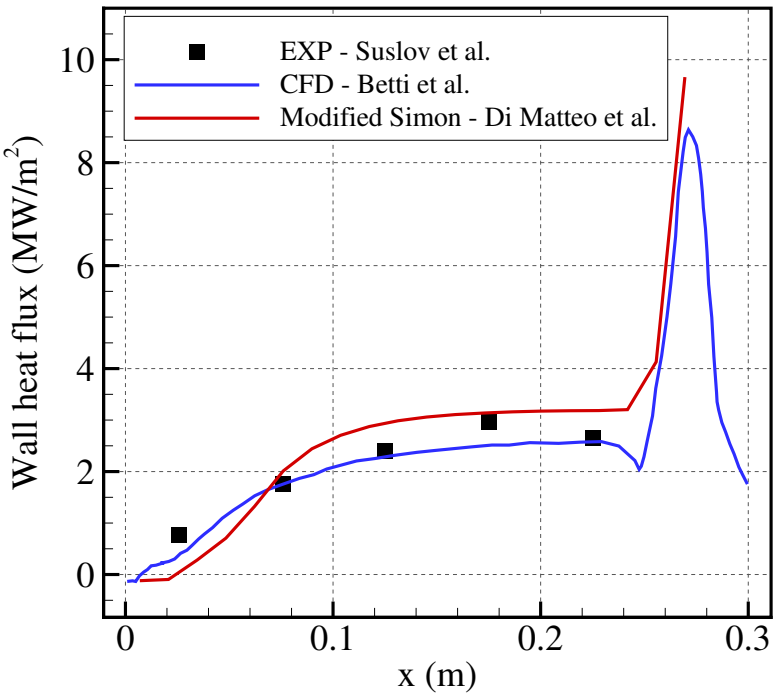

Figure 70: Experimental [101] and numerical wall heat flux computed with the gaseous film cooling model.

The numerical solution provided by the reduced model in EcosimPro is compared also with CFD simulation performed by Betti et al. [102] (blue line in Fig. 70), who performed comparison against the same test case. Although a better agreement is shown in the first chamber segments, numerical results can be reasonably compared despite the great difference in modelling complexity, indicating that the model developed in the framework of the present activity is a valid tool to perform reliable heat loads predictions. Furthermore, Fig. 71 shows the wall heat flux comparison between the reduced model results and the CFD simulation described in Table 18. The reduced model solution (red line) is in good agreement with that provided by the CFD simulation (black line), with a maximum error of 18% obtained toward the end of the combustion

chamber. A further solution without film cooling (blue line) is included in the comparison to appreciate the influence of coolant injection on the wall heat flux. Note that the uncooled simulation has been performed by means of the CPI approach presented in Sec. 4.2. Although some discrepancies in the film region, wall heat flux trend is qualitatively well predicted. An effective comparison is shown approaching the plateau in the first half of the chamber, where the two solutions are almost overlapped. Going downstream, reduced model solution (red line) shows a heat flux decrease due to the end of combustion process, whereas the CFD solution seems to keep the plateau until the convergent part of the nozzle.

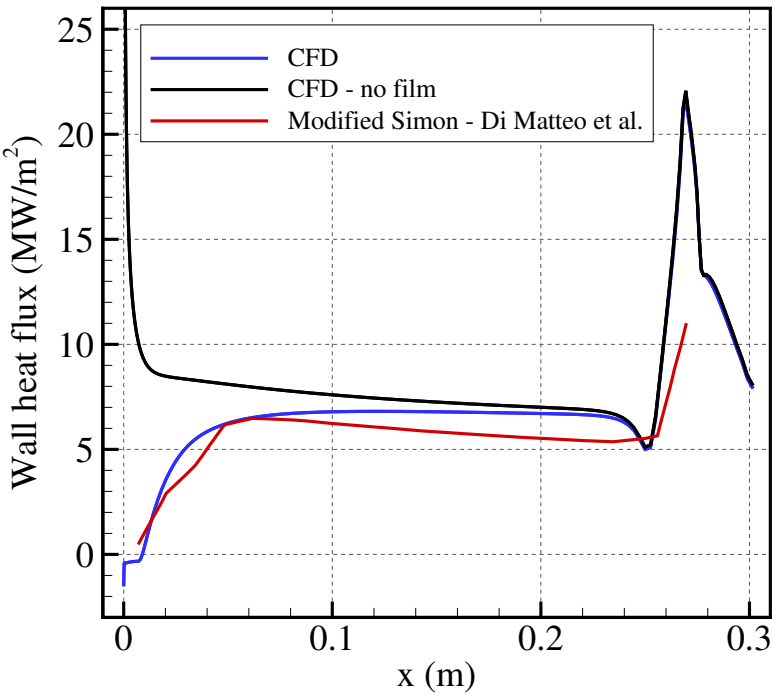

Figure 71: Comparison among gaseous film cooling model solution, experimental data, and CFD simulation.

7 CONCLUSIONS

This Ph.D. research aimed at performing heat transfer analyses in uncooled, film–cooled, and mixture ratio biased oxygen/methane LRE thrust chambers, focusing on the investigation of different modelling solutions representing a good trade–off between accuracy and computational cost.

The simplified CFD numerical approaches presented in this work have shown good predictive capabilities, allowing to perform quantitative comparisons with experimental data and numerical simulations characterized by higher levels of model completeness. Discrepancies within 6 % have been obtained on the throat wall heat flux and wall pressure in case of an uncooled engine. Because of the high versatility offered by such numerical approaches, it has been possible to compare different chemical models featuring frozen kinetics, global, and skeletal reaction mechanisms in the framework of parametric analyses, aimed also at evaluating the role of the main design parameters in film cooled and mixture ratio biased thrust chambers. In this regard, validation has not been performed due to the absence of detailed experimental data in the literature. However, the twofold characterization of such cooling strategies, providing either cooling beneficial effects and performance losses, has been successfully investigated by means of the presented numerical approaches, showing a clear relationship between the throat wall heat flux reduction and the vacuum specific impulse loss yielded by the injection of a secondary flow.

The reliability of the mentioned results allowed the CFD approaches to be employed for the development of a CFD–based numerical correlation, which has been included in a low–order model for the prediction of gaseous film cooling capabilities in the framework of LREs system analysis. Due to the extreme unavailability of experiments and literature references in general, it has been only possible to make adjustments to a previously–existing formulation, improving its predictive capabilities and range of application. Validation against experimental data provided wall heat flux discrepancies below the 20 % threshold, with computational times not higher than 15 minutes using the EcosimPro platform. Liquid film cooling has been investigated as well, observing it as a challenging phenomenon to be described in detail using low–order modelling despite the acceptable comparisons with selected test cases, requiring a comprehensive treatment accounting for the all complex underlying phenomenology.

The presented numerical approaches may be employed in the framework of the engine design phase, when a light and versatile numerical tool is required to effectively perform several iterations before obtaining results of practical interest. In such a way, the different design solutions may be rapidly compared, evaluating pros and cons, and eventually carrying out a preliminary sizing

of the thrust chamber in terms of achieved specific impulse and maximum allowable wall heat flux.

7.1 FUTURE PERSPECTIVES

Future developments are expected mostly for the analysis of film–cooled and mixture ratio biased thrust chambers. In fact, as far as the CFD analysis in oxygen/methane LRE is concerned, minimal information is available in the literature to the author's knowledge. Availability is even lower regarding mixture ratio bias. In this framework, interesting investigations will concern the analysis of such engineering devices in thrust chambers different from that considered in this thesis, hence studying possible geometry and scale effects on the throat wall heat flux and vacuum specific impulse. As this study considered only a single value of peripheral mass flow rate in the mixture ratio bias analysis, it would be also interesting to understand how different values of peripheral mass flow rates affect the throat heat loads and performances. On the other hand, numerical results have been carried out by means of simplified approaches in this thesis. From a modelling point of view, it will be important to compare the proposed numerical simulations with others performed by means of different approaches, for example different turbulence modelling, or the introduction of an eddy dissipation concept as a first solution to account also for turbulence–chemistry interaction. Moreover, even if not expected to provide significant contribution, the effect of radiation may be further investigated in film–cooling and mixture ratio bias applications. Eventually, experimental validation with test cases of practical interest of all the results presented in this work would be fundamental to assess their reliability.

BIBLIOGRAPHY

[1] D. R. Bartz. "A Simple Equation for Rapid Estimation of Rocket Nozzle Convective Heat Transfer Coefficients". In: *Jet Propulsion* 27 (1957), pp. 49–53. DOI: 10.2514/8.12572.

[2] G. P. Sutton and O. Biblarz. *Rocket Propulsion Elements*. Hoboken, New Jersey, USA: John Wiley & Sons, Inc., 2010. ISBN: 9780470080245.

[3] J. Locke, S. Pal, and R. Woodward. *Chamber Wall Heat Flux Measurements for a LOX/CH4 Propellant Uni-Element Rocket*. AIAA Paper 2007–5547. 43rd AIAA/ASME/SAE/ASEE Joint Propulsion Conference & Exhibit. 2007. DOI: 10.2514/6.2007-5547.

[4] D. I. Suslov, R. Arnold, and O. J. Haidn. *Convective and Film Cooled Nozzle Extension for a High Pressure Rocket Subscale Combustion Chamber*. AIAA Paper 2010–1150. 48th AIAA Aerospace Sciences Meeting Including the New Horizons Forum and Aerospace Exposition. 2010. DOI: 10.2514/6.2010-1150.

[5] M. P. Celano, S. Silvestri, G. Schlieben, C. Kirchberger, O. Haidn, and O. Knab. "Injector Characterization for a Gaseous Oxygen-Methane Single Element Combustion Chamber". In: *Progress in Propulsion Physics* 8 (2016), pp. 145–164. DOI: 10.1051/eucass/201608145.

[6] P. Grenard, N. Fdida, L. Vingert, L. H. Dorey, L. Selle, and J. Pichillou. "Experimental Investigation of Heat Transfer in a Subscale Liquid Rocket Engine". In: *Journal of Propulsion and Power* 35.3 (2019), pp. 544–551. DOI: 10.2514/1.B36928.

[7] M. Pizzarelli. "Overview and Analysis of the Experimentally Measured Throat Heat Transfer in Liquid Rocket Engine Thrust Chambers". In: *Acta Astronautica* 184 (2021), pp. 46–58. DOI: 10.1016/j.actaastro.2021.03.028.

[8] H. Burkhardt, M. Sippel, A. Herbertz, and J. Klevanski. "Kerosene vs. Methane: A Propellant Tradeoff for Reusable Liquid Booster Stages". In: *Journal of Spacecraft and Rockets* 41.5 (2004), pp. 762–769. DOI: 10.2514/1.2672.

[9] T. Neill, D. Judd, E. Veith, and D. Rousar. "Practical Uses of Liquid Methane in Rocket Engine Applications". In: *Acta Astronautica* 65.5 (2009), pp. 696–705. DOI: 10.1016/j.actaastro.2009.01.052.

[10] M. Rudnykh, S. Carapellese, D. Liuzzi, L. Arione, G. Caggiano, P. Bellomi, E. D'Aversa, R. Pellegrini, S. D. Lobov, A. A. Gurtovoy, and V. S. Rachuk. "Development of LM10-MIRA LOX/LNG Expander Cycle Demonstrator Engine". In: *Acta Astronautica* 126 (2016), pp. 364–374. DOI: 10.1016/j.actaastro.2016.04.018.

[11] Y. Hong, Z. Liu, S. Silvestri, M. P. Celano, O. J. Haidn, and Z. Yu. "An Experimental and Modelling Study of Heat Loads on a Subscale Methane Rocket Motor". In: *Acta Astronautica* 164 (2019), pp. 112–120. DOI: 10.1016/j.actaastro.2019.07.011.

[12] F. Nasuti and M. Pizzarelli. "Pseudo-Boiling and Heat Transfer Deterioration while Heating Supercritical Liquid Rocket Engine Propellants". In: *The Journal of Supercritical Fluids* 168 (2021), p. 105066. DOI: 10.1016/j.supflu.2020.105066.

[13] J. Volkmann, L. Tuegel, and J. Mcleod. *Gas Side Heat Flux and Film Coolant Investigation for Advanced LOX/Hydrocarbon Thrust Chambers*. AIAA Paper 1990–2184. 26th Joint Propulsion Conference. 1990. DOI: 10.2514/6.1990-2184.

[14] A. Kumakawa, M. Sasaki, K. Sato, H. Tamura, F. Ono, H. Sakamoto, and N. Yatsuyanagi. *Hot Gas Side Heat Transfer Characteristics of LOX/H2 and LOX/HC Type Propellants*. National Aerospace Laboratory TR-1062T. Tokyo, Japan, 1990.

[15] S. Silvestri, M. P. Celano, G. Schlieben, and O. J. Haidn. *Characterization of a Multi-Injector GOX/CH4 Combustion Chamber*. AIAA Paper 2016–4992. July 2016. DOI: 10.2514/6.2016-4992.

[16] S. Silvestri, C. Kirchberger, G. Schlieben, M. P. Celano, and O. J. Haidn. "Experimental and Numerical Investigation of a Multi-Injector GOX/CH4 Combustion Chamber". In: *Transactions of the Japan Society for Aeronautical and Space Sciences, Aerospace Technology Japan* 16.5 (2018), pp. 374–381. DOI: 10.2322/tastj.16.374.

[17] N. Perakis, D. Rahn, O. J. Haidn, and D. Eiringhaus. "Heat Transfer and Combustion Simulation of Seven-Element O2/CH4 Rocket Combustor". In: *Journal of Propulsion and Power* 35.6 (2019), pp. 1080–1097. DOI: 10.2514/1.B37402.

[18] A. Chemnitz, T. Sattelmayer, C. Roth, O. Haidn, Y. Daimon, R. Keller, P. Gerlinger, J. Zips, and M. Pfitzner. "Numerical Investigation of Reacting Flow in a Methane Rocket Combustor: Turbulence Modeling". In: *Journal of Propulsion and Power* 34 (2018), pp. 864–877. DOI: 10.2514/1.B36565.

[19] J. Zips, C. Traxinger, and M. Pfitzner. "Time-Resolved Flow Field and Thermal Loads in a Single-Element GOX/GCH4 Rocket Combustor". In: *International Journal of Heat and Mass Transfer* 143 (2019), p. 118474. DOI: 10.1016/j.ijheatmasstransfer.2019.118474.

[20] D. Maestro, B. Cuenot, and L. Selle. "Large Eddy Simulation of Combustion and Heat Transfer in a Single Element GOX/CH4 Rocket Combustor". In: *Flow, Turbulence and Combustion* 103.3 (2019), pp. 699–730. DOI: 10.1007/s10494-019-00036-w.

[21] N. Perakis and O. J. Haidn. "Inverse Heat Transfer Method Applied to Capacitively Cooled Rocket Thrust Chambers". In: *International Journal of Heat and Mass Transfer* 131 (2018), 150,Äì166. DOI: 10.1016/j.ijheatmasstransfer.2018.11.048.

[22] Y. Hong, Z. Liu, S. Silvestri, M. P. Celano, O. J. Haidn, and Z. Yu. "An Experimental and Modelling Study of Heat Loads on a Subscale Methane Rocket Motor". In: *Acta Astronautica* 164 (2019), pp. 112–120. DOI: 10.1016/j.actaastro.2019.07.011.

[23] D. Muto, Y. Daimon, H. Negishi, and T. Shimizu. "Wall Modeling of Turbulent Methane/Oxygen Reacting Flows for Predicting Heat Transfer". In: *International Journal of Heat and Fluid Flow* 87 (2021), p. 108755. DOI: 10.1016/j.ijheatfluidflow.2020.108755.

[24] Y. Daimon, H. Negishi, S. Silvestri, and O. J. Haidn. *Conjugated Combustion and Heat Transfer Simulation for a 7 element GOX/GCH4 Rocket Combustor*. AIAA Paper 2018–4553. July 2018. DOI: 10.2514/6.2018-4553.

[25] N. Perakis, O. J. Haidn, D. Eiringhaus, D. Rahn, S. Zhang, Y. Daimon, S. Karl, and T. Horchler. *Qualitative and Quantitative Comparison of RANS Simulation Results for a 7-Element GOX/GCH4 Rocket Combustor*. AIAA Paper 2018-4556. July 2018. DOI: 10.2514/6.2018-4556.

[26] J. Wei, M. Ye, S. Zhang, J. Qin, and O. J. Haidn. "Modeling of a 7-Elements GOX/CH4 Combustion Chamber Using RANS With Eddy-Dissipation Concept Model". In: *Aerospace Science and Technology* 99 (2020), p. 105762. DOI: 10.1016/j.ast.2020.105762.

[27] N. Perakis, J. Strauß, and O. J. Haidn. "Heat Flux Evaluation in a Multi-Element CH4/O2 Rocket Combustor Using an Inverse Heat Transfer Method". In: *International Journal of Heat and Mass Transfer* 142 (2019), p. 118425. DOI: 10.1016/j.ijheatmasstransfer.2019.07.075.

[28] E. Strokach, I. Borovik, and O. J. Haidn. "Simulation of the GOx/GCH4 Multi-Element Combustor Including the Effects of Radiation and Algebraic Variable Turbulent Prandtl Approaches". In: *Energies* 13.19 (2020), p. 5009. DOI: 10.3390/en13195009.

[29] G. Morrell. "Investigation of Internal Film Cooling of 1000-pound-thrust Liquid-ammonia-liquid-oxygen Rocket-engine Combustion Chamber". In: (1951).

[30] R. H. Boden. "Heat Transfer in Rocket Motors and the Application of Film and Sweat Cooling". In: *Transactions of ASME* 73 (1951), pp. 385–390.

[31] R. C. Stechman, J. Oberstone, and J. C. Stechmann. "Design Criteria for Film Cooling for Small Liquid-Propellant Rocket Engines." In: *Journal of Spacecraft and Rockets* 6.2 (1969), pp. 97–102.

[32] G. R. Kinney, A. E. Abramson, and J. L. Sloop. *Internal-liquid-film-cooling Experiments with Air-stream Temperatures to 2000 ÃäF in 2-and 4-inch-diameter Horizontal Tubes*. US Government Printing Office, 1952.

[33] A. E. Abramson. "Investigation of Internal Film Cooling of Exhaust Nozzle of a 1000-pound-thrust Liquid-ammonia Liquid-oxygen Rocket". In: (1952).

[34] W. E. Welsh. *Review of Results of an Early Rocket-engine Film-cooling Investigation at the Jet Propulsion Laboratory*. Jet Propulsion Laboratory, California Institute of Technology, 1961.

[35] D. L. Emmons. *Effects of Selected Gas Stream Parameters and Coolant Physical Properties on Film Cooling of Rocket Motors*. Tech. rep. Purdue univ lafayette ind jet propulsion center, 1962.

[36] C. F. Warner and D. L. Emmons. "Effects of Selected Gas Stream Parameters and Coolant Properties on Liquid Film Cooling". In: *Journal of Heat Transfer-transactions of The Asme* 86 (1964), pp. 271–278.

[37] R. A. Gater and M. R. L'Ecuyer. "A Fundamental Investigation of the Phenomena That Characterize Liquid-film Cooling". In: *International Journal of Heat and Mass Transfer* 13.12 (1970), pp. 1925–1939.

[38] R. Cook and R. Quentmeyer. "Advanced Cooling Techniques for High-pressure, Hydrocarbon-fueled Rocket Engines". In: *16th Joint Propulsion Conference*. 1980, p. 1266.

[39] L. Arrington, B. Reed, and J. A. Rivera. "A Performance Comparison of Two Small Rocket Nozzles". In: *32nd Joint Propulsion Conference and Exhibit*. 1996, p. 2582.

[40] R. C. Kesselring, B. L. Mcfarland, R. M. Knight, and R. N. Gurnitz. "Boundary Cooled Rocket Engines for Space Storable Propellants". In: (1972).

[41] J. Volkmann, J. Mcleod, and S. Claflin. "Investigation of Throat Film Coolant for Advanced LOX/RP-1 Thrust Chambers". In: *27th Joint Propulsion Conference*. 1991, p. 1979.

[42] J. G. Kim, K. J. Lee, S: Seo, Y. M. Han, H. J. Kim, and H. S. Choi. "Film Cooling Effects on Wall Heat Flux of a Liquid Propellant Combustion Chamber". In: *42nd AIAA/ASME/SAE/ASEE Joint Propulsion Conference & Exhibit*. 2006, p. 5196.

[43] E. L. Knuth. "The Mechanics of Film Cooling". PhD thesis. California Institute of Technology, 1954.

[44] L. Crocco. "An Approximate Theory of Porous, Sweat, or Film Cooling with Reactive Fluids". In: *Journal of the American Rocket Society* 22.6 (1952), pp. 331–338.

[45] A. R. Graham. "Film Cooling of Rocket Motors". PhD thesis. Jet Propulsion Center, Purdue University, 1958.

[46] J. P. Sellers. "Experimental and Theoretical Study of the Application of Film-Cooling to a Cylindrical Rocket Thrust Chamber". In: (1958).

[47] T. R. Shembharkar and B. R. Pai. "Prediction of Film Cooling with a Liquid Coolant". In: *International journal of heat and mass transfer* 29.6 (1986), pp. 899–908.

[48] R. A. Gater, M. R. L'Ecuyer, and C. F. Warner. *Liquid-film Cooling, its Physical Nature and Theoretical Analysis*. Tech. rep. Purdue university Lafayette in jet propulsion center, 1965.

[49] P. Sawant, M. Ishii, and M. Mori. "Droplet Entrainment Correlation in Vertical Upward Co-current Annular Two-phase Flow". In: *Nuclear Engineering and Design* 238.6 (2008), pp. 1342–1352.

[50] E. B. Coy, S. A. Schumaker, and M. A. Lightfoot. *Film Cooling of Liquid Hydrocarbon Engines for Operationally-Responsive Space Access*. Tech. rep. AIR FORCE RESEARCH LAB EDWARDS AFB CA PROPULSION DIRECTORATE, 2010.

[51] R. P. Miller and E. B. Coy. *Studies in Optimizing the Film Flow Rate for Liquid Film Cooling*. Tech. rep. AIR FORCE RESEARCH LAB EDWARDS AFB CA, 2011.

[52] S. R. Shine, S. S. Kumar, and B. N. Suresh. "Numerical Study of Wave Disturbance in Liquid Cooling Film". In: *Propulsion and Power Research* 2.2 (2013), pp. 107–118.

[53] R. L. Ewen and H. M. Evensen. *Liquid Rocket Engine Self-cooled Combustion Chambers: NASA Space Vehicle Design Criteria (chemical Propulsion)*. National Aeronautics and Space Administration, 1977.

[54] M. Trotti. "Modelling of liquid Film Cooling in a GOX Kerosene Rocket Combustion Chamber". In: (2012).

[55] W. M. Grisson. *Liquid Film Cooling in Rocket Engines*. Tech. rep. Morehouse Coll Atlanta GA, 1991.

[56] D. Jang, Y. Kwak, and S. Kwon. "Design and Validation of a Liquid Film-cooled Hydrogen Peroxide/Kerosene Bipropellant Thruster". In: *Journal of Propulsion and Power* 31.2 (2015), pp. 761–765.

[57] S. R. Shine, S. S. Kumar, and B. N. Suresh. "A New Generalised Model for Liquid Film Cooling in Rocket Combustion Chambers". In: *International Journal of Heat and Mass Transfer* 55.19-20 (2012), pp. 5065–5075.

[58] B. Leckner. "Spectral and Total Emissivity of Water Vapor and Carbon Dioxide". In: *Combustion and flame* 19.1 (1972), pp. 33–48.

[59] T. S. Wang and V. Luong. "Hot-gas-side and Coolant-side Heat Transfer in Liquid Rocket Engine Combustors". In: *Journal of Thermophysics and Heat Transfer* 8.3 (1994), pp. 524–530.

[60] H. W. Zhang, W. Q. Tao, Y. L. He, and W. Zhang. "Numerical Study of Liquid Film Cooling in a Rocket Combustion Chamber". In: *International Journal of Heat and Mass Transfer* 49.1-2 (2006), pp. 349–358.

[61] H. W. Zhang, Y. L. He, and W. Q. Tao. "Numerical Study of Film and Regenerative Rooling in a Thrust Chamber at High Pressure". In: *Numerical Heat Transfer, Part A: Applications* 52.11 (2007), pp. 991–1007.

[62] W. Yang and B. Sun. "Numerical Simulation of Liquid Film in a Liquid Oxygen/Rocket Propellant 1 Liquid Rocket". In: *Journal of thermophysics and heat transfer* 26.2 (2012), pp. 328–336.

[63] R. A. Seban, H. W. Chan, and S. Scesa. *Heat Transfer to a Turbulent Boundary Layer Downstream of an Injection Slot*. American Society of Mechanical Engineers, 1957.

[64] R. A. Seban. "Heat Transfer and Effectiveness for a Turbulent Boundary Layer with Tangential Fluid Injection". In: (1960).

[65] J. H. Chin, S. C. Skirvin, L. E. Hayes, and A. H. Silver. "Adiabatic Wall Temperature Downstream of a Single Tangential Injection Slot". In: *ASME Paper* 58-A (1958), p. 107.

[66] S. S. Papell and A. M. Trout. *Experimental Investigation of Air Film Cooling Applied to an Adiabatic Wall by Means of an Axially Discharging Slot*. National Aeronautics and Space Administration, 1959.

[67] N. Nishiwaki, A. Tsuchida, M. Hirata, S. Yamazaki, and M. Akiyama. "Heat Transfer on a Surface Covered by Cold Air Film". In: *Transactions of the Japan Society of Mechanical Engineers* 27.180 (1961), pp. 1285–1290. DOI: 10.1299/kikai1938.27.1285.

[68] R. J. Goldstein. "Film Cooling". In: *Advances in heat transfer*. Vol. 7. Elsevier, 1971, pp. 321–379.

[69] J. G. Lucas and R. L. Golladay. *An Experimental Investigation of Gaseous-film Cooling of a Rocket Motor*. Tech. rep. National Aeronautics and Space Administration Cleveland OH Lewis research center, 1963.

[70] J. J. Williams. *The Effect of Gaseous Film Cooling on the Recovery Temperature Distribution in Rocket Nozzles*. University of California, Davis., 1969.

[71] L. W. Carlson and E. Talmor. "Gaseous Film Cooling at Various Degrees of Hot-gas Acceleration and Turbulence Levels". In: *International Journal of heat and mass transfer* 11.11 (1968), pp. 1695–1713.

[72] C. Gau, K. A. Yih, and S. S. Chang. "Swirling Flow Effect on Film Cooling Performance Downstream of a Sudden Expansion". In: *Journal of thermophysics and heat transfer* 5.1 (1991), pp. 89–95.

[73] S. C. Kacker and J. H. Whitelaw. "The Effect of Slot Height and Slot-turbulence Intensity on the Effectiveness of the Uniform Density, Two-dimensional Wall Jet". In: (1968).

[74] E. P. Volchkov, S. S. Kutateladze, and A. I. Leont'ev. "Effect of Compressibility and Nonisothermicity on the Efficiency of Film Cooling in a Turbulent Boundary Layer". In: *Journal of Applied Mechanics and Technical Physics* 7.4 (1966), pp. 93–94.

[75] V. M. Repukhov. "Effects of Compressibility and Nonisothermal Conditions on the Performance of Film Cooling". In: *Journal of engineering physics* 19.5 (1970), pp. 1401–1408.

[76] D. R. Pedersen, Ernest R. G. Eckert, and R. J. Goldstein. "Film Cooling with Large Density Differences between the Mainstream and the Secondary Fluid Measured by the Heat-mass Transfer Analogy". In: (1977).

[77] T. Hansmann, H. Wilhelmi, and D. Bohn. "An Experimental Investigation of the Film-cooling Process at High Temperatures and Velocities". In: *5th International Aerospace Planes and Hypersonics Technologies Conference*. 1993, p. 5062.

[78] K. H. Dellimore, A. W. Marshall, and C. P. Cadou. "Influence of Compressibility on Film-cooling Performance". In: *Journal of Thermophysics and Heat Transfer* 24.3 (2010), pp. 506–515.

[79] R. Arnold, D. I. Suslov, and O. J. Haidn. "Experimental Investigation of Film Cooling with Tangential Slot Injection in a LOX/CH4 Subscale Rocket Combustion Chamber". In: *Transactions of the Japan Society for Aeronautical and Space Sciences, Space Technology Japan* 7.ists26 (2009), Pa_81–Pa_86.

[80] R. Arnold, D. I. Suslov, and O. J. Haidn. "Film Cooling in a High-pressure Subscale Combustion Chamber". In: *Journal of propulsion and power* 26.3 (2010), pp. 428–438.

[81] D. Suslov, R. Arnold, and O. J. Haidn. "Investigation of Film Cooling Efficiency in a High Pressure Subscale LOX/H2 Combustion Chamber". In: *47th AIAA/ASME/SAE/ASEE Joint Propulsion Conference & Exhibit*. 2011, p. 5778.

[82] M. P. Celano, S. Silvestri, C. Kirchberger, G. Schlieben, D. I. Suslov, and O. J. Haidn. "Gaseous Film Cooling Investigation in a Model Single Element GCH4-GOX Combustion Chamber". In: *Transactions of the Japan society for aeronautical and space sciences, aerospace technology Japan* 14.ists30 (2016), pp. 129–137.

[83] R. J. Goldstein, E. R. G. Eckert, F. K. Tsou, and A. Haji-Sheikh. "Film Cooling with Air and Helium Injection Through a Rearward-facingslot into a Supersonic Air Flow." In: *AIAA journal* 4.6 (1966), pp. 981–985.

[84] K. A. Juhany and M. L. Hunt. "Flowfield Measurements in Supersonic Film Cooling Including the Effect of Shock-wave Interaction". In: *AIAA journal* 32.3 (1994), pp. 578–585.

[85] B. Aupoix, A. Mignosi, S. Viala, F. Bouvier, and R. Gaillard. "Experimental and Numerical Study of Supersonic Film Cooling". In: *AIAA journal* 36.6 (1998), pp. 915–923.

[86] T. Kanda, F. Ono, M. Takahashi, T. Saito, and Y. Wakamatsu. "Experimental Studies of Supersonic Film Cooling with Shock Wave Interaction". In: *AIAA journal* 34.2 (1996), pp. 265–271.

[87] P. Reijasse and L. Boccaletto. "Influence of Film Cooling on Nozzle Side Loads". In: *46th AIAA Aerospace Sciences Meeting and Exhibit*. 2008, p. 392.

[88] J. S. Klein and M. Tribus. *Forced Convection from Nonisothermal Surfaces*. Tech. rep. 1952.

[89] J. P. Hartnett, R. C. Birkebak, and E. R. G. Eckert. "Velocity Distributions, Temperature Distributions, Effectiveness and Heat Transfer for Air Injected through a Tangential Slot into a Turbulent Boundary Layer". In: (1961).

[90] J. Librizzi and R. J. Cresci. "Transpiration Cooling of a Turbulent Boundary Layer in an Axisymmetric Nozzle". In: *AIAA Journal* 2.4 (1964), pp. 617–624.

[91] S. S. Kutateladze and A. I. Leontev. "The Heat Curtain in the Turbulent Boundary Layer of a Gas (Thermal Conditions on Solid Surface in Turbulent Boundary Layer Gas Flow Calculated to Determine Effective Heat Curtain)". In: *High Temperature* 1 (1963), pp. 250–258.

[92] J. L. Stollery and A. A. M. El-Ehwany. "A Note on the Use of a Boundary-layer Model for Correlating Film-cooling Data". In: *International Journal of Heat and Mass Transfer* 8.1 (1965), pp. 55–65.

[93] R. J. Goldstein and A. Haji-Sheikh. "Prediction of Film Cooling Effectiveness". In: *Proceedings of Japanese Society of Mechanical Engineers, Semi-International Symposium*. Vol. 2. 1967, p. 213.

[94] J. E. Hatch and S. S. Papell. *Use of a Theoretical Flow Model to Correlate Data for Film Cooling or Heating an Adiabatic Wall by Tangential Injection of Gases of Different Fluid Properties*. National Aeronautics and Space Administration, 1959.

[95] J. P. Sellers Jr. "Gaseous Film Cooling with Multiple Injection Stations". In: *AIAA Journal* 1.9 (1963), pp. 2154–2156.

[96] D. B. Spalding. "Prediction of Adiabatic Wall Temperatures in Film-cooling Systems". In: *AIAA Journal* 3.5 (1965), pp. 965–967.

[97] R. Arnold, D. Suslov, and O. J. Haidn. "Film Cooling of Accelerated Flow in a Subscale Combustion Chamber". In: *Journal of propulsion and power* 25.2 (2009), pp. 443–451.

[98] F. F. Simon. "Jet Model for Slot Film Cooling with Effect of Free-stream and coolant Turbulence". In: *NASA STI/Recon Technical Report N* 87 (1986), p. 18034.

[99] C. J. Marek and R. R. Tacina. "Effect of Free-stream Turbulence on Film Cooling". In: *NASA STI/Recon Technical Report N* 75 (1975), p. 25093.

[100] F. Di Matteo, M. Venanzi, M. De Rosa, and M. Onofri. "Modelling and Simulation of Film Cooling in Liquid Rocket Engine Propulsion Systems". In: (2012), p. 3908.

[101] D. Suslov, B. Betti, T. Aichner, S. Soller, F. Nasuti, and J. Haidn O. "Experimental Investigation and CFD-simulation of the Film Cooling in an O2/CH4 Subscale Combustion Chamber". In: *Space Propulsion Conference*. Association Aéronautique et Astronautique de France Paris, France. 2012.

[102] B. Betti, E. Martelli, F. Nasuti, and M. Onofri. *Numerical Study of Heat Transfer in Film Cooled Thrust Chambers*. AIAA Paper 2012-3907. Sept. 2012. DOI: 10.2514/6.2012-3907.

[103] Y. Daimon, H. Negishi, M. Koshi, and D. Suslov. "Numerical and Experimental Investigation of the Methane Film Cooling in Subscale Combustion Chamber". In: *Progress in Propulsion Physics* 8 (2016), pp. 129–144.

[104] P. G. Han, H. J. Namkoung, K. H. Kim, and Y. C. Woo. "A Study on the Cooling Mechanism in Liquid Rocket Engine". In: *40th AIAA/ASME/SAE/ASEE Joint Propulsion Conference and Exhibit*. 2004, p. 3672.

[105] M. Takahashi, T. Tomita, M. Takahashi, H. Tamura, Y. Watanabe, and M. Tsuboi. "Influence of a Gap for Film Cooling on Transient Flow Characteristics of Rocket Engine Nozzles". In: *38th AIAA/ASME/SAE/ASEE Joint Propulsion Conference & Exhibit*. 2002, p. 4147.

[106] T. S. Wang and M. Guidos. "Transient Three-dimensional Side-load Analysis of a Film-cooled Nozzle". In: *Journal of Propulsion and Power* 25.6 (2009), pp. 1272–1280.

[107] F. Nasuti, E. Martelli, M. Onofri, and E. Pietropaoli. "Film Cooling in Dual Bell Nozzles". In: *Fifth European Symposium on Aerothermodynamics for Space Vehicles*. Vol. 563. 2005, p. 459.

[108] E. Martelli, F. Nasuti, and M. Onofri. "Numerical Analysis of Film Cooling in Advanced Rocket Nozzles". In: *AIAA journal* 47.11 (2009), pp. 2558–2566.

[109] J. D. Anderson. *Hypersonic and High-Temperature Gas Dynamics*. AIAA Education series, Reston, VA, 2006, pp. 596–617. DOI: 10.2514/4.105142.

[110] K. Sutton and P. Gnoffo. *Multi-Component Diffusion with Application to Computational Aerothermodynamics*. AIAA Paper 98-2575. June 1998, p. 2575.

[111] J. O. Hirschfelder, C. F. Curtiss, and R. B. Bird. *Molecular Theory of Gases and Liquids*. New York, USA: John Wiley & Sons, Inc., 1954.

[112] B. J. McBride, M. J. Zehe, and S. Gordon. *NASA Glenn Coefficients for Calculating Thermodynamic Properties of Individual Species*. NASA/TP–2002–211556. 2002.

[113] B. J. McBride and S. Gordon. *Computer Program for Calculation of Complex Chemical Equilibrium Compositions and Applications*. NASA RP-1311. 1994.

[114] P. R. Spalart and S. R. Allmaras. "A One-Equation Turbulence Model for Aerodynamic Flows". In: *La Recherche Aerospatiale* 1 (1994), pp. 5–21.

[115] W. P. Jones and R. P. Lindstedt. "Global Reaction Schemes for Hydrocarbon Combustion". In: *Combustion and Flame* 73 (1988), pp. 233–249. DOI: 10.1016/0010-2180(88)90021-1.

[116] B. Betti, D. Bianchi, F. Nasuti, and E. Martelli. "Chemical Reaction Effects on Heat Loads of CH4/O2 and H2/O2 Rockets". In: *AIAA Journal* 54.5 (2016), pp. 1693–1703. DOI: 10.2514/1.J054606.

[117] J. Liberatori, R. Malpica Galassi, D. Bianchi, F Nasuti, M. Valorani, and P. P. Ciottoli. "A Family of Skeletal Reaction Mechanisms for Methane-Oxygen Combustion at High Pressure". In: *Journal of Propulsion and Power* (2022). Submitted for publication.

[118] V. P. Zhukov. "Kinetic Model of Alkane Oxidation at High Pressure from Methane to n-heptane". In: *Combustion Theory and Modelling* 13.3 (2009), pp. 427–442.

[119] https://cantera.org/science/kinetics.html.

[120] J. Troe. "Theory of Thermal Unimolecular Reactions in the Fall-off Range. I. Strong Collision Rate Constants". In: *Berichte der Bunsengesellschaft für physikalische Chemie* 87.2 (1983), pp. 161–169.

[121] R. G. Gilbert, K. Luther, and J. Troe. "Theory of Thermal Unimolecular Reactions in the Fall-off Range. II. Weak Collision Rate Constants". In: *Berichte der Bunsengesellschaft für physikalische Chemie* 87.2 (1983), pp. 169–177.

[122] G. Leccese, D. Bianchi, B. Betti, D. Lentini, and F. Nasuti. "Convective and Radiative Wall Heat Transfer in Liquid Rocket Thrust Chambers". In: *Journal of Propulsion and Power* 34.2 (2018), pp. 318–326. DOI: 10.2514/1.B36589.

[123] B. Betti, M. Pizzarelli, and F. Nasuti. *Coupled Heat Transfer Analysis in Regeneratively Cooled Thrust Chambers*. AIAA Paper 2012–4123. Sept. 2012. DOI: 10.2514/6.2012-4123.

[124] G. Leccese, D. Bianchi, and F. Nasuti. "Numerical Investigation on Radiative Heat Loads in Liquid Rocket Thrust Chambers". In: *Journal of Propulsion and Power* 35.5 (2019), pp. 930–943. DOI: 10.2514/1.B37536.

[125] M. Pizzarelli, F. Nasuti, R. Paciorri, and M. Onofri. "Numerical Analysis of Three-Dimensional Flow of Supercritical Fluid in Cooling Channels". In: *AIAA Journal* 47.11 (2009), pp. 2534–2543. DOI: 10.2514/1.38542.

[126] D. Bianchi, B. Betti, F. Nasuti, and C. Carmicino. "Simulation of Gaseous Oxygen/Hydroxyl-Terminated Polybutadiene Hybrid Rocket Flowfields and Comparison with Experiments". In: *Journal of Propulsion and Power* 31.3 (2015), pp. 919–929. DOI: 10.2514/1.B35587.

[127] D. Bianchi, F. Nasuti, and C. Carmicino. "Hybrid Rockets with Axial Injector: Port Diameter Effect on Fuel Regression Rate". In: *Journal of Propulsion and Power* 32.4 (2016), pp. 984–996. DOI: 10.2514/1.B36000.

[128] M. T. Migliorino, D. Bianchi, and F. Nasuti. "Numerical Analysis of Paraffin-Wax/Oxygen Hybrid Rocket Engines". In: *Journal of Propulsion and Power* 36.6 (2020), pp. 806–819. DOI: 10.2514/1.B37914.

[129] P. L. Roe. "Approximate Riemann Solvers, Parameter Vectors and Difference Schemes". In: *Journal of Computational Physics* 43 (1981), pp. 357–372. DOI: 10.1016/0021-9991(81)90128-5.

[130] G. Strang. "On the Construction and Comparison of Difference Schemes". In: *SIAM Journal on Numerical Analysis* 5 (1968), pp. 506–517. DOI: 10.1137/0705041.

[131] P. N. Brown, G. D. Byrne, and A. C. Hindmarsh. "VODE: A Variable-Coefficient ODE Solver". In: *SIAM Journal on Scientific and Statistical Computing* 10 (1989), pp. 1038–1051. DOI: 10.1137/0910062.

[132] J. Liu and S. N. Tiwari. "Radiative Heat Transfer Effects in Chemically Reacting Nozzle Flows". In: *Journal of Thermophysics and Heat Transfer* 10.3 (1996), pp. 436–444. DOI: 10.2514/3.808.

[133] M. F. Modest. *Radiative Heat Transfer*. Academic Press, San Diego, 2013.

[134] C. L. Tien. "Thermal Radiation Properties of Gases". In: *Advances in Heat Transfer*. Ed. by T. F. Irvine and J. P. Hartnett. Vol. 5. New York: Academic Press, 1968, pp. 253–324. DOI: 10.1016/S0065-2717(08)70131-X.

[135] P. Rivière and A. Soufiani. "Updated Band Model Parameters for H2O, CO2, CH4 and CO Radiation at High Temperature". In: *International Journal of Heat and Mass Transfer* 55 (2012), pp. 3349–3358. DOI: 10.1016/j.ijheatmasstransfer.2012.03.019.

[136] M. Chmielewski and M. Gieras. "Planck Mean Absorption Coefficients of H_2O, CO_2, CO and NO for radiation numerical modeling in combusting flows". In: *Journal of Power Technologies* 95.2 (2015), pp. 97–104.

[137] T. H. Chilton and A. P. Colburn. "Mass Transfer (Absorption) Coefficients Prediction from Sata on Heat Transfer and Fluid Friction". In: *Industrial & engineering chemistry* 26.11 (1934), pp. 1183–1187.

[138] F. Di Matteo, M. De Rosa, and M. Onofri. "Semi-empirical Heat Transfer Correlations in Combustion Chambers for Transient System Modelling". In: *3AF, editor, Space Propulsion Conference*. 2010.

[139] G. Sdoga. "Tecnica del Film Cooling in Endoreattori a Propellente Liquido: Sviluppo e Validazione di un Modello Empirico Mediante Simulazioni CFD". M.Sc. dissertation. Sapienza University of Rome, 2020.

[140] R. Arnold, D. Suslov, O. J. Haidn, and B. Weigand. "Investigation of Film Cooling in a High Pressure LOX/GH2 Subscale Combustion Chamber". In: *Space Propulsion Conference, Crete (Greece)*. 2008.

[141] P. J. Roache. "Verification of Codes and Calculations". In: *AIAA Journal* 36.5 (1998), pp. 696–702. DOI: 10.2514/2.457.

[142] A. Bonfiglioli and R. Paciorri. "Convergence Analysis of Shock-Capturing and Shock-Fitting Solutions on Unstructured Grids". In: *AIAA Journal* 52.7 (2014), pp. 1404–1416.

[143] N. Perakis, O. J. Haidn, and M. Ihme. "Investigation of CO Recombination in the Boundary Layer of CH4/O2 Rocket Engines". In: *Proceedings of the Combustion Institute* 38.4 (2021), pp. 6403–6411. DOI: 10.1016/j.proci.2020.07.080.

[144] J. Wei, S. Zhang, X. Zhou, C. Cheng, J. Qin, and O. J. Haidn. "Effects of Near Wall Flow and Non-Equilibrium Reaction Coupling on Heat Flux Prediction Inside a 7-Elements GOX/GCH4 Combustion Chamber". In: *Applied Thermal Engineering* 204 (2022), p. 118021. ISSN: 1359-4311. DOI: 10.1016/j.applthermaleng.2021.118021.

[145] D. Eiringhaus, D. Rahn, H. Riedmann, O. Knab, and O. J. Haidn. "Numerical Investigation of a 7-Element GOX/GCH4 Subscale Combustion Chamber". In: *7th European Conference for Aeronautics and Space Sciences (EUCASS)*. 2017. DOI: 10.13009/EUCASS2017-173.

[146] M. Leonardi, F. Nasuti, and M. Onofri. "Basic Analysis of a LOX/Methane Expander Bleed Engine". In: *EUCASS 2017* (2017).

[147] https://cameochemicals.noaa.gov/chris/KRS.pdf.